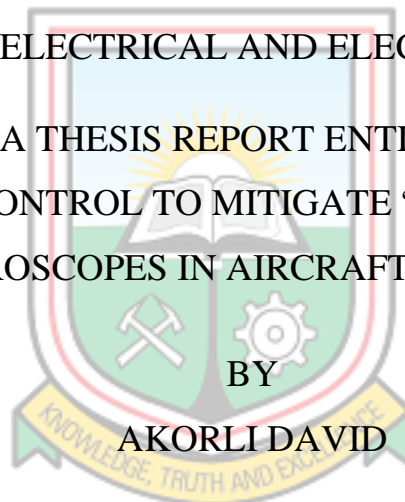UNIVERSITY OF MINES AND TECHNOLOGY, TARKWA

FACULTY OF ENGINEERING

DEPARTMENT OF ELECTRICAL AND ELECTRONIC ENGINEERING

A THESIS REPORT ENTITLED

ENHANCED CONTROL TO MITIGATE "FAULTS" OF MEMS
VIBRATORY GYROSCOPES IN AIRCRAFT AUTOPILOT SYSTEMS

BY

AKORLI DAVID

SUBMITTED IN FULFILMENT OF THE REQUIREMENT FOR THE
AWARD OF THE DEGREE OF MASTER OF PHILOSOPHY IN
ELECTRICAL AND ELECTRONIC ENGINEERING

THESIS SUPERVISOR

…………………………..
MR ERWIN NORMANYO

TARKWA, GHANA
JUNE 2020

DECLARATION

I declare that this thesis is my own work. It is being submitted for examination and approval for the Degree of Master of Philosophy in Electrical and Electronic Engineering in the University of Mines and Technology, Tarkwa. It has not been submitted for any degree, examination or approval in any other University.

....
(Signature of Candidate)

……. day of September, 2020.

ABSTRACT

Aircraft autopilots are automatic flight control and stabilisation systems. A segment of the autopilot is the pitch control system that is responsible for up or down movement of the aircraft about its lateral axis. One militating factor of hitherto existing pitch control systems is the faults of relatively large sized mechanical or other deployed gyroscopes that are capable of malfunctioning the aircraft autopilot system. In this research, the small sized and cheaper MEMS vibratory gyroscope has been investigated by modelling and simulation for temperature and noise effects and deployed as an angular rate sensor in the pitch control system. MEMS vibratory gyroscope output signal response stood at $\pm 5\%$ at 12.5 dps and 33 dps instead of the accepted standard value of $\pm 2\%$. The temperature and noise effects as "faults" affected the performance of the MEMS vibratory gyroscope. PI, PID. Fuzzy-PI, fuzzy-PID and ANFIS controllers were then used to mitigate the effect of the oscillations at the output of the MEMS vibratory gyroscope on the pitch control system. The ANFIS and the two fuzzy controllers did well but settled with remnant oscillations. Particle swarm optimisation and flower pollination algorithms were deployed to optimise the three controllers. The particle swarm optimisation combined with ANFIS controller successfully eradicated the temperature and noise effects on the pitch control system. Additionally, it performed better than the other options in terms of overshoot and settling time. Subject to further research, MEMS vibratory gyroscopes stand to be deployed effectively in aircraft autopilot systems to contribute to global safety in the aviation industry.

DEDICATION

To the Almighty God

ACKNOWLEDGEMENTS

TABLE OF CONTENTS

CHAPTER 5   OPTIMAL MITIGATION OF TEMPERATURE AND   86
NOISE EFFECTS OF THE PITCH CONTROL SYSEM

CHAPTER 6   CONCLUSIONS AND RECOMMENDATIONS   102

LIST OF FIGURES

Pitch Angle of 33 degrees with FPA and PSO Algorithms

LIST OF TABLES

LIST OF ABBREVIATIONS

Abbreviation	Meaning
AAS	Aircraft Autopilot System
ADC	Air Data Computer
ACF	Auto Correlation Function
ADRC	Active Disturbance Rejection Control
AFCS	Automatic Flight Control System
AHRS	Attitude Heading and Reference System
AI	Artificial Intelligence
ANFIS	Adaptive Neuro Fuzzy Inference System
ARMA	Auto Regressive Moving Average
ATC	Air Traffic Control
AVMT	Allan Variance Measurement Technique
BiT	Built-in Test
COTS	Commercial Off-The-Shelf
DoF	Degrees of Freedom
FPA	Flower Pollination Algorithm
GM	Gauss-Markov
GPS	Global Position System
IMU	Inertial Measurement Units
M	Medium
MB	Medium Big
MEMS	Microelectromechanical System
MS	Medium Small
NB	Negative Big
NS	Negative Small
PI	proportional Integral controller
PID	Proportional Integral Derivative controller
PB	Positive Big
PM	Positive Medium
PSO	Particle Swarm Optimisation Algorithm
SEEMD	Sample Entropy Empirical Mode Decomposition
THB	Temperature Humidity Bias

UAV	Unmanned Aerial Vehicle
VB	Very Big
VL	Very Large
VS	Very Small
Z	Zero
ZRO	Zero Rate Output

LIST OF SYMBOLS

Acceleration component in the drive direction a_x

Acceleration component in the sense direction a_y

Acceleration due to gravity g

Aileron deflection angle δ_a

Angular speed of rotation Ω

Beam stiffness in the drive direction k_x

Beam stiffness in the sense direction k_y

Coriolis force F

Damping coefficient in the drive direction c_x

Damping coefficient in the sense direction c_y

Density of air d

Density of the flowing fluid ρ

Drag coefficient C_D

Drag D

Electrostatic force applied by the drive comb F_d

Elevator deflection angle δ_e

Elevator servo gain k_a

Final elevation head of the center of the cross section with respect to a datum h_2

Final mass flow rate m_e^*

Final mean velocity of fluid flow at the cross section v_2

Final pressure of fluid at the cross section p_2

Final time t_e

Final velocity of air V_e

Initial elevation head of the center of the cross section with respect to a datum h_1

Initial mass flow rate m_o^*

Initial mean velocity of fluid flow at the cross section v_1

Initial pressure of fluid at the cross section p_1

Initial time t_o

Initial velocity of air V_o

Input voltage	v
Lift coefficient	C_L
Lift	L
Mass flow rate	m^*
Moment of inertia about the roll axis	J
Roll angle	ϕ
Rudder deflection angle	δ_e
Rudder servo gain	k_r
Servomotor time constant	τ
Stability derivative representing damping in roll	C_{l_p}
Stability derivatives representing the rolling moment (aileron deflection angle)	$C_{l_{\delta a}}$
Surface area of wing	A
Thrust	F
Total mass of aircraft	m
Velocity component in the drive direction	v_x
Velocity component in the sense direction	v_y
Velocity of air	V
Weight	W

INTERNATIONAL SYSTEM OF UNITS (SI UNITS)

Quantity	Unit	Symbol
Acceleration due to gravity	meter per square meter	m/s^2
Angular rate	degrees per second	dps
Area	square meter	m^2
Density	kilogram per cubic meter	kg/m^3
Deflection angle	degree or radian	deg or rad
Dynamic pressure	Newton per square meter	N/m^2
Frequency	hertz	Hz
Length	millimeter	mm
Mass	kilogram	kg
Mass flow rate	Kilogram per second	kg/s
Momentum	Kilogram meter per second	kg.m/s
Overshoot	percentage	%
Pressure	Pascal	Pa
Thrust	Newton	N
Time	seconds	s
Velocity	meter per second	m/s
Voltage	volt	V
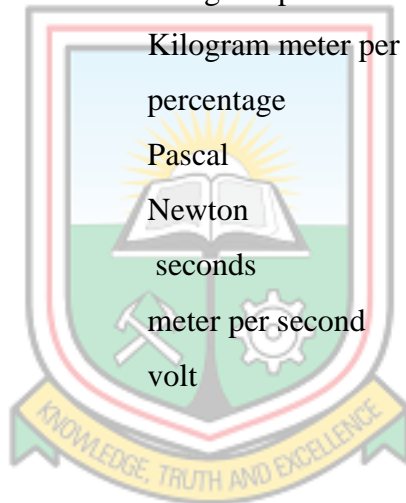
CHAPTER 1

GENERAL INTRODUCTION

1.1   Background to the Research

Aircrafts fly under many conditions. External conditions can alter the desired flight characteristics of the aircraft. To maintain the desired characteristics of the aircraft, the pilot moves the control surfaces either manually or automatically. There are indicating systems and instruments that supply the pilot with information on the performance of the aircraft in flight. The pilot must be able to see and interpret each of these indications and then react to get the desired performance. In high performance aircrafts, especially single-piloted aircraft, other flight duties require much of the pilot's time (Brandt, 2011). Navigation, communication, radar and other special equipment are severely limited if the pilot has to work continually on the physical manipulation of the controls (Stroe *et al*., 2017).

In high-performance aircrafts capable of supersonic flight, aircraft speed is so great that the pilot's normal response time is far too slow. For example, by the time the pilot reacts to an indication to position a control surface, the aircraft may already be out of control. Automatic flight control and stabilisation systems ease the pilot's workload and provide aircraft stability at all speeds (Anon., 2017d). The information now flows directly to a flight control computer rather than to an indicator. This action lessens the time required to start a control movement to nearly zero. The result is increased stability. These systems also provide command controls by which the computer can control the aircraft in nearly any desired flight condition. Some automatic flight control systems are capable of flying the aircraft by radio navigation aids, correcting for wind and making pilot-unaided landings (Geliev *et al*., 2019).

The term Automatic Flight Control System (AFCS) is used, or the shortened version, autopilot. A reliable AFCS is necessary because pilots have duties other than moving the flight controls. However, regardless of how sophisticated the AFCS computer may be, the reasoning power of the pilot cannot be duplicated (Geliev *et al*., 2019).

1.2   Problem Definition

An autopilot aids pilot's workload, but it is highly susceptible to malfunction as a result of external conditions that alter the desired flight characteristics of the aircraft. These affect the primary flight control systems such as elevator, rudder and aileron of the aircraft which operate through servos. According to Uhlig *et al.* (2006), one of the common problems of

autopilot failure is as a result of servo failure, either because of malfunction of motor or unreliable electrical connection. Also, gyroscopes which form part of the Aircraft Autopilot System (AAS) can malfunction leading to failure of the system. This research, thus, seeks to further investigate the gyroscope-related failures of Aircraft Autopilot Systems (AASs) and also evaluate the performance of the gyroscope under adverse external conditions.

1.3 Purpose of the Research

This work is purposed to investigate possible faults and use of MEMS vibratory gyroscopes in AASs.

1.4 Objectives of the Research

The specific objectives are as follows:

i. Find out possible sources of failure of MEMS vibratory gyroscopes;

ii. Investigate the MEMS vibratory gyroscope with regards to input angular rates and faults signals; and

iii. Develop controllers for the mitigation of "failures" of MEMS vibratory gyroscopes in the AAS for optimal performance.

1.5 Expected Outcomes

It is expected that this research would yield the following outcomes:

i. A model that presents failures of gyroscopes in AAS; and

ii. Mitigation of the effects of MEMS vibratory gyroscope "faults" on AASs upon implementation of the findings.

1.6 Research Questions and Hypothesis

The following research questions can be deduced:

i. Can "failures" of MEMS vibratory gyroscopes in AASs be modelled?

ii. What conditions and design parameters would ensure an economical modification of the MEMS vibratory gyroscope in AASs?

iii. Can there be better performance of MEMS vibratory gyroscopes in AASs?

Therefore, the research hypothesis is stated as: MEMS vibratory gyroscope-related "failures" in AASs can be modelled, simulated and mitigated to achieve optimal performance of AASs.

1.7   Scope of the Research

The research is conducted within the framework of AASs, MEMS vibratory gyroscopes, mathematical modelling and computer simulations.

1.8   Research Methods Used

The following methods were used to achieve the objectives:

i.   Review of faults of MEMS vibratory gyroscopes in AASs;

ii.   Development of control system models for investigating and mitigating faults of MEMS vibratory gyroscopes in AASs; and

iii. Validation of the models by way of computer simulations.

1.9   Facilities Used for the Research

The facilities used in this research work include the following:

i.   Library, Laboratory, Computer and Internet facilities at UMaT;

ii.   Laptop computer with MATLAB/Simulink software; and

iii. Facilities of School of Trade Training, Air Force Base Accra and Takoradi Base.

1.10   Significance of the Research

The significance of this research could be seen in the following:

i.   To augment present research on MEMS vibratory gyroscopes usage in AAS; and

ii.   To contribute to global safety in the aviation industry upon implementation of findings.

1.11   Limitations of the Research

The unavailability of laboratories and MEMS vibratory gyroscope components that could have aided in the research is a challenge to this research.

1.12 Definition of Terms and Key Concepts

Aircraft: An aircraft is a machine that is able to fly by gaining support from the air. It counters the force of gravity by using either static lift or by using the dynamic lift of an airfoil, or in a few cases the downward thrust from jet engines.

Autopilot: Autopilot is a system used to control the trajectory/path of an aircraft without constant hands-on control by a human operator being required.

Gyroscope: A gyroscope is a device used for measuring or maintaining orientation and angular velocity. It is a spinning wheel or disc in which the axis of rotation is free to assume any orientation by itself.

MEMS: It is a microelectromechanical system device that is made within the scale of 1 mm to 1 μm and combine electrical components with mechanical systems which uses vibrating mechanical element as a sensing element for detecting angular velocity.

MEMS gyroscope: A MEMS gyroscope is a sensor that measures the rate of change in the angular position of an object.

Radar: It is a system for detecting the presence, direction, distance, and speed of aircraft, ships, and other objects, by sending out pulses of radio waves which are reflected off the object back to the source.

1.13 Organisation of the Thesis

The thesis is organised into six chapters. Chapter 1 is the general introduction to the research work which includes the background to the research, problem definition, objectives of the research, expected outcomes, research questions and hypothesis, scope of the research, research methods used, facilities used for the research, significance of the research, limitations of the research, definition of terms and key concepts and the organisation of the thesis. Chapter 2 reviews the literature on the topic and includes an overview of the history of aircrafts, types of aircraft, the primary control systems, autopilot systems and components, gyroscopes, types of gyroscopes and their applications and a review of related works on faults of MEMS vibratory gyroscopes. Chapter 3 deals with the mathematical modelling and simulations of the MEMS vibratory gyroscope. Chapter 4 presents the mathematical modelling, design of controllers and simulations of the pitch control system for the mitigation of the faults in AAS. Chapter 5 is devoted to two Artificial Intelligence (AI) networks that are employed in the further mitigation of gyroscope-related faults on the

performance of the pitch control system of the AAS. Chapter 6 gives the conclusions, recommendations, research contributions and future research directions.

CHAPTER 2

LITERATURE REVIEW

2.1 Introduction

The history of aviation has extended over more than two thousand years, from the earliest forms of aviation such as kites and attempts at tower jumping, to supersonic, and hypersonic flight by powered, heavier-than-air jets. Kite flying in China dates back to several hundred years Before Christ (BC) and slowly spread around the world. It is thought to be the earliest example of man-made flight. Leonardo da Vinci's 15th century dream of flight found expression in several rational but unscientific designs, though he did not attempt to construct any of them. The discovery of hydrogen gas in the 18th century led to the invention of the hydrogen balloon, at almost exactly the same time that the Montgolfier brothers rediscovered the hot-air balloon and began manned flights. Various theories in mechanics by physicists during the same period of time, notably fluid dynamics and Newton's laws of motion, led to the foundation of modern aerodynamics, most notably by Sir George Cayley. Balloons, both free-flying and tethered, began to be used for military purposes from the end of the 18th century, with the French government establishing balloon companies during the revolution (Villani and Miyagi, 2016).

The term aviation, noun of action stems from Latin avis "bird" with suffix -ation meaning action or progress, was coined in 1863 by French pioneer Guillaume Joseph Gabriel de La Landelle (1812–1886) in "Aviation ou Navigation aérienne sans ballons". Using a methodological approach and concentrating on the controllability of the aircraft, the Wrights brothers built and tested a series of kites and glider designs from 1900 to 1902 before attempting to build a powered design. The gliders worked, but not as well as the Wrights had expected based on the experiments and writings of their 19th century predecessors. Their first glider, launched in 1900, had only about half the lift they anticipated. Their second glider, built the following year, performed even more poorly. Rather than giving up, the Wrights constructed their own wind tunnel and created a number of sophisticated devices to measure lift and drag on the two hundred wing designs they tested. As a result, the Wrights corrected earlier mistakes in calculations regarding drag and lift. Their testing and calculation produced a third glider with a higher aspect ratio and true three-axis control. They flew it successfully hundreds of times in 1902, and it performed far better than the previous models. By using a rigorous system of experimentation involving wind-tunnel testing of airfoils and flight testing of full-size prototypes, the Wrights not only built a

working aircraft, the "Wright Flyer", but also helped advance the science of aeronautical engineering. Experiments with gliders provided the groundwork for heavier-than-air craft, and by the early 20th century, advances in engine technology and aerodynamics made controlled, powered flight possible for the first time. The modern aeroplane with its characteristic tail was established in 1909 and from then on the history of the aeroplane became tied to the development of more and more powerful engines (Jakab, 2014).

The first great ships of the air were the rigid dirigible balloons pioneered by Ferdinand von Zeppelin, which soon became synonymous with airships and dominated long-distance flight until the 1930s, when large flying boats became popular (Prentice *et al*., 2010). After World War II, the flying boats were in turn replaced by land planes, and the new and immensely powerful jet engine revolutionised both air travel and military aviation (Anon., 2010). In the latter part of the 20th century the advent of digital electronics produced great advances in flight instrumentation and "fly-by-wire" systems. The 21st century sees the large-scale deployment of pilotless drones for military, civilian and leisure use. With digital controls, inherently unstable aircrafts such as flying wings became possible (Feng *et al*., 2011).

2.2 Aircrafts

An aircraft is a machine that is able to fly by gaining support from the air (Anon., 2017a). It counters the force of gravity by using either static lift or by using the dynamic lift of an airfoil, or in a few cases the downward thrust from jet engines (Anon., 2017b). Common examples of aircraft include airplanes, helicopters, airships (including blimps), gliders and hot air balloons. Figure 2.1 to Figure 2.5 show some types of aircraft.
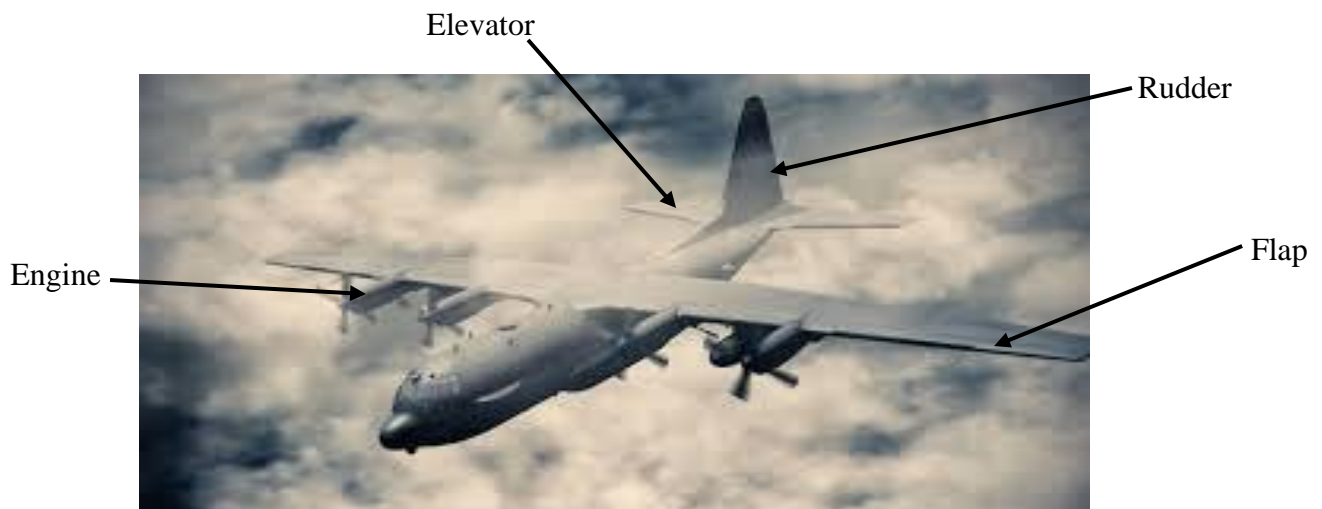
Fig. 2.1 Example of an Airplane
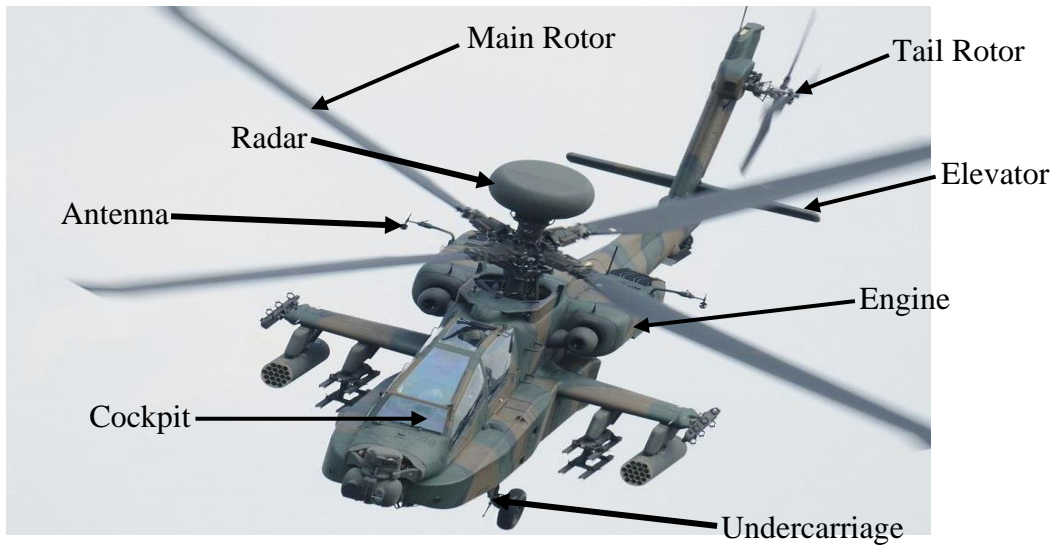
Fig. 2.2 Example of an Armed Helicopter
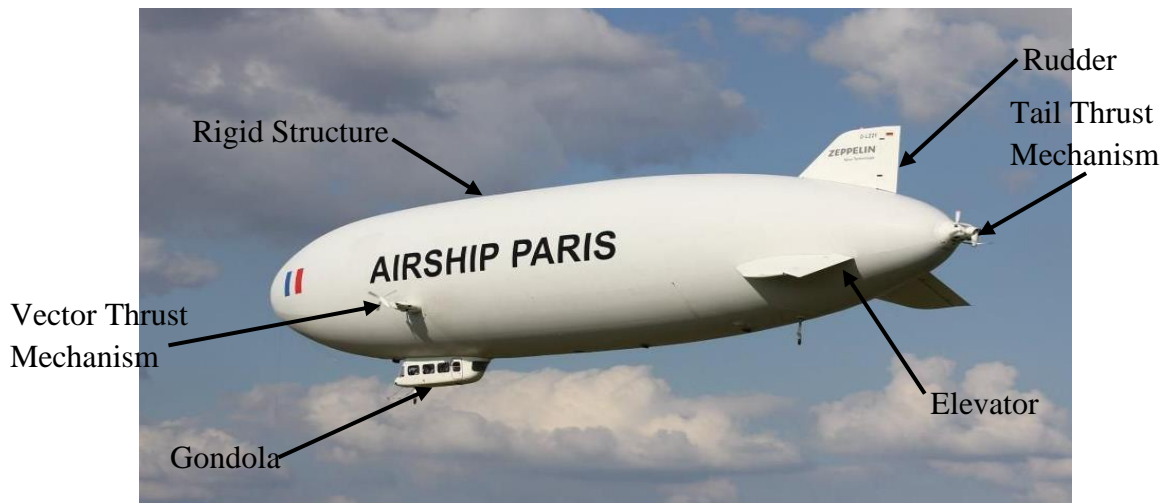
Fig. 2.3 Example of an Airship

Fig. 2.4 Example of a Glider
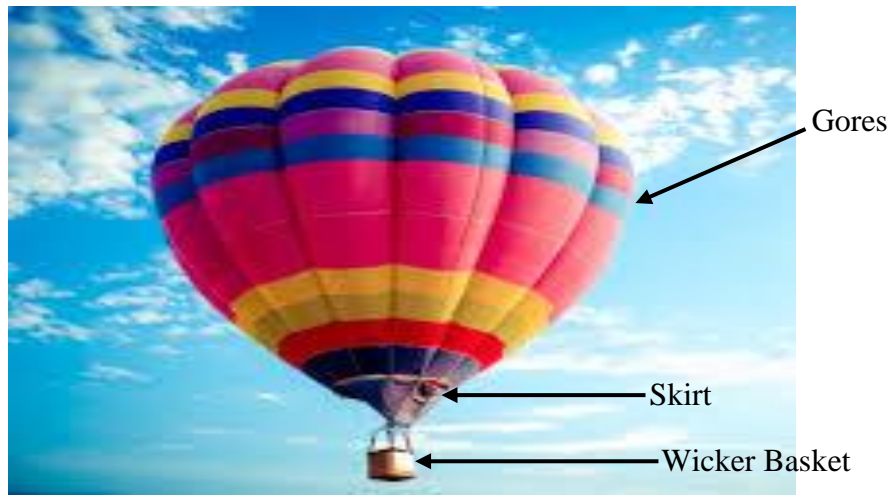
Fig. 2.5 Example of a Hot Balloon

2.2.1   Classification of Aircrafts

The various aircrafts are classified according to mode, mach number, general purpose, engine type and military purpose as presented in Fig. 2.6 (Anon., 2017c).
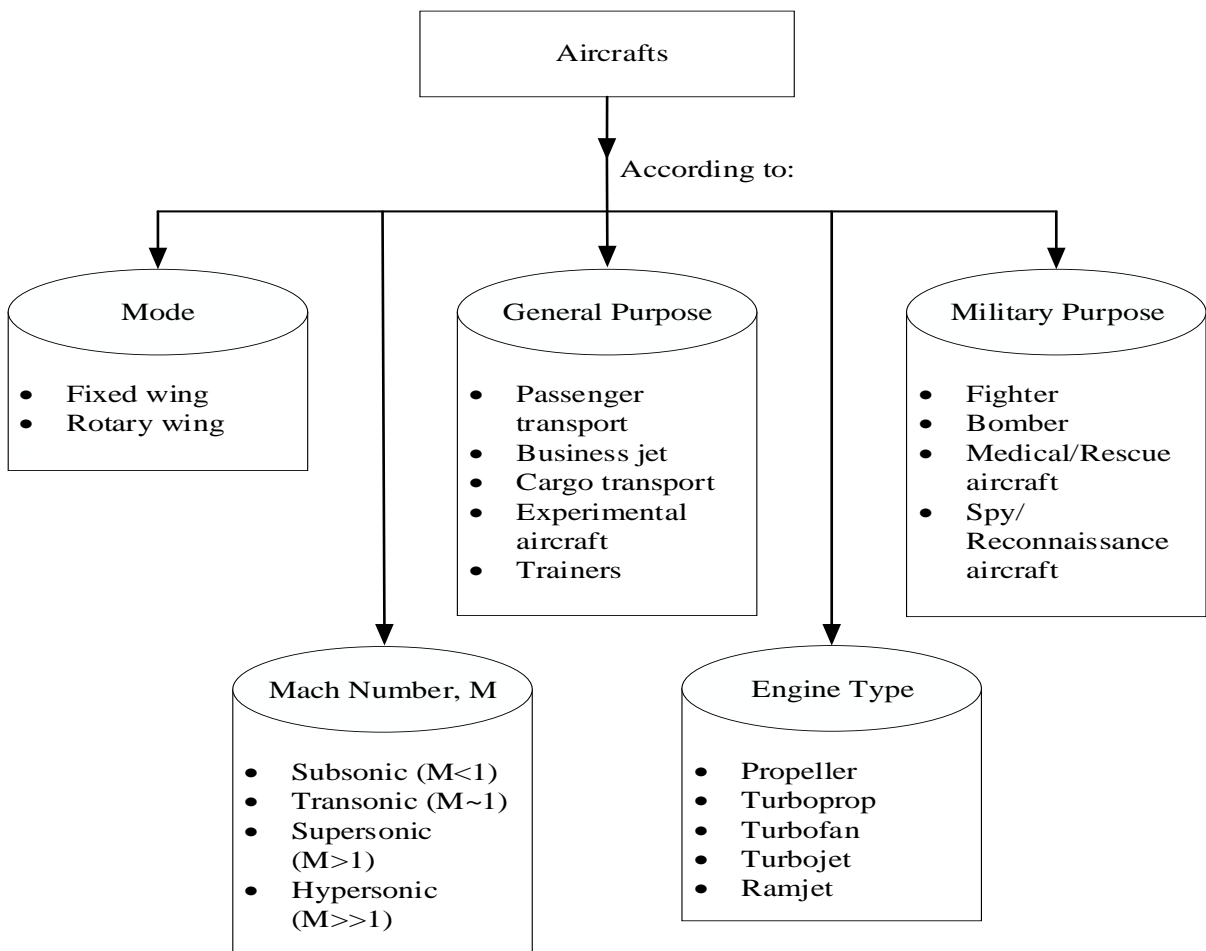
Fig. 2.6 The Classification of Aircrafts

2.2.2 Degrees of Freedom of an Aircraft

The Degrees of Freedom (DoF) of a system is defined as the number of independent restraints necessary to determine the geometric stability of a member or of a frame as a whole, relative to some reference member or system of co-ordinates (Wang *et al.*, 2015). Each co-ordinate may be looked upon as a restraint which removes one DoF from the member or frame under consideration. A member, freely movable in a plane has three DoF or three possible movements, thereby requiring three co-ordinates or restraints in the plane to fix it in a stable manner with respect to the reference member or system of axes. A member movable in space has in general six DoF or six possible movements: three linear translations and three rotations. Six DoF are specific parameter counts for the number of DoF an object has in three-dimensional space, such as the real world. It means that there are six parameters or ways that the body can move (Elmajdub and Manish, 2017). Six DoF consists of the following movement parameters (Fallavollita *et al.*, 2012):

Translation: Moving along the different axes X, Y and Z:

    i.   Moving up and down along the Y axis is called heaving.

    ii.   Moving forwards and backwards along the X axis is called surging.

    iii.   Moving left and right along the Z axis is called swaying.

Rotation: Turning in order to face a different axis (Yang, 2016):

    i.   Moving between X and Y is called pitch.

    ii.   Moving between X and Z is called yaw.

    iii.   Moving between Z and Y is called roll.

An aircraft requires control surfaces to fly and move in different directions. They make it possible for the aircraft to roll, pitch and yaw. Fig. 2.7 (Younes *et al.*, 2015) shows the three axes along which the three primary flight control surfaces tilt.
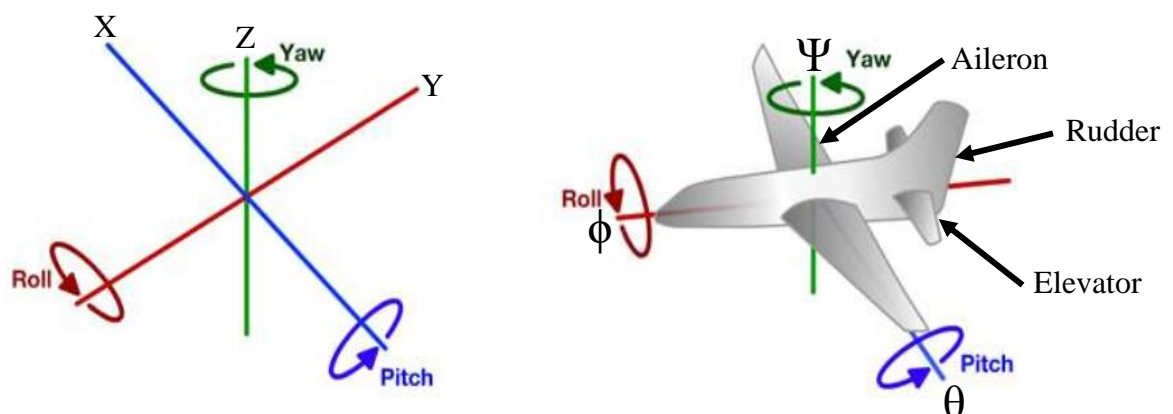
Fig. 2.7 The Six Degrees of Freedom of an Aircraft

The ailerons, operated by turning the control column, cause it to roll. The elevators are operated by moving the control column forward or back causing the aircraft to pitch. The rudder is operated by rudder pedals that make the aircraft yaw. Depending on the kind of aircraft, the requirements for flight control surfaces vary greatly. Primary control surfaces are incorporated into the wings and empennage for almost every kind of aircraft. These surfaces are typically: the elevators included on the horizontal tail to control pitch; the rudder on the aircraft tail for yaw control and the ailerons outboard on the wings to control roll. These surfaces are continuously checked to maintain safe aircraft control and they are normally trailing edge types.

2.3   The Fixed Wing Aircraft

Fig. 2.7 (Kumar and Padture, 2018) shows an aircraft with its major outer components labelled. Many of external components of aircraft are constructed with metal alloys. But external components of modern aircraft are made of carbon fiber and a variety of fiberglass resin (Babinsky, 2015).
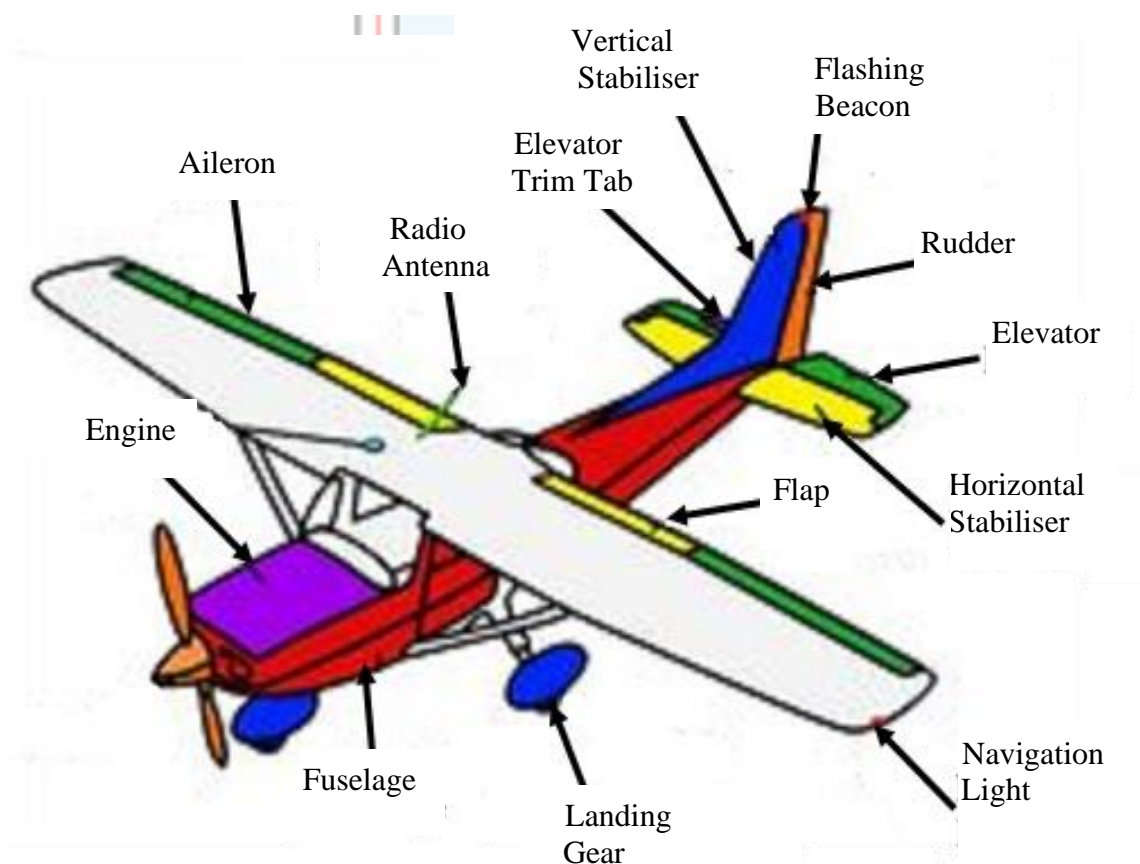
Fig. 2.8 Outer Components of a Fixed Wing Aircraft

2.3.1 Elevator

As the name implies, the elevator helps "elevate" the aircraft. It is located on the tail of the aircraft and directs the nose of the aircraft either upwards or downwards (pitch) in order to make the airplane climb or descend.

2.3.2 Elevator Trim Tab

Trim tabs are small surfaces connected to the trailing edge of a larger control surface on aircrafts. They are used to control the trim of the controls, i.e. to counteract hydro- or aerodynamic forces and stabilise aircrafts in a particular desired attitude without the need for the pilot to constantly apply a control force. This is done by adjusting the angle of the tab relative to the larger surface which is the elevator.

2.3.3 Rudder

The rudder is attached to the vertical stabiliser, which is located on the tail of the aircraft. The rudder helps in steering the nose of aircraft to the left and right. This motion is referred to as yaw. Its main purpose is to counteract certain types of drag, or friction, ensuring that the aircraft's tail follows the nose, rather than sliding out to the side.

2.3.4 Vertical Stabiliser

The vertical stabiliser is designed to stabilise the left-right motion of the aircraft. While most aircraft use a single stabiliser, some models, such as the Lockheed C-69 Constellation use multiple, smaller stabilisers.

2.3.5 Horizontal Stabiliser

The horizontal stabiliser is quite simply an upside-down oriented wing, designed to provide a downward force (push) on the tail. Airplanes are traditionally nose-heavy and this downward force is required to compensate for the weight of the nose portion, keeping the nose level with the rest of the aircraft. Some aircraft can control the angle of the horizontal stabiliser and so therefore, the level of downward force of the nose while in flight, while others are fixed in place.

2.3.6 Flap

Flaps are a 'high lift - high drag' device. Not only do they improve the lifting ability of the wing at slower speeds by changing the camber, or curvature of the wing, but when extended (horizontally) fully they also create more drag. This means an aircraft can descend (or lose altitude) faster, without gaining airspeed in the process.

2.3.7 Antenna

There are numerous radio antennas located around an aircraft, their size and position corresponding to the type of work each antenna must perform and the frequencies being transmitted or received. The Global Position System (GPS) antenna, for example, is always mounted at the top side of an airplane. This is because the GPS satellites are in Space, and therefore always above the aircraft. As a general rule, longer antennas are used for radio communication and navigation at very high frequencies (118 MHz and 136 MHz), while shorter antennas are reserved for higher frequency (900 MHz – 952 MHz) data such as the GPS signals and the transponder, which provides air traffic control with information about the aircraft's position and altitude.

2.3.8 Engine

An aircraft has at least one, or as many as eight engines, which provide the thrust needed to fly. There are many different makes and models of aircraft but all perform the same basic function of taking the air that is in front of the aircraft, accelerating it and pushing it out behind the aircraft. Jet powered aircraft performs this function by compressing the air using turbines, while propeller-powered aircraft use a propeller mounted to the engine. In general, the propeller works like a big screw, pulling the aircraft forward while pushing the air behind it.

2.3.9 Fuselage

This is the portion of the aircraft used to literally join, or fuse, the other parts together. It is commonly thought of as the body of the aircraft and holds the passengers and cargo safely inside.

2.3.10 Navigation Light

A navigation light, also known as a running or position light, is a source of illumination on aircraft. Navigation lights give information on an aircraft position, heading, and status. Navigation lights are not intended to provide illumination for the aircraft making the passage, but rather for other aircraft to be aware of it.

2.3.11 Flashing Beacon

Anti-collision lights, also known as Beacon lights or Strobe lights are a set of lights required on every aircraft to improve visibility to others. Beacon lights are flashing red lights fitted on the top and bottom fuselages of an aircraft. Their purpose is to alert ground crew and other aircraft that an engine is starting up, running or shutting down, or that the aircraft is about to start moving. They spin to produce a flashing effect, increasing the chance they will be noticed.

2.3.12 Aileron

The ailerons are located at the rear of the wing, one on each side. They work opposite to each other, when one is raised, the other is lowered. They are used to increase the lift on one wing while reducing the lift on the other. By so doing, they roll the aircraft sideways, causing the aircraft to turn. This is the primary method of steering a fixed-wing aircraft.

2.4   Additional Components of Aircraft Control Surfaces

The following components (not indicated on Fig. 2.8) are the additional aircraft control surfaces that aid its safe operations.

2.4.1 Slat

A slat is a "high lift" device typically found on jet-powered aircraft. Slats are similar to the flaps except they are mounted on the leading edge of the wing. They also assist in changing the camber, or curvature of the wing, to improve lifting ability at slower speeds.

2.4.2 Spoiler

The spoiler's function is to disrupt, or spoil, the flow of air across the upper surface of the wing. They are usually found on larger aircraft, which can have two types installed. The in-flight spoilers are small and designed to reduce the lifting capability of the wing just enough to allow the aircraft to descend quicker without gaining air speed. Although the flaps can

also perform this function, the spoiler is intended to be used temporarily, while the flaps are typically used for longer durations such as during the approach and landing. The ground spoilers are typically deployed automatically on landing and are much larger than their in-flight spoilers. They are used to completely destroy the lifting ability of the wing upon landing, ensuring that the entire weight of the airplane rests firmly on the wheels, making the brakes more effective and shortening the length of runway needed to stop the aircraft.

2.4.3 Cockpit

The cockpit, sometimes referred to as the "flight deck", is where the pilots sit. It contains the flight controls, which move the airplane, as well as all the buttons and switches used to operate the various aircraft systems.

2.4.4 Empennage

The empennage is the name given to the entire tail section of the aircraft, including both the horizontal and vertical stabilisers, the rudder and the elevator. As a combined unit, it works identically to help guide the aircraft to its destination.

2.4.5 Wheel

The wheels are another part of the undercarriage, or landing gear. While most aircraft have a minimum of three wheels, larger aircraft require many more to support the immense weight. Typically, aircraft wheels are filled with nitrogen instead of air. This is because the pressure of nitrogen gas changes very little with changes in altitude or temperature, which are constantly experienced by the aircraft.

2.4.6 Windshield

The windshield on smaller aircraft is usually made from polycarbonate, a type of plastic, while pressurised aircrafts use a sandwich of plastic and glass layers, called a laminate, up to 20 mm thick. This is necessary to absorb the impact of birds, insects and other debris that may collide with the windshield as the airplane flies at close to the speed of sound.

2.4.7   Wing

The wing provides the majority of the lift an aircraft requires for flight. Its shape is specifically designed for the aircraft to which it is attached. On most aircraft, the interior of the wing is also used to store the fuel required to power the engines.

2.4.8   Winglet

Some aircraft wings have an additional component called a winglet, which is located at the end of each wing. Its purpose is to reduce the drag (or air resistance) the wing produces as it pushes through the air. This not only allows the aircraft to fly faster, but also means it burns less fuel, allowing it to fly longer distances without refuelling.

2.5   Operations of the Fixed Wing Aircraft

Fixed wing aircraft consists of fuselage, wings, stabilisers, flight control surfaces (Elevator, Rudder and Aileron) and landing gear. It also operates on four main forces namely, thrust, drag, lift and weight. Understanding how these forces work and knowing how to control them with the use of power and flight controls are essential to a successful flight. Fig. 2.9 (Tonti, 2014) shows the positions of the four main forces on an aircraft.
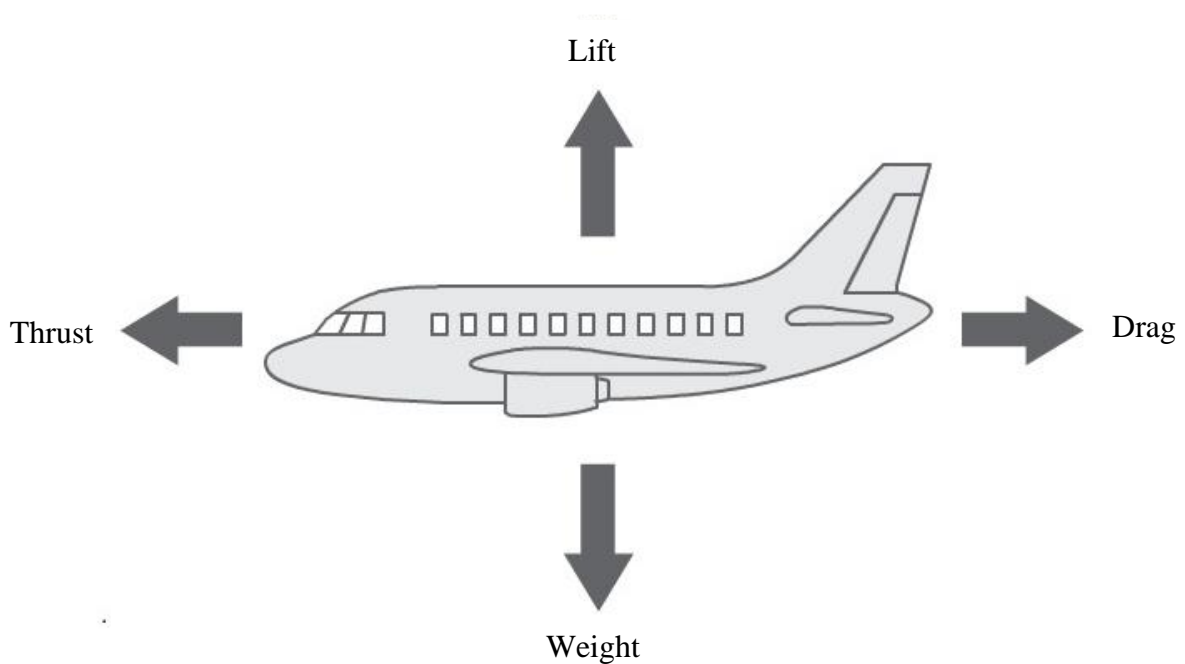
Fig. 2.9 The Four Forces Acting on an Aircraft

Thrust: Thrust is the force which moves an aircraft longitudinally through the air. This forward acting force is produced by the power plant/propeller or rotor. It opposes or overcomes the force of drag. It acts parallel to the longitudinal axis. Equation (2.1) (Peixoto *et al*., 2017) explains the formula for the thrust (force) of an aircraft.

$$F = \frac{\left([MV]_e - [MV]_o\right)}{(t_e - t_o)} = m^*_e V_e - m^*_o V_o \qquad (2.1)$$

where, F = thrust, (N)

$[MV]_e$ = final momentum of the aircraft (kg.m/s)

$[MV]_o$ = initial momentum of the aircraft (kg.m/s)

t_e = final time (s)

t_o = initial time (s)

m_e^* = final mass flow rate (kg/s)

V_e = final velocity of air (m/s)

m_o^* = initial mass flow rate (kg/s)

V_o = initial velocity of air (m/s)

Drag: A rearward, retarding force caused by disruption of airflow by the wing, rotor, fuselage, and other protruding objects. Drag opposes thrust and acts rearward parallel to the relative wind. Equation (2.2) (Narasimhulu *et al*., 2018) shows how the drag of an aircraft is calculated.

$$D = C_D \times d \times \frac{V^2}{2} \times A \qquad (2.2)$$

where, D = drag (N)

d = density of air (kg/m^3)

C_D = drag coefficient,

V = velocity of air (m/s)

A = surface area of the wing (m^2)

Weight: Weight of the aircraft is the combined load of the aircraft itself, the crew, fuel, and cargo or baggage. Weight pulls the aircraft downward because of the force of gravity. It opposes lift and acts vertically downward through the aircraft's center of gravity. Equation (2.3) (Von Braitn, 2014) explains the formula for the weight (force) of an aircraft.

$$W = mg \qquad\qquad (2.3)$$

where, W = weight (N)

  m = total mass of aircraft (kg)

  g = acceleration due to gravity (m/s^2)

Lift: Lift is an aerodynamic force produced by the motion of an aircraft through the air. It opposes the downward force of weight produced by the dynamic effect of the air acting on the airfoil and acts upwards perpendicular to the flight path through the center of gravity. Equation (2.4) (Dole *et al.*, 2016) is the formula for lift.

$$L = C_L \times d \times \frac{V^2}{2} \times A \qquad\qquad (2.4)$$

where, L = lift (N)

  C_L = lift coefficient

2.5.1   How Lift is Generated

Lift is generated when an object changes the direction of flow of a fluid or when the fluid is forced to move due to the object passing through it. When the object and fluid move relative to each other and the object turns the fluid flow in a direction perpendicular to that flow, the force required to do this work creates an equal and opposite force that is called lift. The object may be moving through a stationary fluid, or the fluid may be flowing past a stationary object and these two motions are effectively identical in principle. The lift generated by an airfoil depends on the following factors:

  i. Speed of the airflow;

  ii. Density of the air;

  iii. Total area of the segment or airfoil; and

  iv. Angle of attack between the air and the airfoil.

The angle of attack is the angle at which the airfoil meets the oncoming airflow or vice versa (Babinsky, 2015). A symmetric airfoil must have a positive angle of attack to generate positive lift. At a zero angle of attack, no lift is generated. At a negative angle of attack negative lift is generated. A cambered or nonsymmetrical airfoil may produce positive lift at zero, or even small negative angle of attack. However, the details of how the relative

movement of air and airfoil interact to produce the turning action that generates lift are complex. In causing lift of an angled flat plate, revolving cylinder, airfoil, etc., the flow meeting the leading edge of the object is forced to split, in direction over and under the object. The sudden change in direction over the object causes an area of low pressure to form behind the leading edge on the upper surface of the object. In turn, due to this pressure gradient and the viscosity of the fluid, the flow over the object is accelerated down along the upper surface of the object. At the same time, the flow forced under the object is rapidly slowed or stagnated causing an area of high pressure. This also causes the flow to accelerate along the upper surface of the object. The two sections of the fluid each leave the trailing edge of the object with a downward component of momentum, producing lift. Figure 2.10 (Schade *et al*., 2016; Debiasi *et al*., 2016) shows how lift of aircraft is generated.
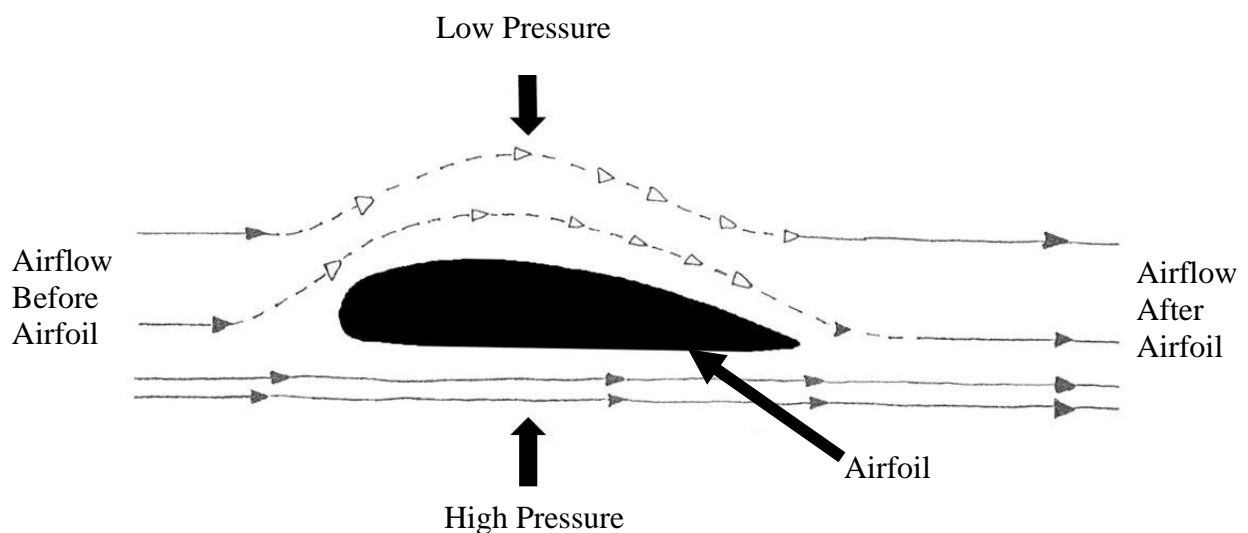
Fig. 2.10 Generation of Lift

Bernoulli's principle, which explains why an airfoil develops an aerodynamic force, describes the relationship between internal fluid pressure and fluid velocity. It is a statement of the law of conservation of energy which states that energy cannot be created or destroyed and the amount of energy entering a system must exit in same amount. A simple tube with a constricted portion near the center of its length illustrates this principle. An example is running water through a garden hose. The mass of flow per unit area (cross-sectional area of tube) is the mass flow rate. In Figure 2.11 (Poulad *et al.*, 2011)*,* the flow into the tube is constant, neither accelerating nor decelerating thus, the mass flow rate through the tube must be the same at Stations 1, 2, and 3.
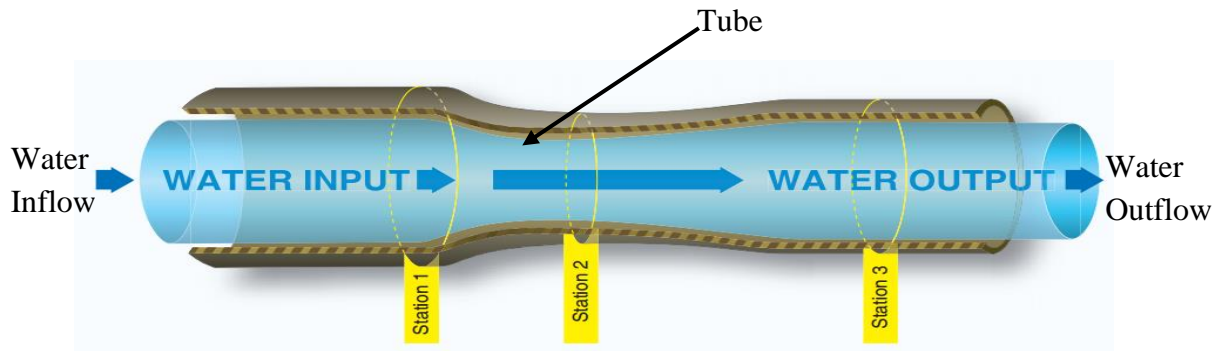
Fig. 2.11 Illustration of Bernoulli's Principle

If the cross-sectional area at any one of these stations or any given point in the tube is reduced, the fluid velocity must increase to maintain a constant mass flow rate to move the same amount of fluid through a smaller area. Fluid speeds up in direct proportion to the reduction in area and Venturi effect is the term used to describe this phenomenon. Equation (2.5) (Abrate, 2016) gives the initial and final energy per unit volume relationship.

$$P_1 + \frac{1}{2}\rho v_1^2 + \rho gh_1 = P_2 + \frac{1}{2}\rho v_2^2 + \rho gh_2 \qquad (2.5)$$

where, P_1 = initial pressure of fluid at the cross section (Pa)

P_2 = final pressure of fluid at the cross section (Pa)

ρ = density of the flowing fluid (kg/m^3)

g = acceleration due to gravity (m/s^2)

v_1 = initial mean velocity of fluid flow at the cross section (m/s)

v_2 = final mean velocity of fluid flow at the cross section (m/s)

h_1 = initial elevation head of the center of the cross section with respect to a datum (m)

h_2 = final elevation head of the center of the cross section with respect to a datum (m)

2.5.2 Venturi Flow

While the amount of total energy within a closed system (the tube) does not change, the form of the energy may be altered. Pressure of flowing air may be compared to energy in that the total pressure of flowing air always remains constant unless energy is added or removed. Fluid flow pressure has two components: Static and dynamic pressure. Static

pressure is the pressure component measured in the flow but not moving with the flow as the pressure is measured. Static pressure is also known as the force per unit area acting on a surface. Dynamic pressure of flow is that component existing as a result of movement of the air. The sum of these two pressures is the total pressure. As air flows through the constriction, static pressure decreases as velocity increases. This increases dynamic pressure. Figure 2.12 (Qu *et al.*, 2015) shows the bottom half of the constricted area of the tube, which resembles the top half of an airfoil. Even with the top half of the tube removed, the air still accelerates over the curved area because the upper air layers restrict the flow just as the top half of the constricted tube does. This acceleration causes decreased static pressure above the curved portion and creates a pressure differential caused by the variation of static and dynamic pressures (Hess, 2016).
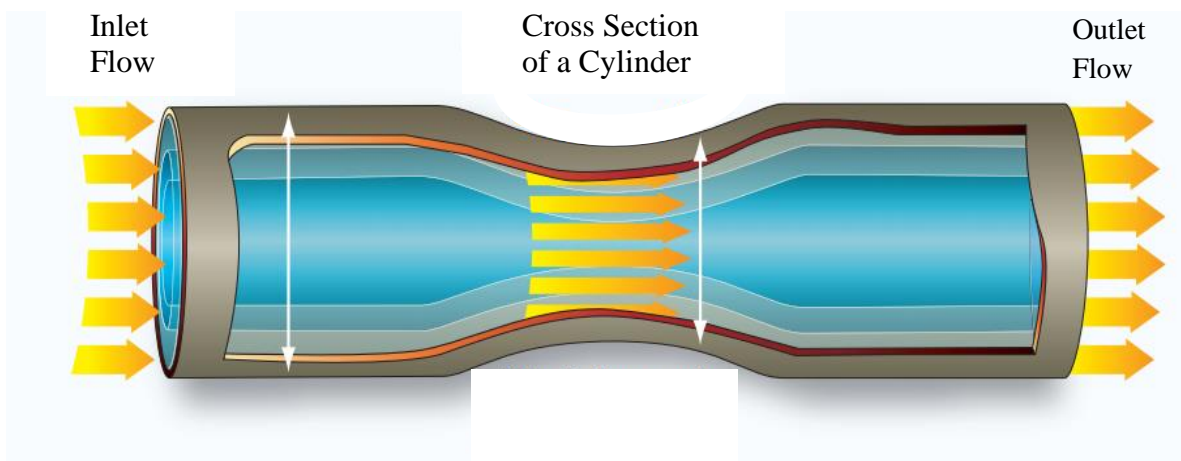
Fig. 2.12 Illustration of the Effect of Venturi Flow

2.6   Operations of the Rotary Wing Aircraft

The main difference between fixed-wing and rotary-wing aircraft is the way lift is generated. The fixed-wing aircraft as stated earlier gets its lift from a fixed airfoil surface whiles the rotary-wing type gets lift from rotating airfoils called rotor blades. Typically, an helicopter is a rotary wing aircraft. An helicopter uses two or more engine-driven rotors from which it gets lift and propulsion. The airfoils of an helicopter are perfectly symmetrical. This means that the upper and lower surfaces are shaped the same. The symmetrical airfoil is used on the helicopter because the center of pressure across its surface is fixed. On the fixed-wing airfoil, the center of pressure moves fore and aft, along the chord line, with changes in the angle of attack. If this type of airfoil were used on a rotary-wing aircraft, it would cause the rotor blades to jump around (dive and climb) uncontrollably (Anon., 2016). With the

symmetrical airfoil, this undesirable effect is removed. The airfoil, when rotated, travels smoothly through the air. The main rotor of a helicopter consists of two or more rotor blades.

Lift is generated by rotating the blades through the air at a high. Lift may be changed by increasing the angle of attack or pitch of the rotor blades. When the rotor is turning and the blades are at zero angle (flat pitch), no lift is developed. This feature provides the pilot with complete control of the lift developed by the rotor blades. A pilot controls the direction of flight of the helicopter by tilting the main rotor. If the rotor is tilted forward, the force developed by the rotor is directed downward and aft. Applying Newton's third law of motion (action and reaction are equal), lift will be developed in an upward and forward direction, and the helicopter will tend to rise and move forward. From this, the pilot can move the helicopter forward or rearward, or to the right or left, simply by tilting the main rotor in the desired direction. The helicopter can move in any direction, with or without forward movement. Fig. 2.13 (Badick *et al*., 2016) shows the directions of the four main forces on the helicopter.
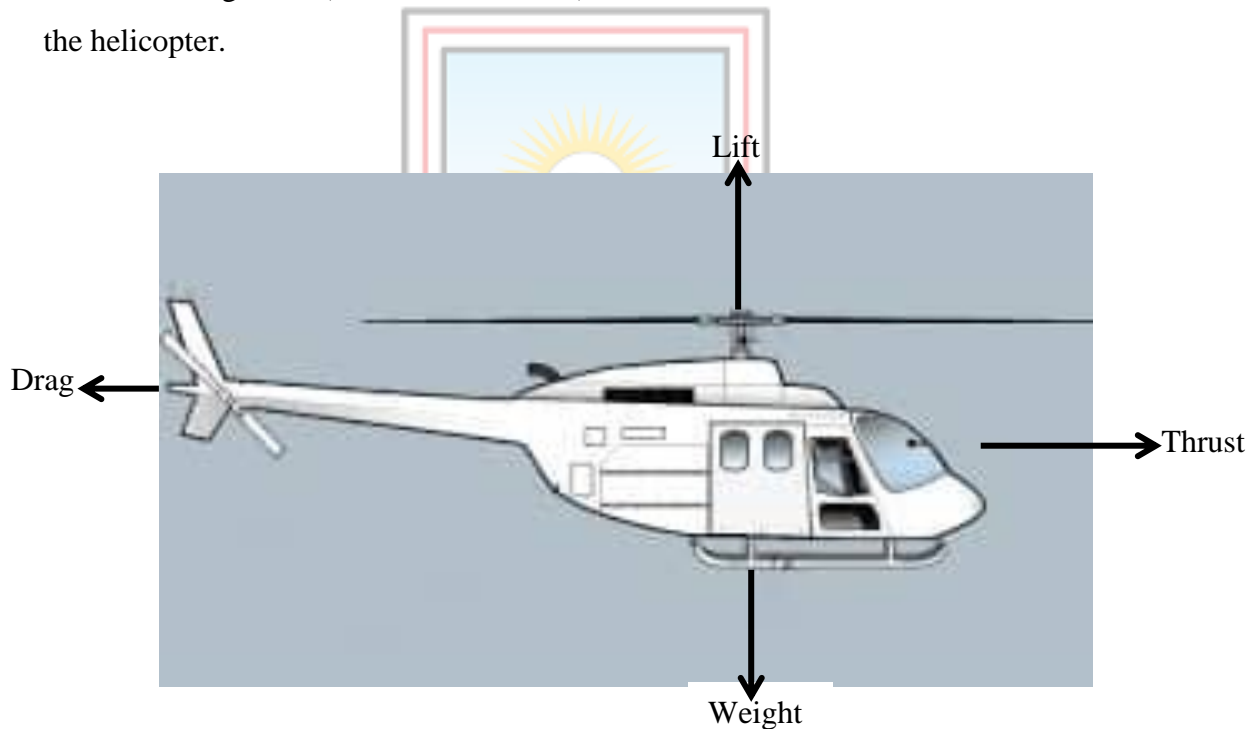
Fig. 2.13 The Four Forces on an Helicopter

An helicopter has the ability to remain in one spot in the air with little or no movement in any direction (hovering). This is done by equalising all the four forces acting on the helicopter (lift, drag, weight, and thrust). This action also allows an helicopter to take off or land without a runway. As the helicopter's main rotor turns in one direction, the body (fuselage) of the helicopter tends to rotate in the opposite direction (Newton's third law).

This is known as torque reaction. In a single main rotor helicopter, the usual way of getting rid of torque reaction is by using a tailed rotor (anti-torque rotor). This rotor is mounted vertically on the outer portion of the helicopter's tail section. The tail rotor produces thrust in the opposite direction of the torque reaction developed by the main rotor (Coban *et al.*, 2017).

2.7   Aircraft Landing Gear

Aircraft landing gear is the undercarriage of an aircraft or spacecraft and may be used for either takeoff or landing. The landing gear supports the aircraft when it is not flying, allowing it to take off, land, and taxi without damage. Wheels are typically used but skids, skis, floats or a combination of these and other elements can be deployed depending on the surface and on whether the aircraft only operates vertically or is able to taxi along the surface (Petrescu *et al.*, 2017). Faster aircraft usually have retractable undercarriages, which fold away during flight to reduce air resistance or drag (Wen, 2009). Fig. 2.14 (Keane *et al.*, 2017) shows the landing gear of an aircraft.
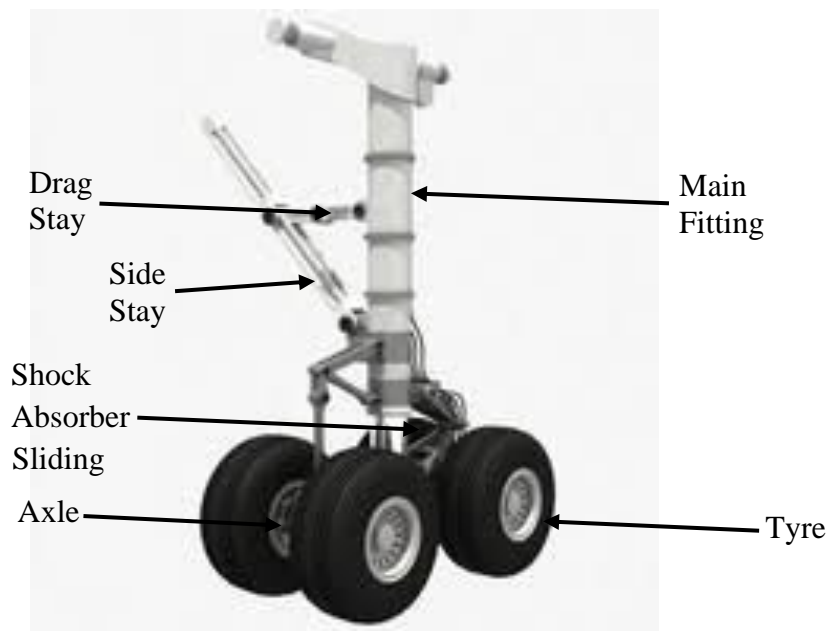
Fig. 2.14 The Aircraft Landing Gear

2.8   Aircraft Autopilot System

An autopilot is a flight control system that allows a pilot to fly an airplane without continuous hands-on control of the airplane (Anon., 2015; Ferreira *et al.,* 2018). It allows the pilot to focus on higher-order tasks such as navigating, communicating with air traffic control, planning for weather contingencies and rerouting associated with any kind of

emergency circumstance. An AAS works by sending signals to the flight control system. The pilots input what type of mode they want, like a heading hold mode or an altitude hold mode. If the pilots want to hold a specific altitude, or the height of the plane, they could designate that as well. More sophisticated autopilot systems can actually maintain a navigational course. Pilots do three things when they fly the airplane: they aviate, that is actual hands-on, stick-and-rudder control; they navigate, which is actually planning a route or course and thirdly, they communicate. Pilots have to communicate with Air Traffic Control (ATC), look at on-board systems to maintain the status of the mechanical components of the aircraft, and plan for weather contingencies. The autopilot performs one of those three tasks and alleviates the pilot from actually aviating. Fig. 2.15 (Wargo *et al.*, 2014) shows the location of the autopilot system for a typical trainer aircraft.
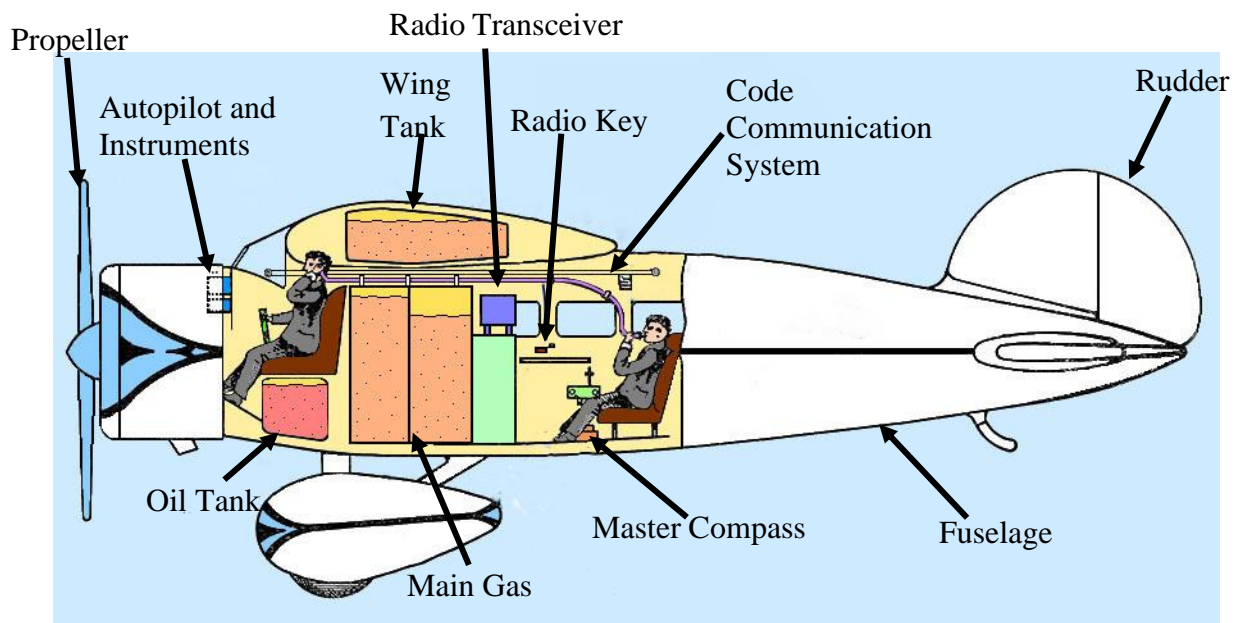
Fig. 2.15 Trainer Aircraft depicting Location of the Autopilot System

A typical AAS comprises mainly sensors subsystem, computer and controls and the loads. There are numerous sensors that are used to measure the operating parameters of the aircraft. The computer and controls see to the manipulation of the operating parameters of the aircraft and then send signals to the controls to operate the loads. The loads are the elevator, aileron, rudder and aircraft trim system. They are used for safe and smooth operation of the aircraft. Figure 2.16 (Akyürek, 2016) shows the block diagram of an AAS.
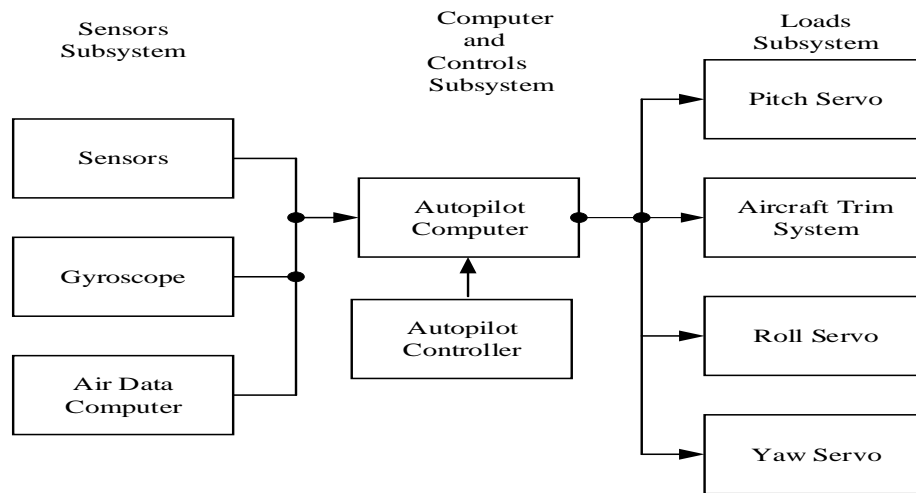
Fig. 2.16 Block Diagram of an Aircraft Autopilot System

2.8.1   Sensors Subsystem

The sensors subsystem comprises sensors, gyroscope and the air data computer.

Sensors

Sensors are used to send data to the autopilot computer, which processes the information and transmits its output signals to the servo to move the control surfaces and also change the attitude of the aircraft (Goupil, 2011; Ribeiro and Oliveira, 2010).

Gyroscope

Normally, the typical mechanical gyroscope is considered a motorised gyroscope. Its angular momentum interacts with the force produced by the earth's rotation to maintain a north-south orientation of the gyroscopic spin axis, thereby providing a stable directional reference (Chen *et al*., 2012). Recent research however has rendered the MEMS gyroscope as a potential alternative to the hitherto usable mechanical type.

Air data computer

Air data computer is an electronic digital computer in aircrafts that senses or computes static and pitot pressure, outside air and total air temperature. Air Data's line of Air Data Computer (ADC) are designed to measure and compute navigation parameters in aircraft, high speed military trainers, helicopters and Unmanned Aerial Vehicles (UAV). Parameters such as pressure, altitude, baro-corrected altitude, altitude rate of change, computed and true airspeeds, mach number and static air temperature are computed. A comprehensive Built-in Test (BiT) function that provides high-reliability fault detection and isolation capability is

also one of its features. It is extremely robust and provides standard pitot and static tubing interface (Karlgaard *et al*., 2017).

2.8.2   Computer and Controls Subsystem

The subsystem is made up of the autopilot computer and controller.

Autopilot computer

The heart of a modern Automatic Flight Control System (AFCS) is a computer with several high-speed processors. To gather the intelligence required to control the aircraft, the processors communicate with sensors located on the major control surfaces. They also collect data from other aircraft systems and equipment, including gyroscopes, accelerometers, altimeters, compasses and airspeed indicators. The processors in the AFCS then take the input data and, using complex calculations, compare it to a set of control modes. A control mode is a setting entered by the pilot that defines a specific detail of the flight. There are also control modes that maintain airspeed, heading and flight path. These calculations determine if the aircraft is obeying the commands set up in the control modes. The processors then send signals to various servomechanism units (Peck *et al*., 2015).

Autopilot controller

An autopilot controller is a device that keeps aircraft moving in a particular direction without human involvement. An AFCS works by sending signals to the flight control system. The pilot inputs what type of mode is required, like a heading hold mode or an altitude hold mode. To hold a specific heading, or direction, the pilot pushes a button and specifies some values like 3-6-0 for north or 1-8-0 for south. If the pilots want to hold a specific altitude, or the height of the aircraft, they could designate that as well. The pilot selects each maneuver and makes small inputs into an autopilot controller (Sarter *et al*., 2015).

2.8.3   Loads Subsystem

A servomechanism, is a device that provides mechanical control at a distance. One servo exists for each control surface included in the autopilot system. The servos take the computer's instructions and use motors or hydraulics to move the aircraft's control surfaces, making sure the aircraft maintains its proper course and attitude. The pitch, roll, yaw servos and the aircraft trim system constitute the load subsystem.

Pitch servo (Elevator)

The elevator is a moveable part of the horizontal stabiliser, hinged to the back of the fixed part of the horizontal tail. The elevators move up and down together with the help of the pitch servo. When the pilot pulls the stick backward, the elevators go up. Pushing the stick forward causes the elevators to go down. Raised elevators push down on the tail and cause the nose to pitch up. This makes the wings fly at a higher angle of attack, which generates more lift and more drag. Centering the stick returns the elevators to neutral and stops the change of pitch (Hamel, 2017). Fig. 2.17 (Laith, 2018) gives the pitch servo control system and Equation (2.6) (Kumar and Dahiya, 2016) the transfer function of the pitch servo.
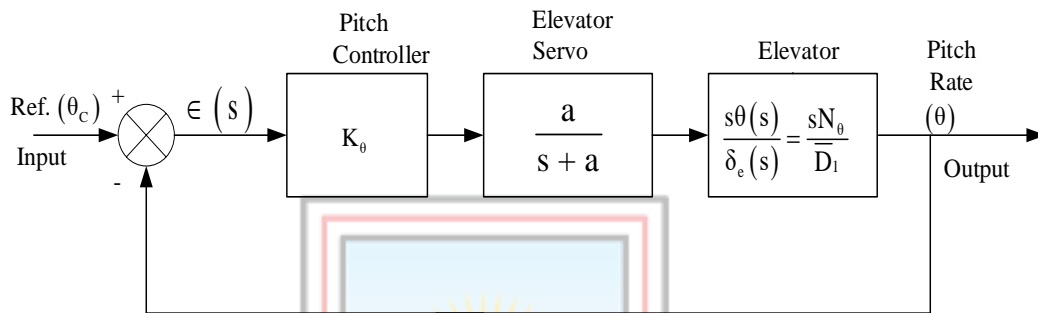
Fig. 2.17 Control System of the Pitch Servo

$$\frac{\delta_e}{\upsilon} = \frac{k_a}{\tau s + 1} \tag{2.6}$$

where, δ_e = elevator deflection angle, (rad or deg)

v = input voltage, (volt)

k_a = elevator servo gain

τ = servomotor time constant

Roll servo (Aileron)

Ailerons are mounted on the trailing edge of each wing near the wingtips and move in opposite directions by the roll servo. When the pilot moves the stick to the left, the aileron on the left wing goes up and the aileron on the right wing goes down. A raised aileron reduces lift on that wing where it is located and a lowered one increases the lift, so moving the stick left causes the left wing to drop and the right wing to rise. This causes the aircraft to roll to the left and begin to turn to the left. Centering the stick returns the ailerons to neutral position. The aircraft will continue to turn until opposite aileron motion returns the bank angle to zero to fly straight. Fig. 2.18 (Minoura *et al.*, 2009) shows the control system

27

of the roll servo and Equation (2.7) (Saeed *et al*., 2015) gives the transfer function of the roll servo.
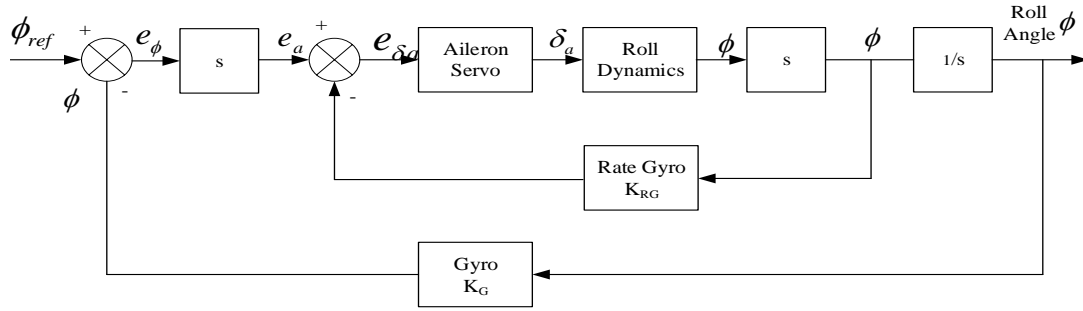
Fig. 2.18 Control System of the Roll Servo

$$\frac{\phi(\text{s})}{\delta_a(\text{s})} = \frac{C_{l_{\delta a}}}{s\left(\dfrac{J}{qSb}s - \dfrac{b}{2v}C_{l_p}\right)} \tag{2.7}$$

where, ϕ = roll angle (deg)

    δ_a = aileron deflection angle (deg)

    J = moment of inertia about the roll axis (kg m^2)

    S = platform area (m^2)

    b = wing span (m)

    q = dynamic pressure (N/m^2)

    C_{l_p} = stability derivative representing damping in roll (/rad)

    $C_{l_{\delta a}}$ = stability derivatives representing the rolling moment due to aileron deflection

       angle (deg)

Yaw servo (Rudder)

The rudder is typically mounted on the trailing edge of the vertical stabiliser, part of the empennage. When the pilot pushes the left pedal, the rudder deflects left by taking command from the yaw servo. Pushing the right pedal causes the rudder to deflect right. Deflecting the rudder to the right pushes the tail of aircraft left and causes the nose to yaw to the right. Centering the rudder pedals returns the rudder to neutral and stops the yaw. The control system of the yaw servo is presented in Fig. 2.19 (Ramesh *et al*., 2012) and the corresponding transfer function is given by Equation (2.8) (Huajun *et al*., 2012).
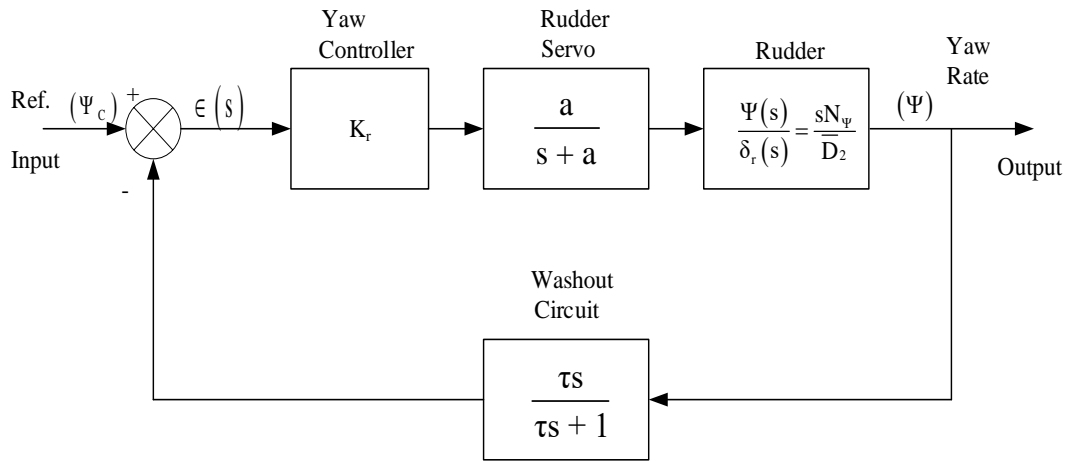
Fig. 2.19 Control System of the Yaw Servo

$$\frac{\delta_e}{\upsilon} = \frac{k_r}{\tau s + 1} \tag{2.8}$$

where, δ_e = rudder deflection angle (deg)

      v = input voltage (volt)

      τ = servomotor time constant

      k_r = rudder servo gain

Aircraft trim system

These are small surfaces connected to the trailing edge of a larger control surface on aircrafts, used to counteract hydro or aerodynamic forces and stabilise the aircraft in a particular desired attitude without the need for the pilot to constantly apply a control force. This is done by adjusting the angle of the trim tab relative to the larger surface. Changing the setting of the trim tab adjusts the neutral or resting position of a control surface (such as an elevator or rudder).

2.9 Microelectromechanical System Gyroscopes

Microelectromechanical System (MEMS) gyroscopes are devices within the scale of 1 mm to 1μm that combine electrical components with mechanical systems which use vibrating mechanical elements as a sensing element for detecting angular velocity (Valadeiro *et al*., 2016). They do not have rotating parts that require bearings and this allows an easy miniaturisation and the use of advanced manufacturing techniques. MEMS gyroscopes are fabricated using micromachining techniques and do not rely on a spinning rotor as used in conventional mechanical gyroscopes because fabricating rotating parts with significant

useful mass is difficult at the micro level. All MEMS gyroscopes with a vibrating element are based on the transfer of energy between two vibration modes caused by the acceleration of Coriolis. The Coriolis acceleration, proportional to the angular velocity is an apparent acceleration that is observed in a rotating frame of reference (Zhanshe *et al.*, 2015). The advent of MEMS technology has directly enabled the development of low-cost, low-power sensors and actuators, which are rapidly replacing their macroscopic scale equivalents in many traditional applications most notably, Inertial Measurement Units (IMUs).

A MEMS gyroscope is a sensor that measures the rate of change in the angular position of an object. Majority of MEMS gyroscopes use vibrating mechanical elements to sense angular velocity. A MEMS vibratory gyroscope can be simply visualised as a two DoF (2-DoF) spring-mass-damper system as shown in Fig. 2.20.
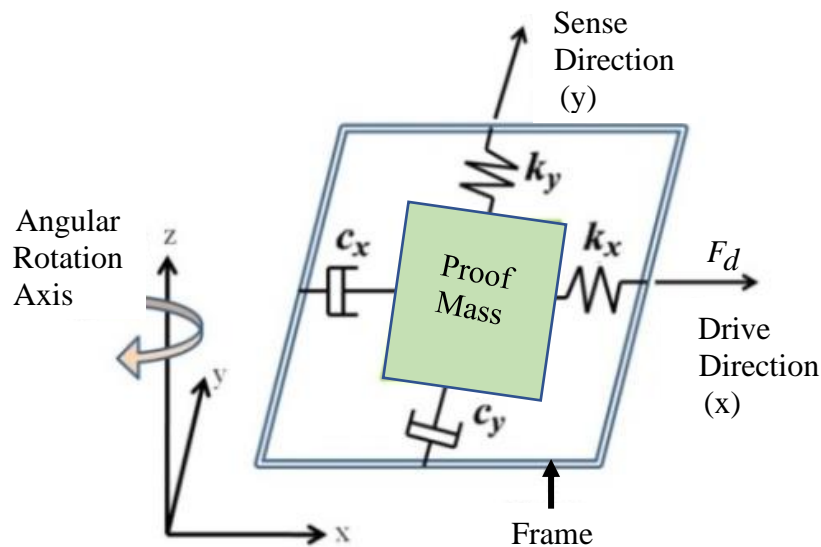
Fig. 2.20 Schematic Illustration of the MEMS Vibratory Gyroscope as a 2-DoF Spring-Mass-Damper System

At the core, it has a vibrating mass (proof mass). The proof mass is suspended above the substrate by use of flexible beams, which also work as mechanical springs. In most MEMS vibratory gyroscopes, the proof mass is subjected to vibration at resonance frequency by the use of an electrostatic force (F_d) causing movement in the drive direction (Kumar and Hemalatha, 2015). When the gyroscope as a sensor experiences an angular rotation, a Coriolis force is induced in the direction orthogonal to both the drive direction (x) and angular rotation axis (z). Coriolis effect is the deflection of moving objects when they are viewed in a rotating reference frame. Equation (2.9) gives the Coriolis force (Zeitlin, 2016).

$$F = 2m\Omega v \qquad\qquad (2.9)$$

where, F = Coriolis force (N/kg)

    m = mass of object (kg)

    Ω = angular speed of rotation (rad/s)

    v = horizontal speed (m/s)

This rotation-induced Coriolis force causes an energy transfer between the drive mode and the sense mode. The proof mass movement caused by the Coriolis force in the sensed direction (y) is proportional to the applied angular rotation and can be measured with differential capacitance techniques by the use of interdigitated comb electrodes. An example of such construction of MEMS vibratory gyroscope is shown schematically in Fig. 2.21 (Kwon *et al*., 2017).
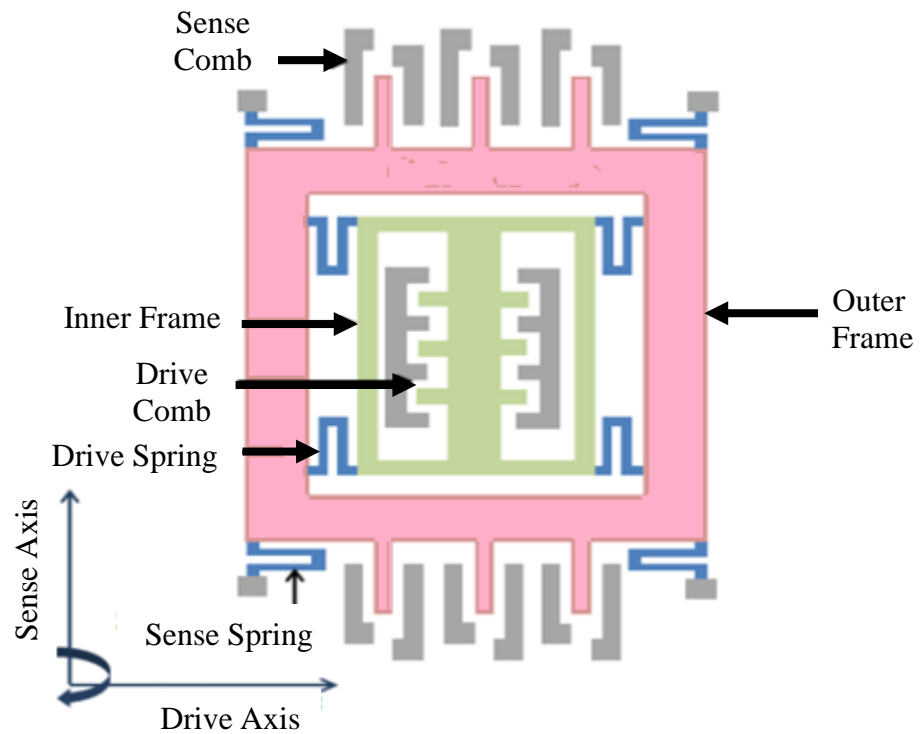
Fig. 2.21 Constructional Features of a MEMS Vibratory Gyroscope

In some cases, a MEMS gyroscope has two proof masses placed on either side that are driven in opposite directions causing the Coriolis force induced on the two masses to be in opposite directions. Fig. 2.22 (Sun and Xie, 2017) depicts the two proof mass type of the MEMS vibratory gyroscope.

31
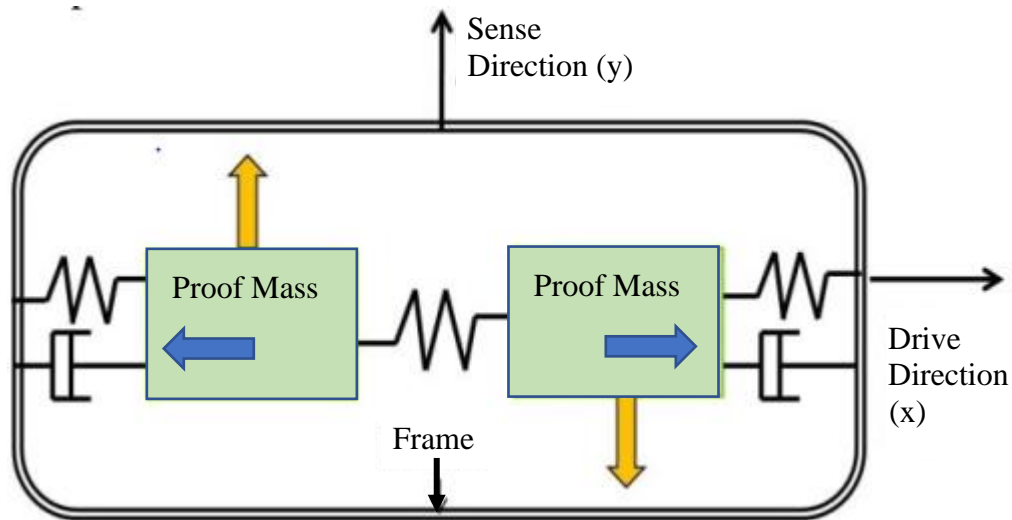
Fig. 2.22 Two Proof Mass-Spring-Damper System Type of MEMS Vibratory Gyroscope

This arrangement helps to nullify the external inertial inputs caused by undesirable ambient vibration and shock. These types of gyroscopes can be used for inertial navigation where single-axis MEMS vibratory gyroscopes are combined and mounted on three Cartesian directions (i.e., X, Y and Z) with other electronic components. This tracking system requires robust and accurate gyroscopes, the performance of which should be maintained within a desired specific range over a specified time period (Patel and McCluskey, 2016).

2.9.1 Degrees of Freedom of MEMS Vibratory Gyroscopes

In order to derive the equation of motion for a MEMS vibratory gyroscope, the system is represented by a spring-mass-damper system. Since the movement of gyroscope structure is modelled while it rotates, motion equations can be represented based on a stationary (gyroscope frame) and non-stationary frame (inertial frame) (Kwon *et al*., 2017). The spring-mass-damper system is initially observed with respect to the gyroscope frame. Once the motion equations have been established, these equations are derived with respect to the inertial frame. Up to four DoF of the MEMS vibratory gyroscope have been reported in the literature and these are presented in Fig. 2.23 (Ivanova *et al*., 2013).
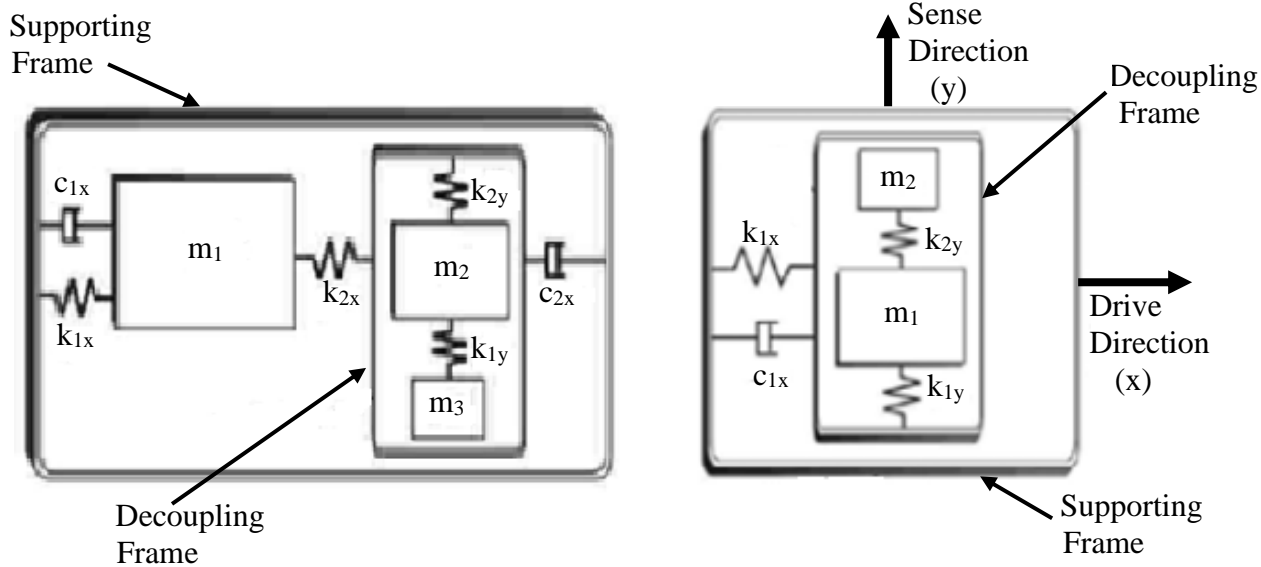
a. Four Degrees of Freedom   b. Three Degrees of Freedom
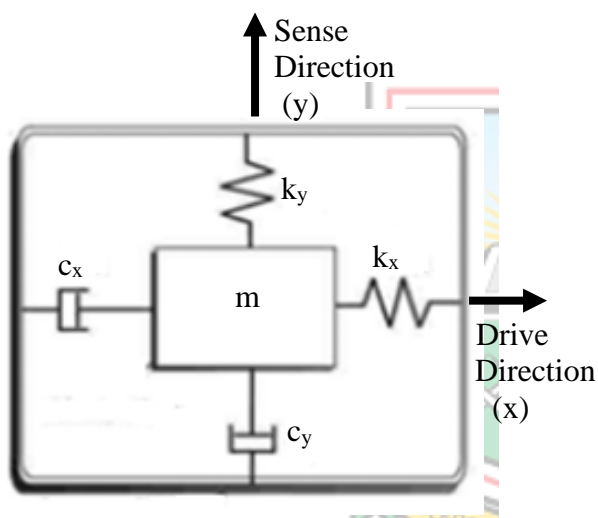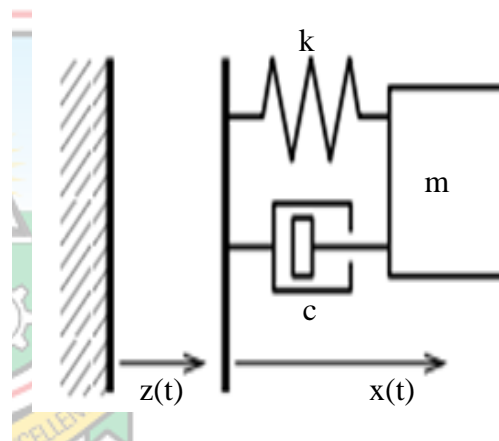
c. Two Degrees of Freedom   d. Single Degree of Freedom

Fig. 2.23 The Degrees of Freedom of a MEMS Vibratory Gyroscope

Four degrees of freedom design

The Four DoF (4-DOF) system is designed with three interconnected proof masses, which provide flexibility in defining the drive and sense mode dynamical parameters (Fig. 2.23a). The approach is based on utilising 2-DoF drive and sense direction oscillators, that form a 4-DoF dynamical system in contrast to the conventional gyroscope approach with a 2-DoF overall dynamical system. This system can be found in applications such as in the automobile industry, electronics and inertial navigation systems for tactical weapons. Specifically, the DoF are heave, roll, pitch and yaw.

Three degrees of freedom design

The aim of a Three DoF design concept is to utilise resonance in either the drive mode or the sense mode, to improve sensitivity while maintaining the robust operational characteristics. A structurally decoupled 2-DoF and single DoF (1-DoF) oscillators are formed in the drive and sense modes (Fig. 2.23b). In the 3-DoF system with 2-DoF drive mode, the wideband region is achieved in the drive-mode frequency response and the device is operated at resonance in the drive mode. This allows utilisation of well-proven drive mode control techniques, while providing robust gain and phase in the sense mode. By utilising dynamic amplification in the drive mode, large oscillation amplitudes of the sensing element is achieved with small actuation amplitudes, providing improved linearity and stability even with parallel plate actuation. Applications of this system can be found in aerospace, down-hole drilling and high-temperature industrial applications. Specifically, the DoF are roll, pitch and yaw.

Two degrees of freedom design

In the 2-DoF MEMS vibratory gyroscope, the proof mass is free to oscillate in two orthogonal directions: the drive – direction, x and the sense – direction, y (Fig. 2.23c). An external sinusoidal force, generally, the electrostatic force is applied by comb-drive structures that put the proof mass into resonance in the drive direction. When the gyroscope performs angular rotation, the Coriolis force is induced in the y direction. If the drive and sense resonant frequencies are matched, the Coriolis force excites the system into resonance in the sense direction. The resulting amplitude of oscillation in the sense direction is proportional to the Coriolis force and the angular velocity to be measured. The sense direction oscillation is detected by air-gap capacitors. Maximum possible gain is achieved when the gyroscopes are designed to operate at or near the peak operation. This is achieved by matching drive and sense resonant frequencies. Some applications of this system are deep energy exploration, navigation and tracking.

Single degree of freedom design

1-DoF system is a spring-mass-damper system in which the spring has no damping or mass, the mass has no stiffness or damping, the damper has no stiffness or mass. But the mass is allowed to move in only one direction (Fig. 2.23d). The horizontal vibrations of a single-storey building can be conveniently modelled as a 1-DoF system. It can be used in automatic door locks.

The equations of motion for the spring-mass-damper system with respect to the gyroscope frame can be represented as in Equations (2.10) and (2.11) (Hakan and Yaralioglu, 2017).

$$ma_x + c_x v_x + k_x x = F_d \tag{2.10}$$

$$ma_y + c_y v_y + k_y y = 0 \tag{2.11}$$

where m = mass of the vibrating structure (kg)

c_x = damping coefficient in the drive direction (Ns/m)

c_y = damping coefficient in the sense direction (Ns/m)

k_x = beam stiffness in the drive direction (N/m)

k_y = beam stiffness in the sense direction (N/m)

a_x = acceleration component in the drive direction (m/s^2)

a_y = acceleration component in the sense direction (m/s^2)

v_x = velocity component in the drive direction (m/s)

v_y = velocity component in the sense direction (m/s)

F_d = electrostatic force applied by the drive comb (N)

If these equations are viewed from an inertial frame, according to Hakan and Yaralioglu (2017), they can be represented by Equations (2.12) and (2.13), respectively.

$$m\ddot{x} + c_x \dot{x} + k_x x = F_d + 2m\Omega\dot{y} \tag{2.12}$$

$$m\ddot{y} + c_y \dot{y} + k_y y = -2m\Omega\dot{x} \tag{2.13}$$

The $2m\Omega\dot{y}$ and $2m\Omega\dot{x}$ are the rotation-induced Coriolis terms. When the gyroscope starts vibrating in the drive direction and experiences external angular rotation, these Coriolis terms cause dynamic coupling between the drive and sense modes of vibration, and the suspended proof mass starts to vibrate in the sense direction as a result of the coupling. Furthermore, parasitic coupling between the drive and sense axes introduces unwanted bias (offset) errors due to deterministic or stochastic noise sources. As a consequence, if the orientation of the platform to which a vibrating body is attached is changed, the vibrating

body will exert a force on the platform. This force can be measured and can be used to find the output of the gyroscope.

The advantages of MEMS vibratory gyroscopes include the following (Passaro *et al.,* 2017):

    i.   Extremely space efficient: Available in the form of chips, so they can be fitted on electronic circuits;

    ii.   Adequate performance: As the technology is evolving, the performance accuracy of MEMS vibratory gyroscopes is also improving;

    iii.   No moving components hence, completely maintenance free; and

    iv.   Available at a fraction of the cost of rotary and optical gyroscopes.

The demerits of MEMS vibratory gyroscopes are (Xie and Fedder, 2016):

    i.   Plant establishment requires huge investment;

    ii.   Micro components are costly;

    iii.   Prior knowledge is required to handle them; and

    iv.   Procedure for design is complex.

Despite the disadvantages, MEMS vibratory gyroscopes measure angular rotations about specific axes with respect to an inertial reference frame and have found broad applications in aircrafts, automotive (rollover detection, anti-sliding control, and GPS), consumer electronics (game consoles, camera image stabilisation, cell phone, and 3-D mouse) and medical device applications.

2.9.2 Characterisation of MEMS Vibratory Gyroscopes

MEMS vibratory gyroscopes are associated with a number of parameters which are important with regard to selection for an application. Table 2.1 gives the important parameters usually directed in a typical data sheet of a MEMS vibratory gyroscope.

Table 2.1 A Typical Data Sheet of MEMS Vibratory Gyroscope

SN	Parameter	Symbol	Value
1.	Scale Factor (mv/(°/s))	$g_{i.SFerr}$	15.7
2.	Bias Error (°/h)	$g_{i.Berr}$	56.18
3.	Repeatability of Scale Factor (ppm)	$g_{i.SFrep}$	14.36
4.	Resolution (°/s)	$g_{iRe.}$	0.008
5.	Noise Floor (°/h/√Hz)	$g_{i.NF}$	13.72
6.	Temperature Sensitivity of Scale Factor (ppm/°C)	$g_{i.SFTS}$	1086.01
7.	Input Angular Rate Limit (°/s)	$g_{i.ARil}$	±500
8.	Linearity Error of Scale Factor (%)	$g_{i.SFlerr}$	0.5
9.	Asymmetry of Scale Factor (%)	$g_{i.SFsym}$	0.039
10.	Repeatability Bias (°/h)	$g_{i.Brep}$	65.59

(Source: Sarruda, 2011; Yan *et al*., 2012)

2.9.3 The MEMS Vibratory Gyroscope in Aircraft Autopilot Systems

Flight control systems in modern aircraft are fly-by-computer systems. Sensors are integral to the instrument systems on board aircraft, including flight, engine and navigation instruments. Signals from sensors monitoring the thrust levers, pedals and flight stick are received by a flight management system that controls engine power and actuates control surfaces such as ailerons and flaps. Sensors play a critical role in providing the data necessary for safe and effective aircraft operation by the pilot and automated control systems. Gyroscopes are used for heading indication as well as controlling common flight instruments like turn and attitude indicators. MEMS vibratory gyroscopes on the other hand detect changes in the capacitance or voltage of a piezoelectric material as it oscillates or vibrates. Attitude Heading and Reference Systems (AHRS) receive data from MEMS vibratory gyroscopes and display attitude information such as roll, pitch and yaw in addition to aircraft heading. This is as a result of the ADCs which output data to the autopilot system (Dalldorff *et al.,* 2013; Tomayko, 2017).

2.9.4 Faults of the MEMS Vibratory Gyroscope in Aircraft Autopilot Systems

A number of researches have centered generally on faults of gyroscopes in AASs. Notable of these researches are those concerned with analysis of faults due to bias, random drift, systematic drift, lag, gain degradation and floating of vertical gyroscopes (Jinhui and Jiang 2011); detection and isolation of sensor and surface/actuator failures affecting Kalman filter innovations in an UAV dynamic model (Caliskan and Hacizade 2017); detection and isolation of input sensor faults of a PIPER PA30 longitudinal aircraft characterised by a nonlinear model in the presence of wind gust disturbance and measurement errors (Singh and Murthy, 2015); sensor bias, jamming, disconnection and aileron and other control surface faults were detected and isolated by using knowledge of the aircraft's dynamics (Eykeren *et al.,* 2012); actuator failure detection and fault-tolerant control of a fixed-wing unmanned aerial aircraft using longitudinal and lateral PID control structures in combination with sequential least squares (Jimoh *et al.,* 2017). On the other hand, contributions of MEMS vibratory gyroscope faults to AAS failures involve the following: Faults due to angular rate resolution, inconsistent measurement repeatability, lack of accuracy, random bias instability and long term drift. These faults still limit deployment of the gyroscope in a variety of field applications where autonomous and repeatable operations are required over extended time and varying environments.

Bias: This is the apparent output of the rotation sensor for zero input rate assuming specific fixed operational conditions (e.g. temperature). It is expressed in deg/s or deg/hour units. A major source of bias error in MEMS vibratory gyroscopes is mechanical quadrature ie. the undesired sense-mode vibration caused by fabrication imperfections. While phase-sensitive demodulation suppresses the quadrature signal by several orders of magnitude, minute phase drifts called quadrature spill over error are inherent in the system. This is erroneous change of bias due to the partially unsuppressed quadrature. Random noise and drift effects are often referred to as bias.

Bias stability: This is a measure of the gyroscope's output stability over a length of time, and it is a fundamental performance metric for all gyroscope types including those of MEMS. Bias stability is measured after the device is turned on and for a particular length of time. This variable provides a measure of drift of the output offset value over time. Bias instability is best measured using the Allan Variance Measurement Technique (AVMT) (Passaro *et al*., 2017). Many applications, including autonomous vehicle navigation, require higher bias stability for excellent performance.

Angular rate resolution: Gyroscope resolution defines the minimum change in input required to produce a measurable change in output. The white noise of the device limits the resolution; therefore, the resolution can be determined by measuring the standard deviation of the white noise. White noise is a type of noise that is produced by combining sounds of all different frequencies together.

Bandwidth: The bandwidth of a gyroscope measures how many measurements can be made per second. It is the range of frequencies of the angular rate input that the gyroscope can detect. It indicates the range of input frequencies for which the input-output relation is preserved.

2.10 Review of Related Works on Mitigation of Faults of MEMS Vibratory Gyroscopes in Aircraft Autopilot Systems

MEMS vibratory gyroscopes are associated with a number of faults that affect their output performance. Table 2.2 presents a review of the related works of faults associated with MEMS vibratory gyroscope.

Table 2.2 Review of Related Works on Faults of MEMS Vibratory Gyroscopes

SN	Author	Title of Paper	Contribution	Limitation
1.	Shen *et al*. (2016).	A Noise Reduction Method for Dual-mass Micro-Electromechanical Gyroscopes based on Sample Entropy Empirical Mode Decomposition and Time-Frequency Peak Filtering.	Use of sample entropy empirical mode decomposition (SEEMD) was proposed to filter out various noise.	Temperature effects reduction was not considered.
2.	Jimoh *et al*. (2017).	PI-based Fault Tolerant Control for Fixed-wing UAVs using Control Allocation.	Use of PID control to overcome actuator failures for good stability and performance of UAVs.	Fuzzy-PID and ANFIS as better controllers were not considered for faults mitigation.
3.	Ma *et al*. (2020).	A Temperature Error Parallel Processing Model for MEMS Gyroscope based on a Novel Fusion Algorithm	Use of fusion algorithm to improve upon the mitigation of temperature drift effect on MEMS gyroscopes.	Noise effect was not considered.
4.	Xing *et al*. (2017).	Modelling and Compensating of Random Drift of MEMS Vibratory Gyroscope based on Least Squares Support Vector Machine Optimised by Chaotic Particle Swarm Optimisation.	Improvement of MEMS gyroscope precision by wavelet filtering of noise and random drift data reconstruction.	Temperature and noise effects on MEMS vibratory gyroscope were not considered.
5.	Liang *et al*. (2019).	A Method for Real-time Suppression of In-phase Error of Silicon Micro Gyroscopes.	Experimental suppression of real time in-phase error of micro gyroscope due to sensor noise.	Temperature effects suppression combined with that of the sensor noise based in-phase error was not studied.
6.	Rafiee *et al*. (2017).	A Review of the Most Important Failure, Reliability and Nonlinearity Aspects in the Development of Microelectromechanical System (MEMS)	Studied the nonlinear behaviour of silicon MEMS gyroscope.	Temperature and noise effects of MEMS gyroscope were not considered.

Table 2.2 Cont'd

7.	Patel and McCluskey (2016).	Performance of MEMS Vibratory Gyroscopes in Harsh Environments.	Clarified the effects of harsh environments such as temperature and humidity on MEMS vibratory gyroscope.	The effect of noise was not investigated.
8.	Tkalich *et al*. (2018).	Analysis of Errors in Micromechanical Devices.	Modelling of static errors to improve accuracy of micromechanical devices.	Dynamic errors were not considered.
9.	Jaiswal *et al*. (2016).	Adaptive Gyroscope Drift Compensation based on Temporal Noise Modelling.	Use of adaptive bias correction method to compensate random and static bias errors.	Temperature and noise were not considered.
10.	Gu *et al*. (2019).	MEMS Gyroscope Bias Drift Self-Calibration based on Noise-Suppressed Mode Reversal.	Proposed a bias drift self-calibration method for MEMS gyroscopes based on noise-suppressed mode reversal without mode-lling bias drift signal.	Temperature effect suppression were not considered.
11.	Ting *et al*. (2018).	Modelling of Structural and Environmental Effects on Microelectromechanical (MEMS) Vibratory Gyroscopes.	Investigated stiffness, damping and temperature effects on MEMS vibratory gyroscope performance.	Noise was not considered.
12.	Hu *et al*. (2018).	A Temperature Compe-nsation Method of Measuring Frequency for Cylindrical Vibra-tory Gyroscope in Freq-uency Split Trimming.	Development of a temperature compensation model.	Noise was not considered.
13.	Feng *et al*. (2018).	System Reliability Analysis of MEMS Gyroscope with Multiple Failure Modes.	Use of failure mechanism, process and mode correlation to determine MEMS gyroscope reliability.	Temperature and noise effects were not considered.
14.	Takala *et al*. (2012).	Bias Prediction for MEMS Gyroscopes.	Kalman filter prediction of MEMS vibratory gyroscope future bias.	The effect of temperature was not considered.
15.	Zhiqiang and Zheng (2011).	Disturbance Rejection in MEMS Gyroscope: Problems and Solutions.	Summarised practical applications of the Active Disturbance Rejection Control (ADRC) of MEMS vibratory gyroscopes.	Temperature and noise rejection control were not considered.

Recent developments on "faults" mitigation of MEMS vibratory gyroscopes are quite varied. Some of these measures however, could not consider temperature mitigation such as in the work on sample entropy empirical mode decomposition (Shen *et al*., 2016), bias drift self-calibration for noise suppression without the bias drift signal modelling (Gu *et al*., 2019) and Kalman filter prediction of noise (Takala *et al*., 2012). Similar research could not mitigate noise effects, notably, use of fusion algorithm to enhance temperature drift effect mitigation (Ma *et al*., 2020) in the performance of the gyroscope in harsh environments (Patel and McCluskey, 2016), investigation of stiffness, damping and temperature effects (Ting *et al*., 2018), temperature compensation model development of frequency measurement (Hu *et al*., 2018). Still in the literature, there are works that neither compensated temperature nor noise. Chiefly, in this category were works on compensation of random drift using Artificial Intelligence (AI) techniques (Xing *et al*., 2017), experimental suppression of in phase error (Liang *et al*., 2019), review of major reliability and nonlinearity challenges of MEMS structures (Rafiee *et al*., 2017), random and static bias errors compensation (Jaiswal *et al*., 2016), multiple failure mode based system reliability analysis (Feng *et al*., 2018) and practical applications of ADRC (Zhiqiang and Zhen, 2011).

An investigation of the combined effects of temperature and noise on the performance of the AAS will not only be relevant to the concept of safety in the aviation industry, but also, enhance the possibility of deploying the MEMS vibratory gyroscope as an angular rate sensor in AAS.
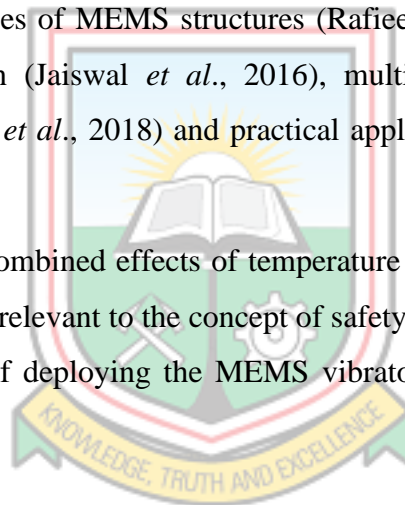
2.11   Summary and Research Gap

This chapter elaborated on the history of aviation, the types of aircraft, their principles of operation and also the forces acting on them. The AAS was also captured followed by the behaviour of the gyroscopes in the AAS. The DoF were explained and the 4-DoF of gyroscopes were elucidated. The chapter covered a review of related works on MEMS vibratory gyroscopes. After an extensive review, it became clear that no work had been done to mitigate the effects of faults of MEMS vibratory gyroscopes due to a combination of temperature and noise, on the AAS. In other words, possible MEMS vibratory gyroscope-related faults contributions as a result of temperature and noise to AAS failures have not been studied. This serves as enormous motivation for this research.

CHAPTER 3

MODELLING AND SIMULATION OF THE MEMS VIBRATORY GYROSCOPE

3.1   Introduction

The gyroscope is one of the most important components in aircraft instrumentation systems. In this research, the MEMS vibratory gyroscope is considered for deployment in the AAS. Mathematical modelling of the MEMS vibratory gyroscope is executed and simulations are conducted using MATLAB Simulink software. Flowchart of the modelling and simulation process of the MEMS vibratory gyroscope is shown in Fig. 3.1.
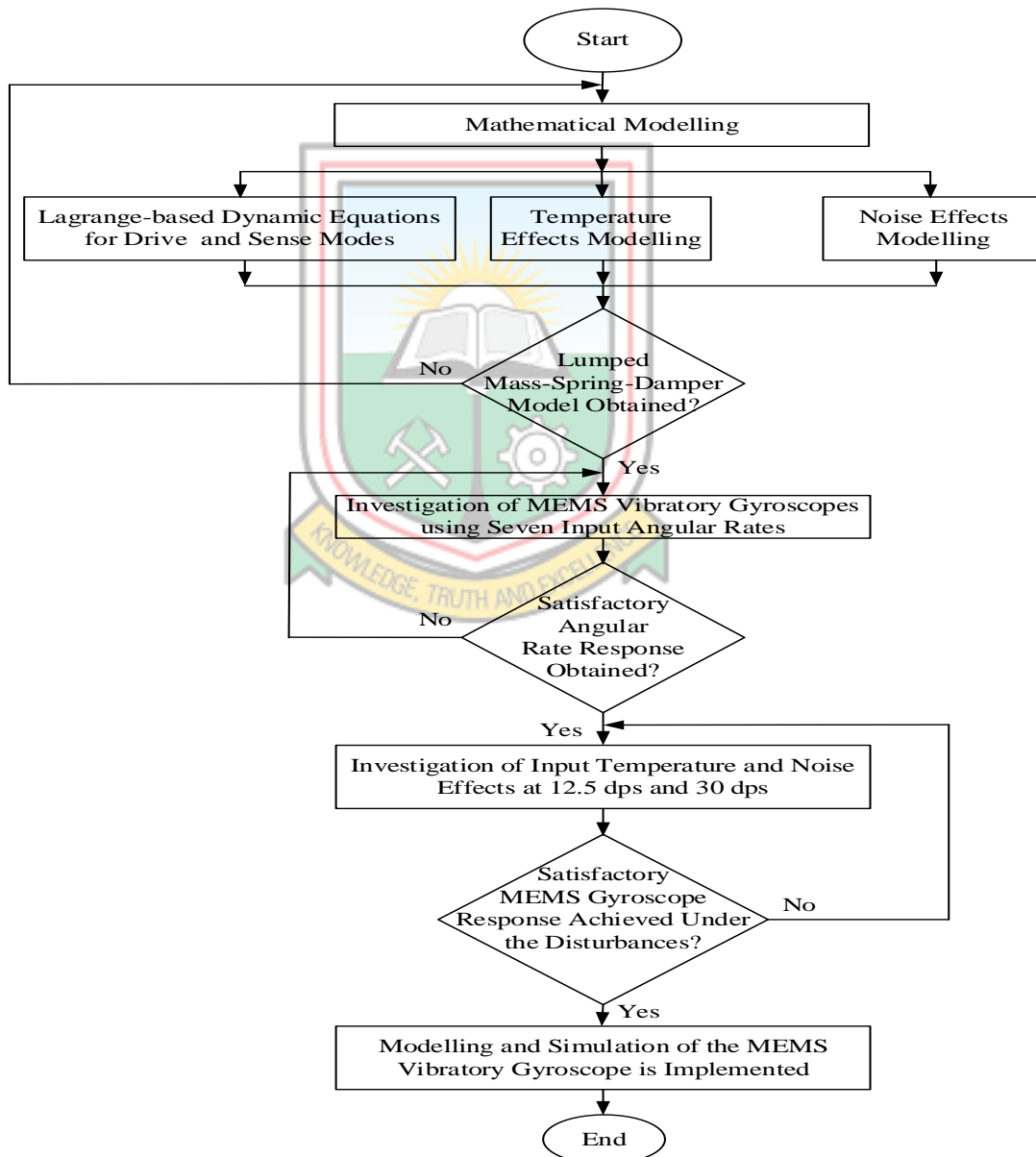
Fig. 3.1 A Flowchart of the Methodology for the Modelling and Simulation of MEMS Vibratory Gyroscope

3.2 Overview of MATLAB/Simulink Software

MATLAB is a programming language designed for solving complex technical problems in the science and engineering community. The advantage MATLAB has over other software is its ability to incorporate extensions with add-on toolboxes that are oriented towards a particular field of study. The graphical programming language Simulink is an extension of MATLAB, which is intended for dynamic system investigation. Presumably, the system under study is reorganised as functional diagrams, which consist of equivalent blocks by their functions, to the program blocks that are included in the Simulink library. The blocks in Simulink use click and drag to make a model of the actual system (Perelmuter, 2015).
.

3.3 Mathematical Modelling of the MEMS Vibratory Gyroscope

The operation of MEMS vibratory gyroscopes is based on the energy transfer of two perpendicular vibrational modes due to Coriolis effect. This working principle is based on the transfer of energy between the drive and sense modes as a result of Coriolis acceleration corresponding to input angular velocity. In the drive mode, the vibrating mass is oscillated at a constant amplitude and in the sense mode the orthogonal oscillation of sense mass due to input angular velocity is measured. The drive mode actuation and sense mode oscillation detection in MEMS vibratory gyroscopes is generally carried out using electrostatic transduction mechanisms due to their low-input power requirement. However, the output displacement of electrostatic actuators is low. Compared with conventional gyroscopes, the MEMS vibratory gyroscope demonstrates such advantages as lower cost, smaller size and lower power consumption which enable it to have broad application prospects in the military and civil fields such as Unmanned Aerial Vehicles (UAVs), and interactive consumer electronics including gaming consoles, mobile phones, and image stabilisation in cameras (Toyoda *et al*., 2015).

Inherent design drawbacks of a two single DoF MEMS vibratory gyroscope include narrow working mode bandwidth and poor dynamic stability and measurement accuracy due to inconsistent sensitivity (Minotti *et al*., 2017; Wang *et al*., 2014). It is assumed that the performance of the multi-DoF MEMS vibratory gyroscope is better than the two single DoF type that consist of 1-DoF drive mode and 1-DoF sense mode. This research seeks to focus on 3-DoF MEMS vibratory gyroscope.

There are two main models of the 3-DoF MEMS vibratory gyroscope namely, 2-DoF drive mode and 1-DoF sense mode and the 2-DoF sense mode and 1-DoF drive mode. With the

2-DoF sense mode and 1-DoF drive mode, the frame structure is used for quadrature error minimisation, but increases the mechanical impedance and achieves wide operational bandwidth. So, the sensitivity and bias stability of this model is not all that good in theory (Hao *et al*., 2019). Therefore, this research seeks to focus on the 2-DoF drive mode and 1-DoF sense mode. The 2-DoF drive mode and 1-DoF sense mode oscillates with a flat operation frequency region and utilises resonance in the 1-DoF sense mode which is placed in-between the two drive resonances. This design is aimed at operating the device in a robust mode and also achieving high sensitivity by utilising resonance of the sense mode. The disadvantage about this model is that when the system is operated at high frequency, the bandwidth becomes considerably high whereby amplitude decreases significantly (Abdolvand *et al*., 2016; Hu and Gallacher, 2018). Fig. 3.2 shows the schematic representation of the proposed gyroscope structure.
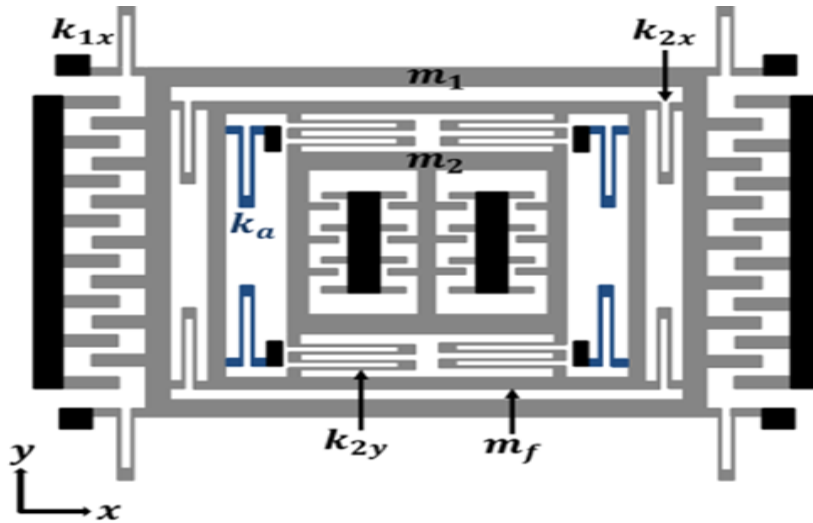
Fig. 3.2 Physical Layout Schematic of MEMS Vibratory Gyroscope

The structure consists of inertial masses and multiple suspensions configured in such a way to form the 3-DoF system with complete 2-DoF drive and 1-DoF sense oscillators. The outer mass m_1 is anchored to the substrate by spring k_{1x} while the sense mass m_2 is nested within the decoupled frame mass m_f which is connected to the drive mass m_1 by spring k_{2x}. The mass m_2 is also interconnected to m_f by the spring k_{2y}. The drive mass m_1 and the combination of masses m_2 and the decoupling frame m_f together form the 2-DoF drive mode oscillators in the x-direction. The spring k_{1x} connecting the drive mass m_1 to the outer anchors allows this drive mass to resonate in the x- direction alone, while constraining its motion in the y-direction, whereas the sense mass m_2, is configured to move in both

directions i.e. in the x-direction along with the frame mass, m_f and in the y-direction allowed by spring k_{2y}. Besides, m_2 is also anchored to the substrate by additional spring k_a in the drive direction as shown in Fig. 3.2. The additional spring is designed to reduce the resonance separations of the two drive mode oscillators, thereby increasing the drive amplitude.

Dynamic equations for drive and sense modes

The equations of motion for the proposed MEMS vibratory gyroscope are derived using the Lagrange equation, given as in Equation (3.1).

$$\frac{d}{dt}\left(\frac{\partial K}{\partial \dot{x}_i}\right) - \frac{\partial K}{\partial x_i} + \frac{\partial D}{\partial \dot{x}_i} + \frac{\partial V}{\partial x_i} = f \tag{3.1}$$

where, K = kinetic energy

   V = potential energy

   D = dissipation function

   f = the forcing function of the vibrating system

The subscript i depicts the degree of freedom.

Fig. 3.3 and Fig. 3.4 show the lumped parameter mass-spring-damper representation and lumped model, respectively of the proposed MEMS vibratory gyroscope.
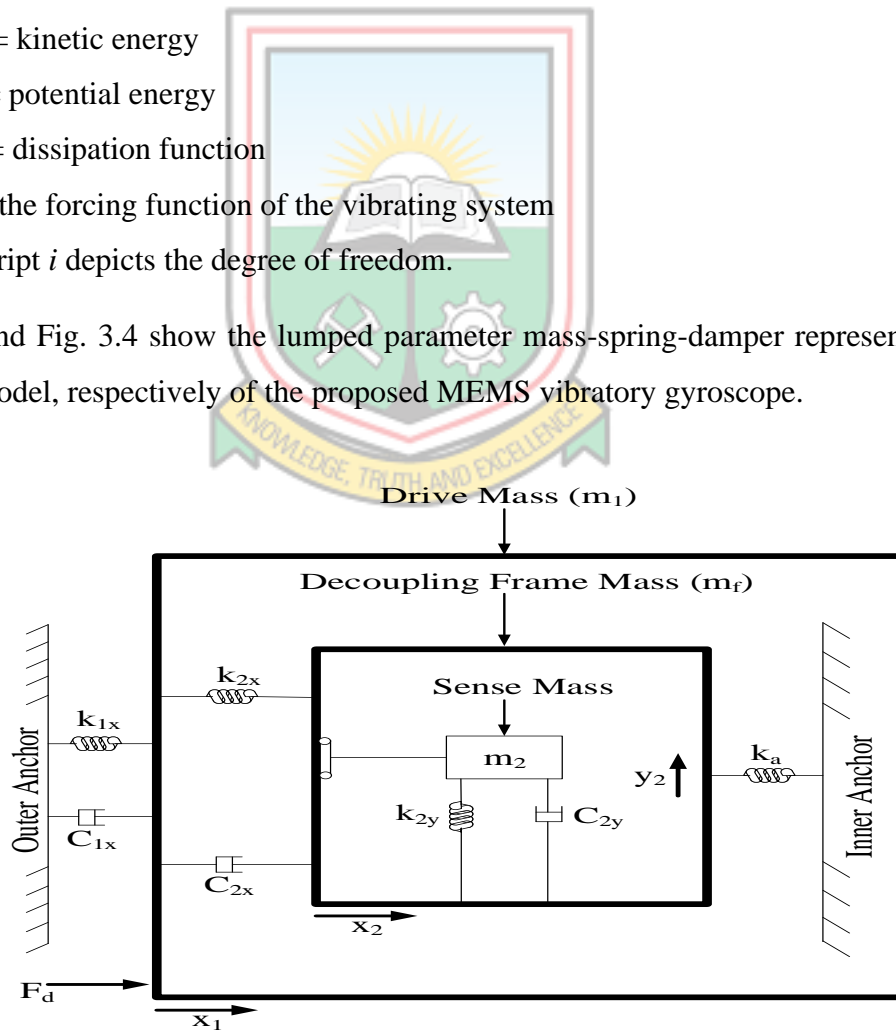
Fig. 3.3 Mass-Spring-Damper Representation of the 3-DoF MEMS Vibratory Gyroscope
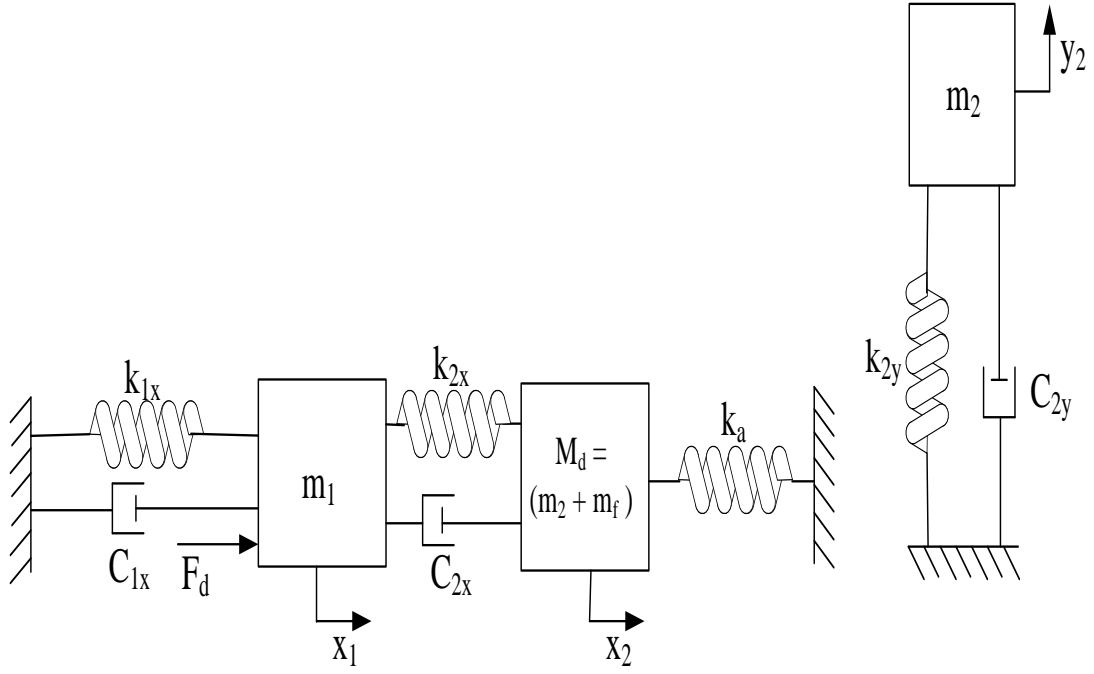
Fig. 3.4 Lumped Mass-Spring-Damper Model of the Proposed MEMS Vibratory Gyroscope

The kinetic energy, potential energy, and dissipative function for this model can be written as:

$$K = \frac{1}{2} m_1 \dot{x}_1^2 + \frac{1}{2}(m_2 + m_f)\dot{x}_2^2 + \frac{1}{2} m_2 \dot{y}_2^2 \tag{3.2}$$

$$V = \frac{1}{2} k_{1x} x_1^2 + \frac{1}{2} k_{2x}(x_1 - x_2)^2 + \frac{1}{2} k_a x_2^2 + \frac{1}{2} k_{2y} y_2^2 \tag{3.3}$$

$$D = \frac{1}{2} c_{1x} \dot{x}_1^2 + \frac{1}{2} c_{2x} \dot{x}_2^2 + \frac{1}{2} c_{2y} \dot{y}_2^2 \tag{3.4}$$

$$m_1 \ddot{x}_1 + c_{1x} \dot{x}_1 + (k_{1x} + k_{2x})x_1 - k_{2x} x_2 = F_d(t) \tag{3.5}$$

$$M_d \ddot{x}_2 + c_{2x} \dot{x}_2 + (k_{2x} + k_a)x_2 - k_{2x} x_1 = 0 \tag{3.6}$$

$$m_2 \ddot{y}_2 + c_{2y} \dot{y}_2 + k_{2y} y_2 = 0 \tag{3.7}$$

where, $F_d(t) = F\cos(\Omega t)$ = driving force that excites the active mass m_1 at the drive

frequency ω_d, and results in the displacement x_1,

$M_d = (m_2 + m_f)$ = drive direction displacement of the proof mass m_2 together

with inner frame mass m_f,

$2m_2\Omega_z\dot{x}_2$ = displacement of the sense mass m_2 due to Coriolis force

where, Ω_z = time invariant input angular rate about the z-axis

c_{1x}, c_{2x} and c_{2y} = damping coefficients in both the drive and sense directions

k_{1x}, k_{2x} and k_{2y} = spring stiffness in both drive and sense directions

For frequency analysis, the Equations (3.5), (3.6) and (3.7) can be transformed into a matrix form given as:

$$[M]\ddot{X} + [C]\dot{X} + [K]X = [F_D] \tag{3.8}$$

where matrices M, C and K are given as:

$$[X] = \begin{bmatrix} x_1 \\ x_2 \\ y_2 \end{bmatrix} \tag{3.9}$$

$$[M] = \begin{bmatrix} m_1 & 0 & 0 \\ 0 & m_2 + m_f & 0 \\ 0 & 0 & m_2 \end{bmatrix} \tag{3.10}$$

$$[C] = \begin{bmatrix} c_{1x} & 0 & 0 \\ 0 & c_{2x} & 0 \\ 0 & 0 & c_{2y} \end{bmatrix} \tag{3.11}$$

$$[K] = \begin{bmatrix} k_{1x} + k_{2x} & -k_{2x} & 0 \\ -k_{2x} & k_{2x} + k_a & 0 \\ 0 & 0 & k_{2y} \end{bmatrix} \tag{3.12}$$

$$F_D = \begin{bmatrix} F_d \\ 0 \\ 0 \end{bmatrix} \tag{3.13}$$

If the system of equations has a solution then,

$$[X] = [A]\sin(\omega t) + [B]\cos(\omega t) \tag{3.14}$$

where, A and B are vectors,

$$[K] - \omega^2[M] = \begin{bmatrix} k_{1x} + k_{2x} - \omega^2 m_1 & -k_{2x} & 0 \\ -k_{2x} & k_{2x} + k_a - \omega^2(m_2 + m_f) & 0 \\ 0 & 0 & k_{2y} - \omega^2 m_2 \end{bmatrix} \tag{3.15}$$

$$\omega[C] = \begin{bmatrix} \omega c_{1x} & 0 & 0 \\ 0 & \omega c_{2x} & 0 \\ 0 & 0 & \omega c_{2y} \end{bmatrix} \tag{3.16}$$

$$[T] = \begin{bmatrix} [K] - \omega^2[M] & -\omega[C] \\ \omega[C] & [K] - \omega^2[M] \end{bmatrix} \tag{3.17}$$

The relation among A, B and T is given by:

$$\begin{bmatrix} [A] \\ [B] \end{bmatrix} = [T]^{-1} \begin{bmatrix} [F] \\ [0] \end{bmatrix} \tag{3.18}$$

Once A and B are known, the frequency response can be obtained as in equation (3.19).

$$x_i(\omega) = \sqrt{A_i + B_i} \tag{3.19}$$

If the length of a beam L as the x-axis dimension, width was the y-axis dimension and the thickness t as the z-axis dimension are known, then the area moment of inertia of the beam in the y and z directions are given by Equations (3.20) and (3.21) (Acar and Shkel, 2009; Kavitha *et al.*, 2016).

$$I_y = \frac{1}{12}tw^3 \tag{3.20}$$

$$I_z = \frac{1}{12}tw^3 \tag{3.21}$$

where, I_y = moment of inertia in the y direction

t = thickness of the beam

w = width of the beam

I_z = moment of inertia in the z direction

For a single fixed guided beam, the translational stiffness for motion in the orthogonal direction to the beam axis is given as in Equation (3.22) (Zhou *et al.*, 2017).

$$K_{y,z} = \frac{1}{2}\frac{3EI_{y,z}}{(\frac{L}{2})^3} \tag{3.22}$$

where, E = the Young's modulus

$I_{y,z}$ = moment of inertia in the orthogonal direction

L = length of the beam

The stiffness values of the fixed-guided beam along the three principal axes are given by Equations (3.23), (3.24) and (3.25) (Liu and Yan, 2017).

$$k_x = E\frac{wt}{L} \tag{3.23}$$

$$k_y = E\frac{w^3t}{L^3} \tag{3.24}$$

$$k_z = E\frac{wt^3}{L^3} \tag{3.25}$$

where, k_x = stiffness of the fixed-guided beam in the x direction

k_y = stiffness of the fixed-guided beam in the y direction

k_z = stiffness of the fixed-guided beam in the z direction

For a folded beam, stiffness becomes (Zhou *et al*., 2016):
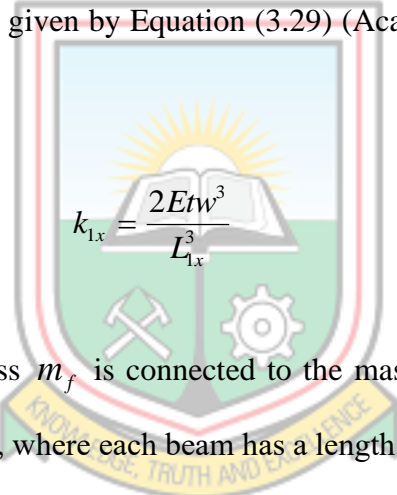
$$k_{folded} = E \frac{tw^3}{2L^3} \tag{3.26}$$

The stiffness of a double-folded beam is expressed by Equation (3.27) (Nashat *et al*., 2018)

$$2k_{folded} = (E \frac{tw^3}{2L^3}) \times 2 \tag{3.27}$$

$$k_{folded} = E \frac{tw^3}{L^3} \tag{3.28}$$

The suspension connecting the drive mass m_1 to the anchors is consisted of single U-turn four flexures with length L_{1x} of each beam as shown in Fig. 3.2. The overall stiffness of the suspension for mass m_1 is given by Equation (3.29) (Acar and Shkel, 2009; Verma *et al*., 2015):

$$k_{1x} = \frac{2Etw^3}{L_{1x}^3} \tag{3.29}$$

The decoupling frame mass m_f is connected to the mass m_1 by suspension comprising single U-turn four flexures, where each beam has a length of L_{2x}. The derived stiffness for the suspension is given by equation (3.30) (Verma *et al*., 2015).

$$k_{2x} = \frac{2Etw^3}{L_{2x}^3} \tag{3.30}$$

The suspension anchoring the frame mass, m_f, to the substrate is provided with single U-turn four flexures, the length of each arm of which is L_a. These springs are oriented with their axes perpendicular to the drive direction. They are designed to reduce the resonance separation between the two drive modes, thereby increasing the drive mode amplitude. These beams are also modelled similarly and the overall stiffness is derived as given by Equation (3.31) (Verma *et al*., 2015).

$$k_a = \frac{2Etw^3}{L_a^3} \tag{3.31}$$

The suspension connecting the passive mass, m_2 to the frame mass m_f is comprised of double U-turn four flexures in order to achieve increased sensitivity in the sense direction. These flexures are rigid in the drive direction hence, eliminating dynamical coupling between the drive and sense modes. The length of each beam is L_{2y} and the derived stiffness value is (Verma *et al.*, 2015):

$$k_{2y} = \frac{2Etw^3}{L_{2y}^3} \tag{3.32}$$

The overall suspension design offers dynamical amplification of the passive mass, decoupling of the drive and sense direction oscillators and elimination of cross coupling between the drive and sense modes. It may be noted that the width of all flexures has been assumed to be the same, i.e., *w* and the entire structure of the device is uniformly thick having thickness of *t*.

3.3.1 Temperature Effects

The main material of MEMS gyroscope is silicon, which is sensitive to temperature variations. The mechanical and physical parameters such as Young's modulus and stress are influenced by temperature, and will affect the stiffness of system and gyro resonance frequency, cause drift of the output temperature of gyroscope. Its properties include structure, size, modulus of elasticity and residual stress, etc. change with temperature. The change of its modulus of elasticity is particularly significant as it causes the change of system stiffness, resulting in the change of resonance frequency. Modulus of elasticity has an approximate linear relationship with temperature change and this is represented in the following equations (Jiang *et al.*, 2018; Tang *et al.*, 2013).

$$E(T) = E(T_o)k_E E(T_o)(T - T_o) \tag{3.32}$$

where, $E(T)$ and $E(T_o)$ = modulus of elasticity of silicon at the temperature of T and T_o

= 300 K

k_E = temperature coefficient of modulus of elasticity of silicon

Since the MEMS gyroscope system stiffness is proportional to the modulus of elasticity, thus we have:

$$K = K_o - k_E K_o (T - T_o)$$ (3.33)

The relationship between resonant frequency and temperature can then be expressed as:

$$\omega_n(T_2) = \sqrt{\frac{K_2}{m}} = \sqrt{\frac{[K_1 - k_E K_1(T_2 - T_1)]}{m}}$$ (3.34)

where, K_2 and K_1 = system stiffness at the temperatures T_2 and T_1

$\omega_n(T_2)$ = gyroscope's resonant frequency at the temperature of T_2

m = weight of the mass block

As T_1 is close to T_2, equation (3.34) can be approximated as:

$$\omega_n(T_2) \approx \frac{\omega_n(T_1)[1 - k_E(T_2 - T_1)]}{2}$$ (3.35)

Clearly, the gyroscope's resonant frequency is dependent on temperature and temperature gradient. Gyroscope compensation mainly deals with scale factor error and zero bias error. If the gyroscope is static, the offset of gyroscope detection sensitivity is mainly zero drift. And the reason for gyroscope zero bias is the offset of its natural frequency and Q-value. When compensating for static error (mainly zero bias error), the commonly used model is based on the built-in temperature sensor, without considering the temperature gradient and the relationship between temperature of environment and internal temperature (Fontanella *et al.*, 2018).

3.3.2 Noise Effects

Noise is an irregular or unwanted signal. In AASs, noise is one of the unwanted signals that affect the output of the autopilot system. A Gauss-Markov (GM) method of noise reduction is applied. The GM processes are stationary processes that have exponential Auto Correlation Function (ACF). The first-order GM process is frequently used to describe a correlated signal, which is defined by the exponential ACF (Navidi *et al.*, 2016).

$$R_x(\tau) = \sigma^2 e^{-\beta|\tau|} \tag{3.36}$$

where, $R_x(\tau)$ = correlated signal

$\quad \sigma^2$ = noise variance

$\quad \beta^{-1}$ = correlation time

$\quad \tau$ = time interval

Equations (3.37) and (3.38) give the second and third order GM process models,

$$x_k = e^{-\beta \Delta t} x_{k-1} + w_k \tag{3.37}$$

$$\sigma_{x_k}^2 = \frac{\sigma_{w_k}^2}{(1 - e^{-2\beta \Delta t_k})} \tag{3.38}$$

where, Δt = discrete time sampling interval

$\quad w_k$ = zero mean Gaussian white noise

$\quad x$ = random variable

3.4 Simulation of the MEMS Vibratory Gyroscope using MATLAB/Simulink Software

Fig. 3.5 shows the MEMS vibratory gyroscope represented in Matlab Simulink software version 2019a. The MEMS vibratory gyroscope is hereby separately simulated for a better understanding of its performance, especially under fault conditions of temperature and noise. In the simulations, the angular rates in degrees per second (dps) considered as sensor input are -0.15, 12.5, 20, 25, 33 and 35. The acknowledgement of the input angular rates of the MEMS vibratory gyroscope are duly presented in the results and discussion.
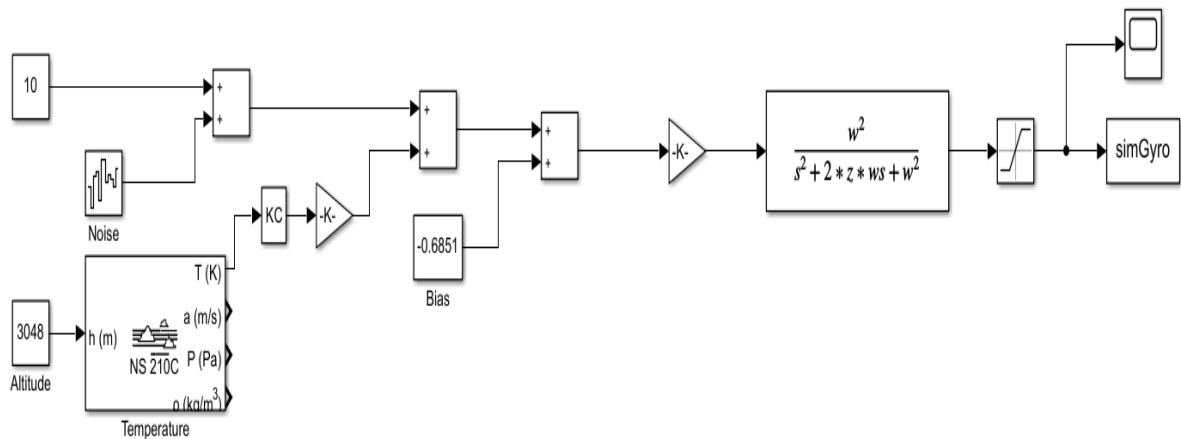
Fig. 3.5 MATLAB/Simulink Version of MEMS Vibratory Gyroscope

3.5   Results and Discussion

3.5.1   Simulation Results

The simulation results are presented on Figs. 3.6 to Fig. 3.13. Fig. 3.6 and Fig. 3.7 give the response of the MEMS vibratory gyroscope without the influence of temperature and noise faults. Fig. 3.8 and Fig. 3.9 give the outcome of temperature influence on the performance of gyroscope. The noise effect is given by Fig. 3.10 and Fig. 3.11. Finally, the effects of both noise and temperature are provided by Fig 3.12 and Fig. 3.13.
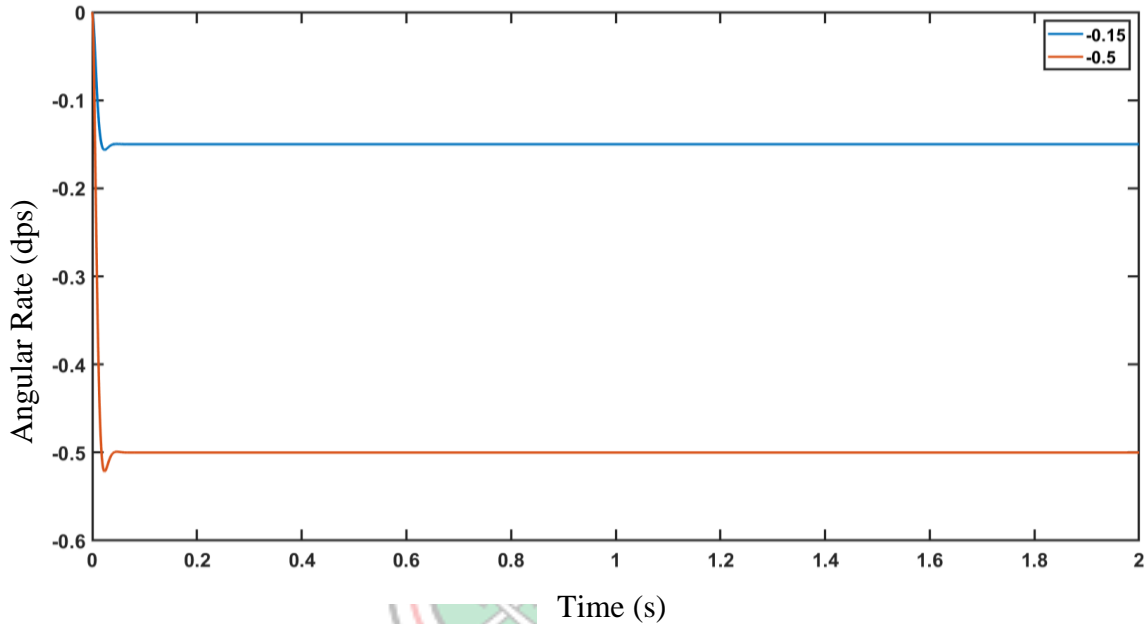
Fig. 3.6 Response of MEMS Vibratory Gyroscope to Input Angular Rates of -0.5 dps and – 0.15 dps
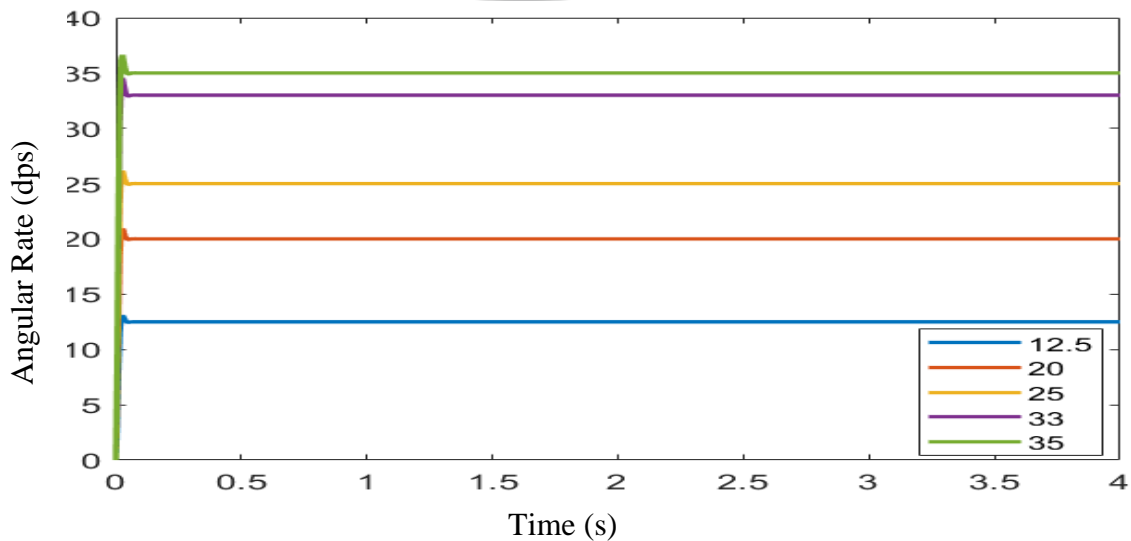
Fig. 3.7 Response of MEMS Vibratory Gyroscope to the Input Angular Rates of 12.5, 20, 25, 33 and 35 dps
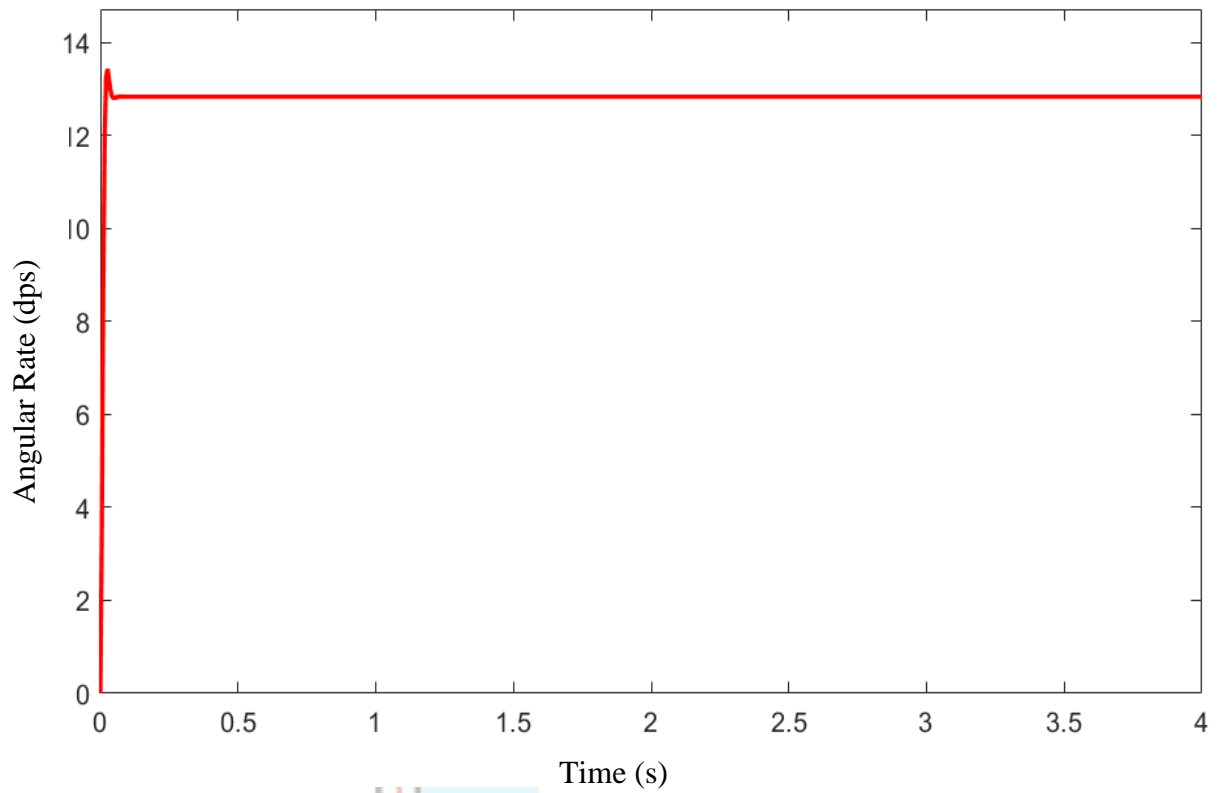
Fig. 3.8 Response of MEMS Vibratory Gyroscope to the Input Angular Rate of 12.5 dps with the Introduction of Temperature at a Height of 3084 m
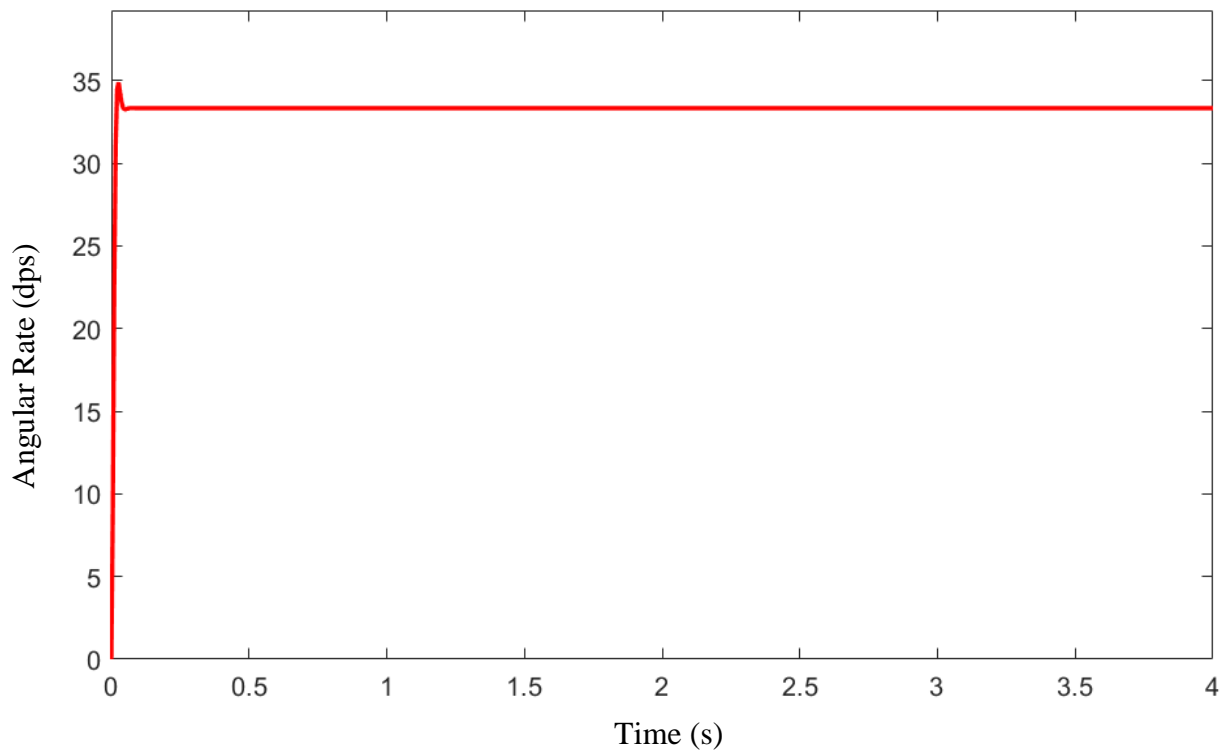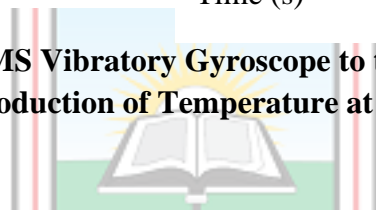
Fig. 3.9 Response of MEMS Vibratory Gyroscope to the Input Angular Rate of 33 dps with the Introduction of Temperature at a Height of 3084 m
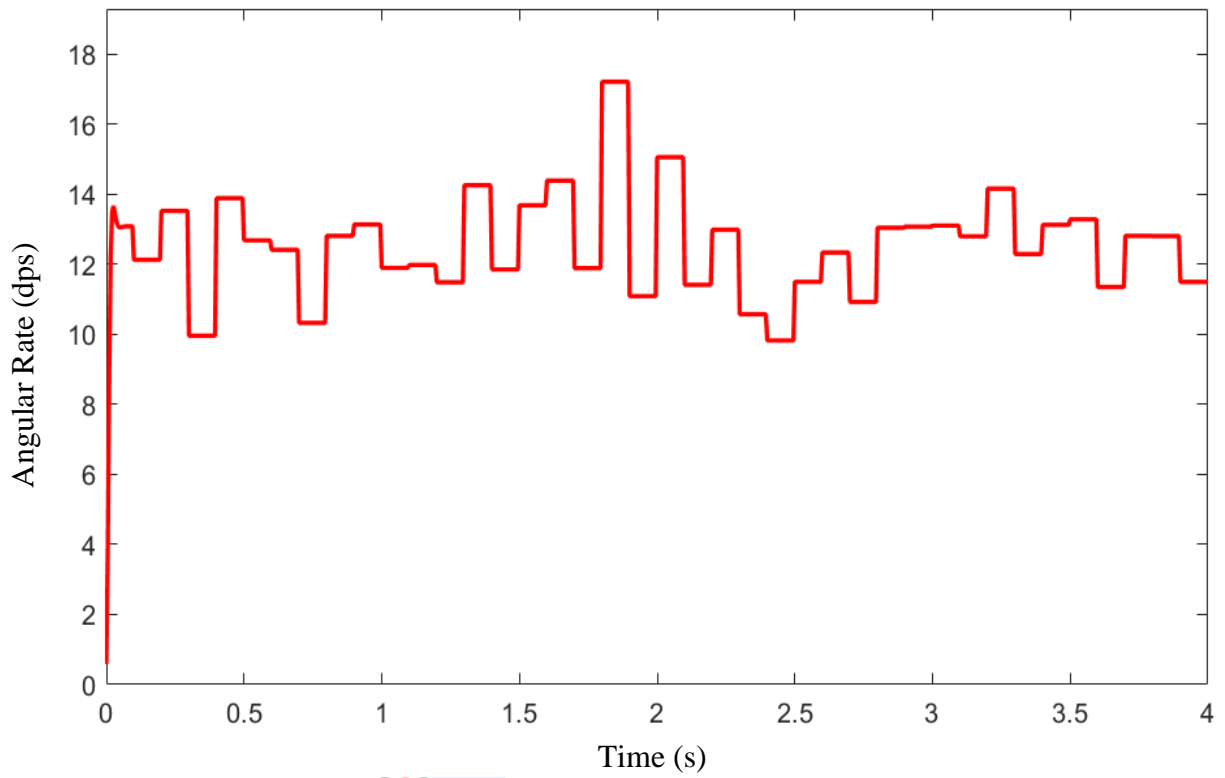
Fig. 3.10 Response of MEMS Vibratory Gyroscope to the Input Angular Rate of 12.5 dps with Noise Introduced
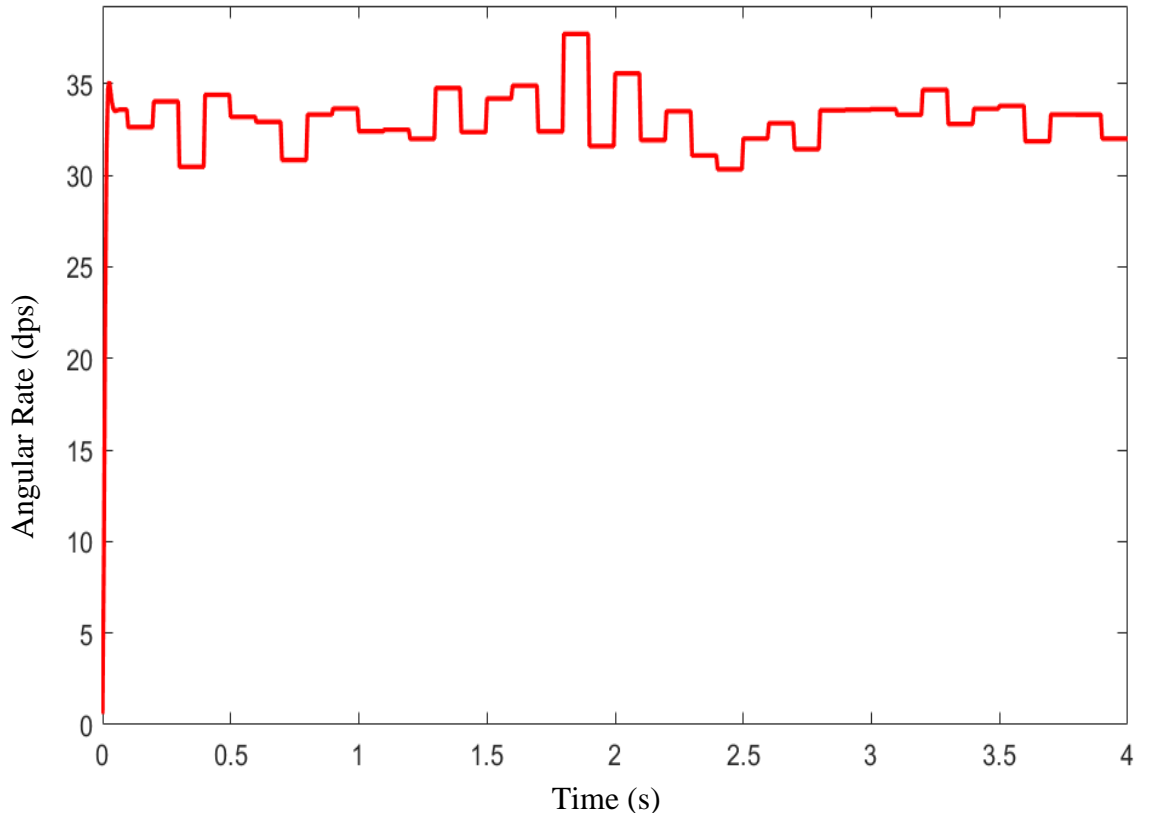
Fig. 3.11 Response of MEMS Vibratory Gyroscope to the Input Angular Rate of 33 dps with Noise Introduced
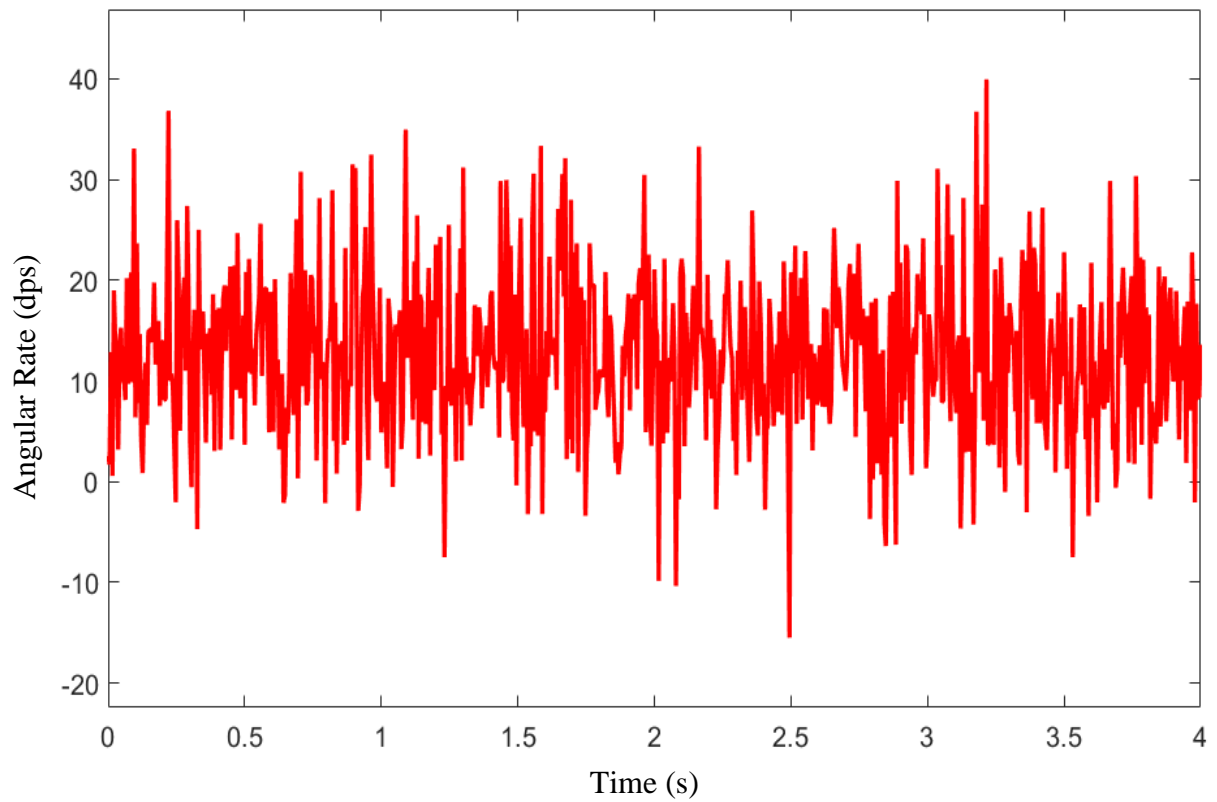
Fig. 3.12 Response of MEMS Vibratory Gyroscope to the Input Angular Rate of 12.5 dps with the Introduction of Temperature and Noise
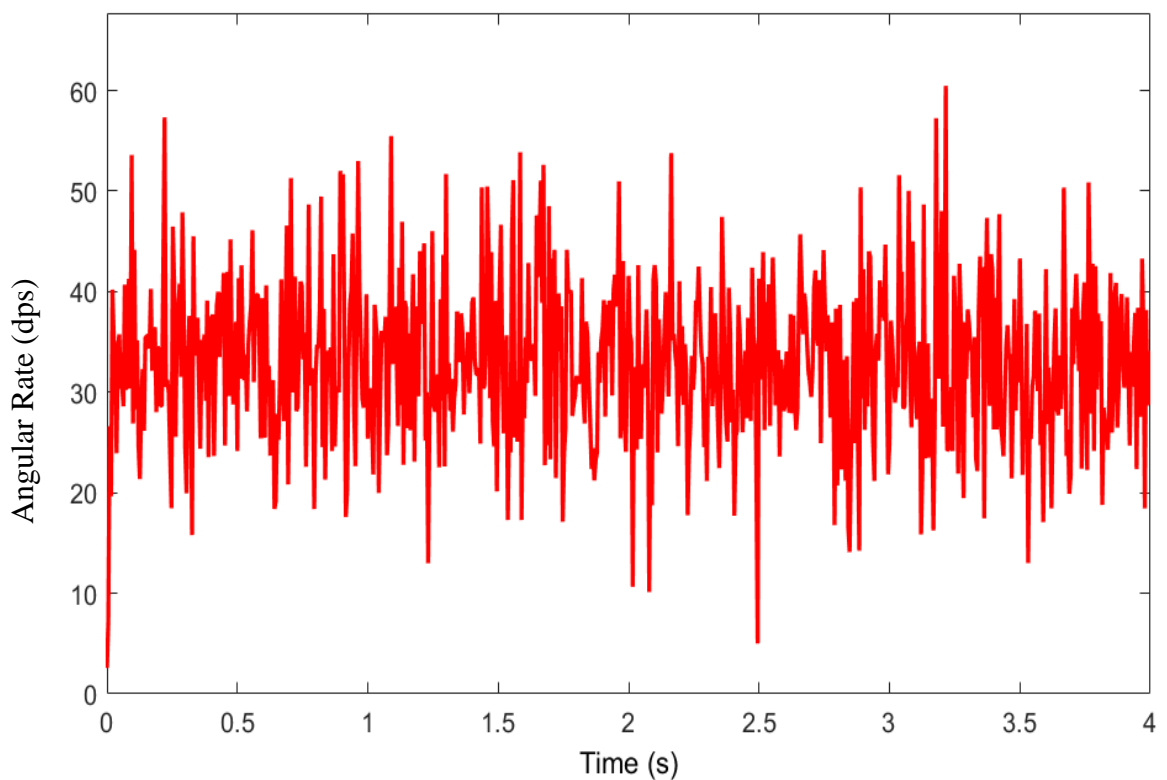
Fig. 3.13 Response of MEMS Vibratory Gyroscope to the Input Angular Rate of 33 dps with the Introduction of Temperature and Noise

3.5.2   Discussion

From Fig. 3.6 and Fig. 3.7, it could be seen that the respective input angular rates are duly reported by the MEMS vibratory gyroscope though with an overshoot of 4.53% to 5.85% and no oscillations whatsoever. From Fig. 3.8 and Fig. 3.9, the introduction of temperature as a fault increased the response of the gyroscope by 0.05%. The effect of noise as seen from Fig. 3.10 and Fig. 3.11 are quite pronounced on the response of the gyroscope. It distorts the output signal and can capably influence the ability of the control system to accurately control the attitude of aircraft with regard to the pitch. The discrepancy in the angular rate signal is of the order of $\pm 5\%$. Standard practice stipulates a value of 2%. The combined effect of temperature and noise is severe, as can be seen from Fig. 3.12 and Fig. 3.13. It can be seen that signal waveform distortion lies in the range of $\pm 10\%$. This can have detrimental effect on the aircraft's pitch control system and this calls for further investigation.

3.6   Summary

In this chapter, the MEMS vibratory gyroscope had been investigated by way of modelling and simulations. The correctness of the mathematical model of the gyroscope was validated by way of responses to angular rates at its input. It came to light however, that the combined effects of temperature and noise as faults are capable of degrading the accuracy and stability of the pitch measurement and control. Further investigation is required to establish the exact effect of these variables on the pitch control system and this serves as the focus of Chapter 4.
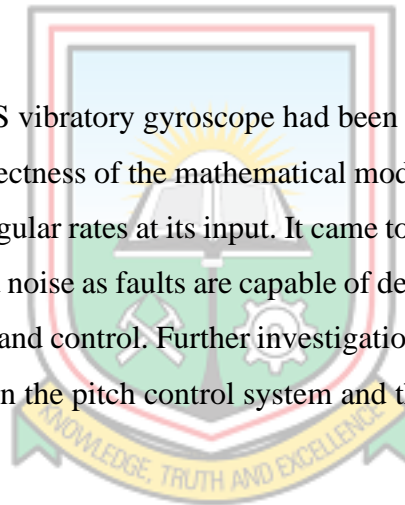
CHAPTER 4

PITCH CONTROL BY THE AIRCRAFT AUTOPILOT SYSTEM

4.1   Introduction

This chapter investigates the effects of temperature and noise being experienced by the MEMS vibratory gyroscope, on the pitch control system of the AAS. Aircraft pitch control movement is critical during the take-off phase, steady flight as well as landing. The system is evaluated using mathematical models and simulations in MATLAB Simulink software. Fig. 4.1 gives a flowchart of the methodology of pitch control.
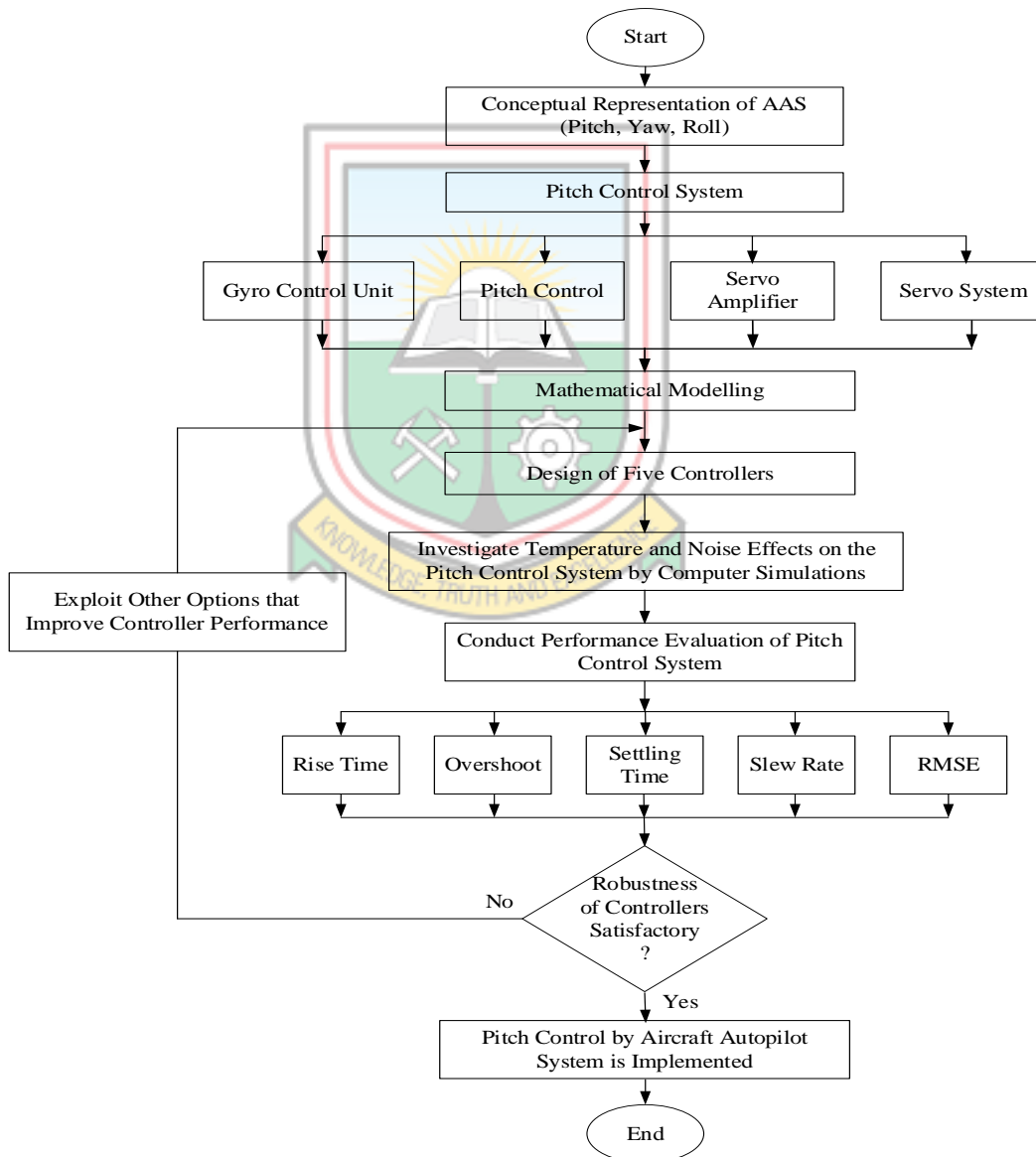
Fig. 4.1 A Flowchart of the Methodology for Pitch Control by Aircraft Autopilot System

4.2   Concept of the Aircraft Autopilot System

There are three basic control motions of aircraft, i.e. pitch, roll and yaw. The pitch motion of aircraft is categorised under longitudinal stability whereas roll and yaw are categorised under lateral stability. In this research, emphasis is put on the pitch motion of the aircraft under the control of the autopilot system. The concept of the complete AAS is illustrated in Figure 4.2.
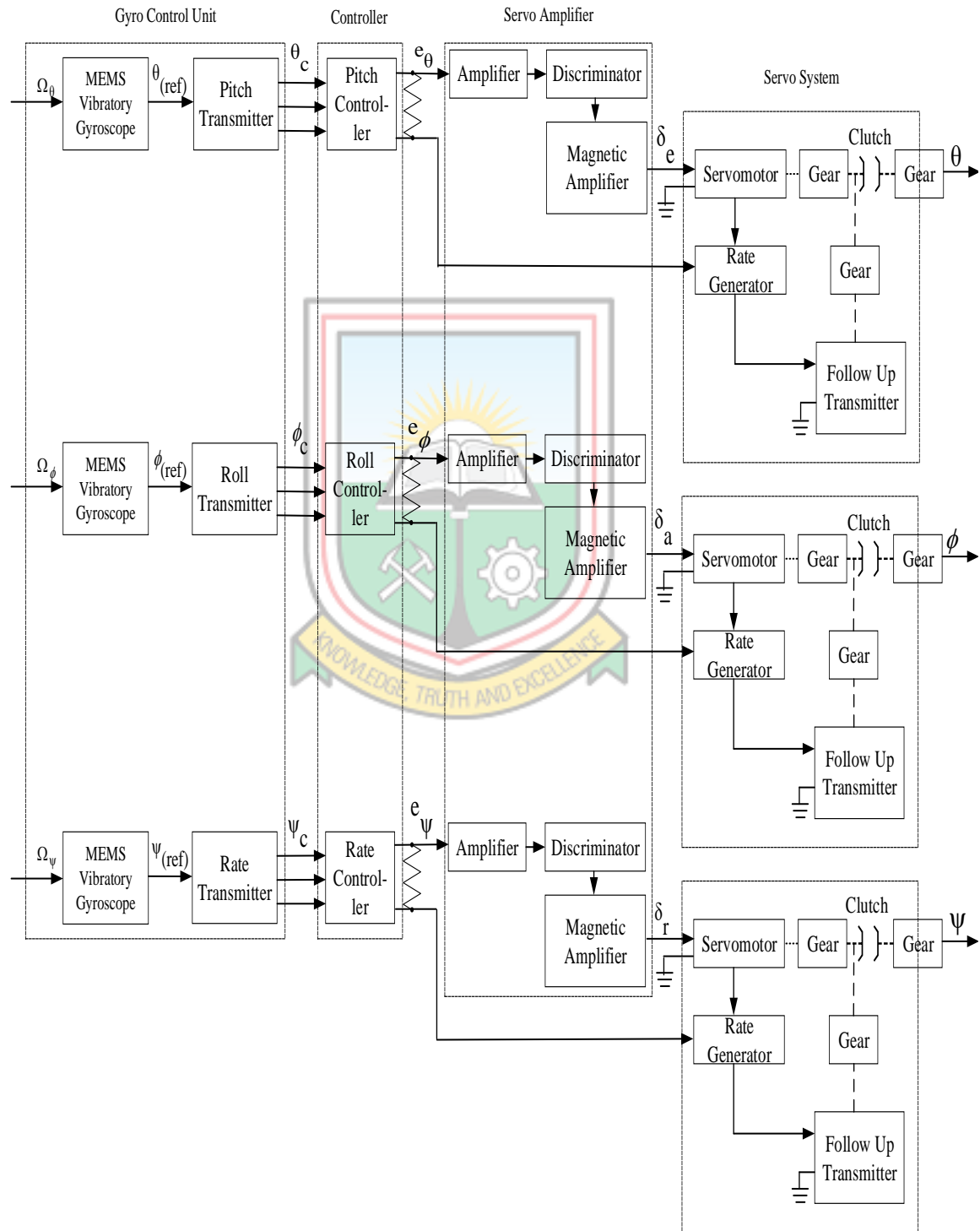
Fig. 4.2 Conceptual Representation of the Aircraft Autopilot System

4.3 The Pitch Control System

Aircraft pitch control motion offers a critical phase during take-off as well as during steady flight and landing. A set of control surfaces known as elevator are used for controlling aircraft pitch motion. Elevators are movable control surfaces located at the back of fixed wing aircraft and hinged to the trailing edge of the horizontal stabliser, running parallel to the main wings that cause rotation of the aircraft. The elevators cause the aircraft to climb and descend and also to obtain sufficient lift from the wings to keep the aircraft in level flight at various speeds (Mcruer *et al.*, 2014). If the elevator is rotated upwards, it decreases the lift force on the tail, causing the tail to lower and the nose to rise. If the elevator is rotated downward, it increases the lift force on the tail causing it to rise and the nose to lower. Lowering the aircraft's nose increases speed in forward direction and raising the nose decreases the same speed. The pitch control system of aircraft consists of the gyro control unit, pitch controller, servo amplifier and the servo system. Fig. 4.3 shows the functional diagram of the pitch control system.
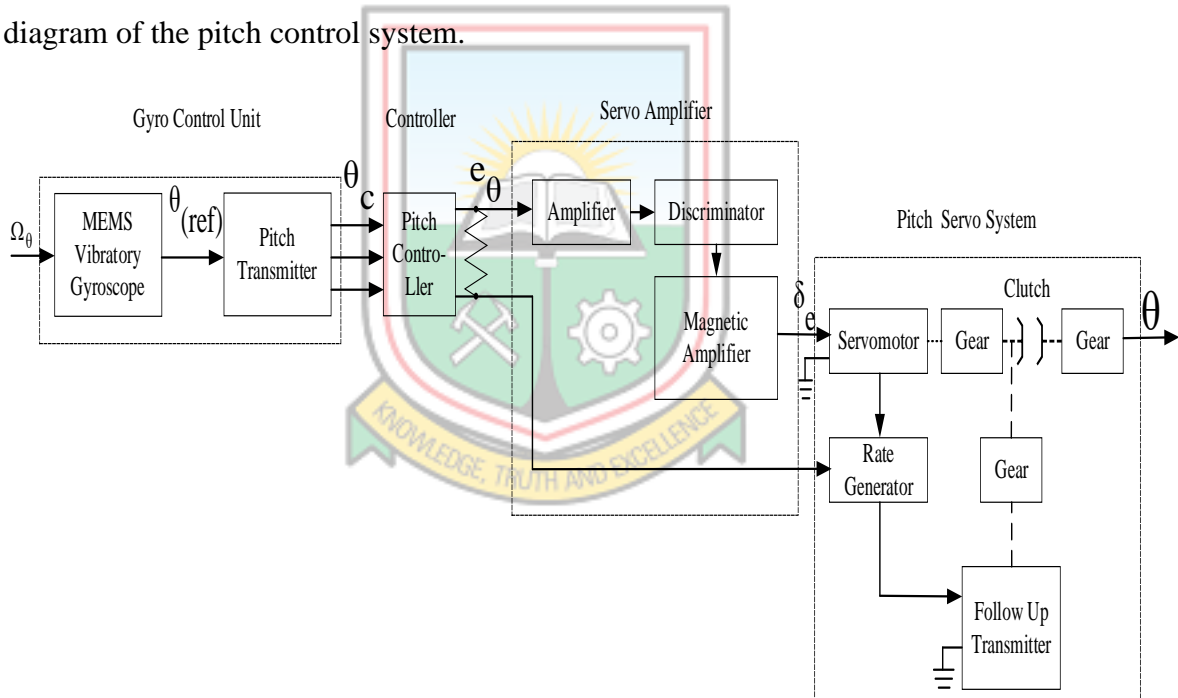
Fig. 4.3 Functional Diagram of the Pitch Control System

4.3.1   Gyro Control Unit

MEMS vibratory gyroscope

A gyroscope is a device used for measuring or maintaining orientation and angular velocity. MEMS gyroscopes are fabricated using micromachining techniques and do not rely on a spinning rotor as used in conventional mechanical gyroscopes because fabricating rotating parts with significant useful mass is difficult at the micro level. The gyroscope is used for

measuring or maintaining the pitch control of aircraft. Hitherto existing pitch control systems make use of mechanical gyroscopes and not the MEMS gyroscopes. This research tries to deploy the MEMS vibratory gyroscope in pitch control by the AAS. This is because MEMS vibratory gyroscopes are very small in size, devoid of spinning discs and cost efficient compared to mechanical gyroscopes. The MEMS vibratory gyroscope is to control the orientation of the aircraft.

MEMS gyroscopes are vibratory rate gyroscopes, which have no rotating parts that require bearings, and can be easily miniaturised and batch fabricated using micromachining techniques. These structures are fabricated on polysilicon or crystal silicon, and their main mechanical component is a two degree of freedom vibrating proof mass, which is capable of oscillating on two directions in a plane. Their operation is based on the Coriolis effect. When the gyroscope is subjected to an angular velocity along an axis (input axis) orthogonal to the axis of initial oscillation (driven axis), the Coriolis effect transfers energy from one vibrating mode to another. The response of the second vibrating mode, which is along a third axis (sense axis) orthogonal to the previous two, provides information about the applied angular velocity. The vibrating modes of a MEMS vibratory gyroscope are mechanically uncoupled, their natural frequencies should be matched, and their outputs should only be sensitive to angular velocity (Krug, 2016).

Pitch transmitter and follow-up transmitter

Pitch transmitter forms part of the gyro control unit. It is located between the MEMS vibratory gyroscope and the pitch controller. Its purpose is to transmit angular orientation signals from the output of the MEMS vibratory gyroscope to the pitch controller. This signal is then amplified by the servo amplifier to drive the servo system, which in turn applies the pitch signal to the AAS system to actuate the elevator in order to control the pitch angle of the aircraft. The follow up transmitter transduces the actual pitch angle and in combination with the pitch transmitter, generates a voltage signal proportional to the angular error which actuates the pitch servo.

4.3.2 Pitch Controller

The pitch controller of the AAS implements an algorithm that helps to control the angular orientation of aircraft such that it hardly varies from the reference value. The controller functions by generating angular error signals that serve as the control signal to bring the actual pitch angle to the set point or reference value. In this research, the pitch controller is

deployed to help suppress unwanted temperature and noise signals existing at the input of the gyroscope from influencing the angular orientation of the aircraft.

4.3.3 Servo Amplifier

The servo amplifier of the pitch control system comprises the amplifier, discriminator and magnetic amplifier which together serve the purpose of amplification of the low energy output signal of the pitch controller to a high energy signal capable of actuating the servomotor of the servo system. The amplifier element pre-amplifies the pitch controller output signal whilst the magnetic amplifier serves the purpose of a power amplifier. The discriminator matches signals of the magnetic amplifier to that of the pre-amplifier by way of discriminating the signal at its input in terms of magnitude and phase with the help of reference signals in order to generate a corresponding signal at its output commensurate with magnetic amplifier functionality. Further clarification on the magnetic amplifier could be found in Young and Aaron (2015).

4.3.4 Pitch Servo System

The servo system as a high energy unit of the pitch control system is actuated by the amplified control signal at the output of the magnetic amplifier. It is actuated in order to eliminate or reduce the error in angular orientation between the actual and reference angular positions. It consists of the servomotor, gears, clutch, follow up transmitter and the rate generator. The servomotor as a rotary actuator is bi-directional and gives precise control of the angular position. Its speed is transduced and fed back to the pitch controller by the rate generator which serves as a kind of tachogenerator. The servomotor responds to its input signal in terms of magnitude and phase. The follow up transmitter communicates actual servo position signal to the pitch transmitter of the gyro control unit. This signal is combined with the MEMS vibratory gyroscope output reference position signal to generate control input signal of the pitch controller. The gears of the servo system match the servomotor with the follow up transmitter and the elevator in terms of speed and torque. The clutch engages or disengages power transmission from the servomotor to the elevator by connecting or disconnecting their shafts all by way of the gears.

4.4 Mathematical Modelling of the Pitch Control System Elements

4.4.1 Modelling of the Gyro Control Unit

Modelling of the MEMS vibratory gyroscope

Kindly see Chapter 3 for the modelling of the MEMS vibratory gyroscope.

Modelling of the pitch and follow up transmitters

The pitch transmitter is modelled in accordance with Equation (4.1).

$$V_{\theta_{Ref}}(t) - V_{\theta}(t) = K_{tr}\theta_C(t) = K_{tr}(\theta_{ref}(t) - \theta(t)) = V_e(t) \tag{4.1}$$

where, $V_{\theta_{Ref}}(t)$ = voltage signal in volts at the output of the pitch transmitter corresponding to the pitch reference angle θ_{Ref}

$V_{\theta}(t)$ = voltage signal in volts at the output of the follow up transmitter corresponding to the actual pitch angle $\theta(t)$

K_{tr} = the gain of the follow up or pitch transmitter in volt/deg

$\theta_C(t)$ = the pitch angle error in degrees whose corresponding voltage serves as input to the pitch controller

$\theta_{ref}(t)$ = reference pitch angle in degrees at the output of the MEMS vibratory gyroscope equivalent to the input angular rate

$\theta(t)$ = actual pitch angle of operating aircraft in degrees

$V_e(t)$ = error voltage in volts at the input of the amplifier due to the angular error $e_{\theta}(t)$ at time t

4.4.2 Modelling of the Pitch Controller

The pitch controller is modelled as a Proportional (P), Integral (I), Derivative controller or their combinations or as a fuzzy-based controller. For a typical PID controller, the control signal is given by equation (4.2).

$$U(t) = K_P e(t) + K_I \int_0^t e(t)d(t) + K_d \frac{de(t)}{dt} \tag{4.2}$$

where, $U(t)$ = control voltage signal in volts

$e(t)$ = error

K_p = proportional gain

K_I = integral gain

K_d = derivative gain

t = time in seconds

4.4.3 Modelling of the Servo Amplifier

The servo amplifier is modelled according to Equation (4.3).

$$V_{\delta e}(t) = k_1 k_2 V_e(t) = K_{s\dot{a}} V_e(t) \tag{4.3}$$

where, $V_{\delta e}(t)$ = voltage at the output of the magnetic amplifier in volts at time t responsible for generating the elevator deflection $\delta_e(t)$

k_1 = the gain of the amplifier

k_2 = the gain of the magnetic amplifier

$K_{s\dot{a}} = k_1 k_2$ = the gain of the servo amplifier

4.4.4 Modelling of the Pitch Servo System

The servo system consists of electrical and mechanical components. The electrical component consists of resistance, inductance, input voltage and the back electromotive force. The mechanical part consists of motor shaft, inertia of the motor, load inertia and damping (Chen *et al.*, 2016). It exhibits excellent torque-speed characteristics and controlled by changing the voltage signal connected to the input. The non-linear equations of the servo system based on Newton's second law combined with Kirchhoff's voltage law are given in Equations (4.4) and (4.7) (Pyrhonen *et al.*, 2016). The equations for the electrical side of the system are:

$$V_a(t) = R_a i_a(t) + L_a \frac{di_a(t)}{dt} + V_b(t) \tag{4.4}$$

where, V_a = armature voltage of the servo motor in volts

R_a = armature resistance of the servo motor in ohms

i_a = armature current of servo motor in amperes

L_a = inductance of armature of servo motor in Henry

V_b = back electromotive force (EMF) in volts

But,

$$V_b(t) = K_b \frac{d\theta(t)}{dt} \tag{4.5}$$

where, K_b = back EMF constant of servo motor

θ = output signal

$$V_a(t) = R_a i_a(t) + L_a \frac{di_a(t)}{dt} + K_b \frac{d\theta(t)}{dt} \tag{4.6}$$

The equations for the mechanical side of the system are:

$$T_{app}(t) = J \frac{d^2\theta(t)}{dt^2} + B \frac{d\theta(t)}{dt} \tag{4.7}$$

where, $T_{app}(t)$ = applied torque

B = damping coefficient

J = inertia of the motor

But,

$$T_{app}(t) = K_T i_a(t) \tag{4.8}$$

where, K_T = torque constant

$$J \frac{d^2\theta(t)}{dt^2} + B \frac{d\theta(t)}{dt} = K_T i_a(t) \tag{4.9}$$

To develop the state space equations of the servo system, the state variables are defined as the outputs of the integrators, with x_1 being i_a, x_2 being θ, and x_3 being $d\theta/dt$, respectively. Hence, from Equations (4.8) and (4.9), Equations (4.10) and (4.11) respectively, are obtained by way of rearrangement.

$$\frac{di_a(t)}{dt} = -\left(\frac{R_a}{L_a}\right) i_a(t) - \left(\frac{K_b}{L_a}\right) \frac{d\theta(t)}{dt} + \left(\frac{1}{L_a}\right) V_a(t) \tag{4.10}$$

$$\frac{d^2\theta(t)}{dt^2} = -\left(\frac{B}{J}\right) \frac{d\theta(t)}{dt} + \left(\frac{K_T}{J}\right) i_a(t) \tag{4.11}$$

With respect to the definition for the state variables, and defining $u(t)$ as $V_a(t)$ and $y(t)$ as $\theta(t)$, then, the state and output equations become:

$$\dot{x}_1(t) = -\left(\frac{R_a}{L_a}\right)x_1(t) - \left(\frac{K_b}{L_a}\right)x_3(t) + \left(\frac{1}{L_a}\right)u(t) \tag{4.12}$$

$$\dot{x}_2(t) = x_3(t) \tag{4.13}$$

$$\dot{x}_3(t) = -\left(\frac{B}{J}\right)x_3(t) + \left(\frac{K_T}{J}\right)x_1(t) \tag{4.14}$$

$$y(t) = x_2(t) \tag{4.15}$$

The state and output equations of the servo system are represented in Equations (4.18) and (4.19), respectively.

$$\dot{x}(t) = Ax(t) + Bu(t) \tag{4.16}$$

$$y(t) = Cx(t) \tag{4.17}$$

$$\begin{bmatrix} \dot{x}_1(t) \\ \dot{x}_2(t) \\ \dot{x}_3(t) \end{bmatrix} = \begin{bmatrix} -R_a/L_a & 0 & -K_b/L_a \\ 0 & 0 & 1 \\ K_T/J & 0 & -B/J \end{bmatrix} \begin{bmatrix} x_1(t) \\ x_2(t) \\ x_3(t) \end{bmatrix} + \begin{bmatrix} 1/L_a \\ 0 \\ 0 \end{bmatrix} u(t) \tag{4.18}$$

$$y(t) = \begin{bmatrix} 0 & 1 & 0 \end{bmatrix} \begin{bmatrix} x_1(t) \\ x_2(t) \\ x_3(t) \end{bmatrix} \tag{4.19}$$

4.5   Design of Controllers

For the purpose of this research, the following pitch controllers are designed: Proportional-Integral-Derivative (PID) controller, Proportional-Integral (PI) controller, Fuzzy-PID controller, Fuzzy-PI controller and Adaptive Neuro-Fuzzy Interference System (ANFIS) controller.

4.5.1   Proportional-Integral Controller

Equation (4.20) (Dogruer and Tan, 2018), gives the governing equation of a PI controller.

$$U_{\theta_c}(t) = K_p e_{\theta_c}(t) + K_i \int_0^t e_{\theta_c}(t)dt \tag{4.20}$$

where, $U_{\theta_c}(t)$ = control voltage signal at the output of the pitch controller in volts

$e_{\theta_c}(t)$ = the error signal generated by the pitch and follow up transmitters in volts

4.5.2 Proportional-Integral-Derivative Controller

A PID controller has three terms namely, proportional, integral and derivative. It is used in many applications. Advantages of using a PID controller are the elimination of steady-state error and overshoots and the improvement of system stability (Palaniyappan *et al*., 2018). The mathematical equation of a PID controller is represented by Equation (4.21) (Rout *et al*., 2016).

$$U_{\theta_c}(t) = K_p e_{\theta_c}(t) + K_i \int_0^t e_{\theta_c}(t)dt + K_d \frac{d}{dt} e_{\theta_c}(t) \qquad (4.21)$$

Table 4.1 shows the values of Proportional, Integral and Derivative gains of PI and PID controllers, respectively used in the simulations. Below is the tuning procedure used to obtain the gains.

i. First, note whether the required proportional control gain is positive or negative. To do so, step the input u up (increased) a little, under manual control, to see if the resulting steady state value of the process output has also moved up (increased). If so, then the steady-state process gain is positive and the required Proportional control gain, K_c, has to be positive as well;

ii. Turn the controller to P-only mode, i.e. turn both the Integral and Derivative modes off;

iii. Turn the controller gain, K_c, up slowly (more positive if K_c was decided to be so in step 1, otherwise more negative if K_c was found to be negative in step 1) and observe the output response. Note that this requires changing K_c in step increments and waiting for a steady state in the output, before another change in K_c is implemented;

iv. When a value of K_c results in a sustained periodic oscillation in the output (or close to it), mark this critical value of K_c as K_u, the ultimate gain. Also, measure the period of oscillation, P_u, referred to as the ultimate period. Hint: for the system A in the PID simulator, K_u should be around 0.7 and 0.8; and

v. Using the values of the ultimate gain, K_u, and the ultimate period, P_u, Ziegler and Nichols prescribes the following values for K_c, t_I and t_D, depending on which type of controller is desired.

Table 4.1 Proportional, Integral and Derivative Gains of PI and PID Controllers

SN	Parameter	Controller	
		PI	PID
1.	K_p	0.207	0.207
2.	K_i	2.067	2.067
3.	K_d	-	1.7×10^{-3}

4.5.3 Fuzzy-PID Controller

Fuzzy PID controller is a conventional PID regulator but based on fuzzy set theory, under the absolute control error and deviation change and the absolute value of the rate, automatically adjusting the proportional coefficient K_p, integral coefficient K_i and differential factor K_d of the fuzzy controller. It is a nonlinear control mechanism using fuzzy reasoning algorithm (Torabi *et al*., 2018). Fig. 4.4 shows the structure of a fuzzy-PID controller. With the inputs as error (e) and the derivative of error ($\dot{e}$) whilst the controller output signal is u.
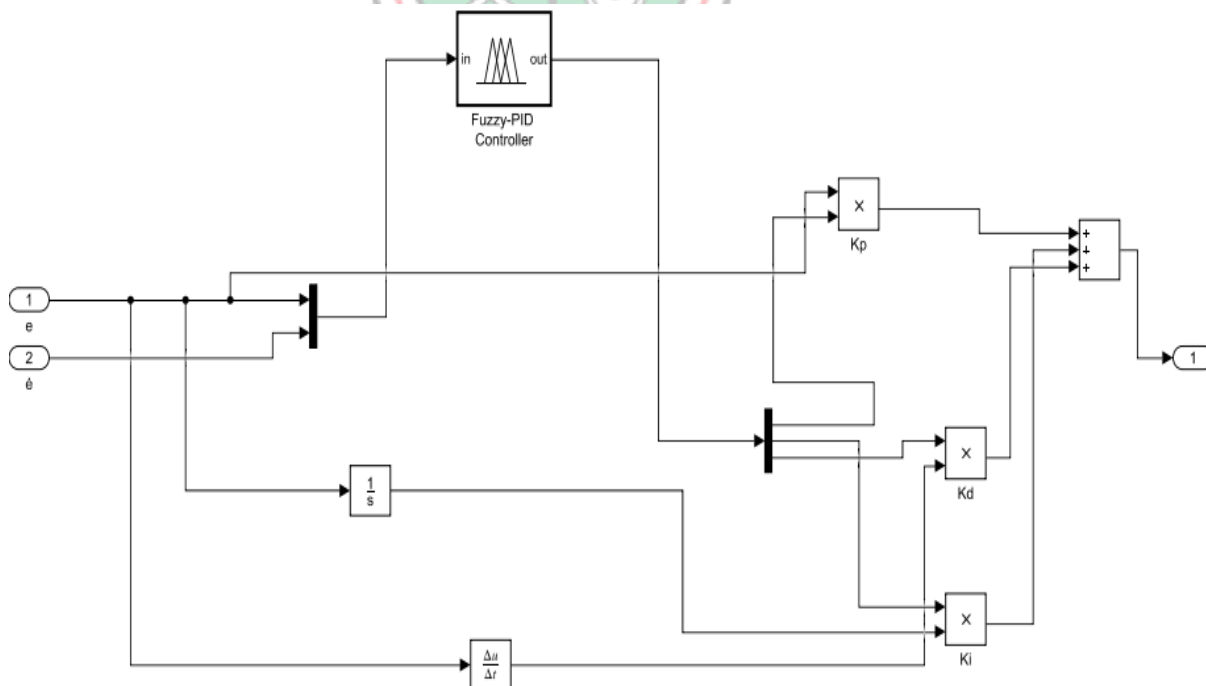
Fig. 4.4 Structure of the Fuzzy-PID Controller

The rule base for the fuzzy controllers considers the following memberships for the error and derivative of error: Negative Big (NB), Negative Small (NS), Zero (Z), Positive Medium (PM), Positive Big (PB), Medium (M), Very Small (VS), Very Big (VB), Very Large (VL), Medium Big (MB) and Medium Small (MS). Tables 4.2, 4.3 and 4.4 give the rule base for the coefficients K_p, K_i and K_d, respectively. Membership function, input and output variables, rule viewer and surface viewer of the fuzzy-PI controller are as shown in Fig. 4.5, Fig. 4.6, Fig. 4.7 and Fig. 4.8, respectively.

Table 4.2 Rule Base for the Proportional Controller Coefficient K_p

Δe/e	NB	NM	NS	Z	PS	PM	PB
NB	VL	VL	VB	VB	MB	M	M
NM	VL	VL	VB	MB	MB	M	MS
NS	VB	VB	VB	MB	M	MS	MS
Z	VB	VB	MB	M	MS	VS	VS
PS	MB	MB	M	MS	MS	VS	VS
PM	VS	MB	M	MS	VS	VS	Z
PB	M	M	VS	VS	VS	Z	Z

Table 4.3 Rule Base for the Integral Controller Coefficient K_i

Δe/e	NB	NM	NS	Z	PS	PM	PB
NB	Z	Z	VS	VS	MS	M	M
NM	Z	Z	VS	MS	MS	M	M
NS	Z	VS	MS	MS	M	MB	MB
Z	VS	VS	MS	M	MB	VB	VB
PS	VS	MS	M	MB	MB	VB	VL
PM	M	M	MB	MB	VB	VL	VL
PB	M	M	MB	VB	VB	VL	VL

70

Table 4.4 Rule Base for the Derivative Controller Coefficient K_d

Δe/e	NB	NM	NS	Z	PS	PM	PB
NB	MB	MS	Z	Z	Z	VS	MB
NM	MB	VS	Z	VS	VS	MS	M
NS	M	MS	VS	MS	M	MB	MB
Z	M	MS	MS	MS	MS	MS	M
PS	M	M	M	M	M	M	M
PM	VL	MS	MB	MB	MB	MB	VL
PB	VL	VB	VB	VB	MB	MB	VL

Fig. 4.5 Membership Function of Fuzzy-PID Controller
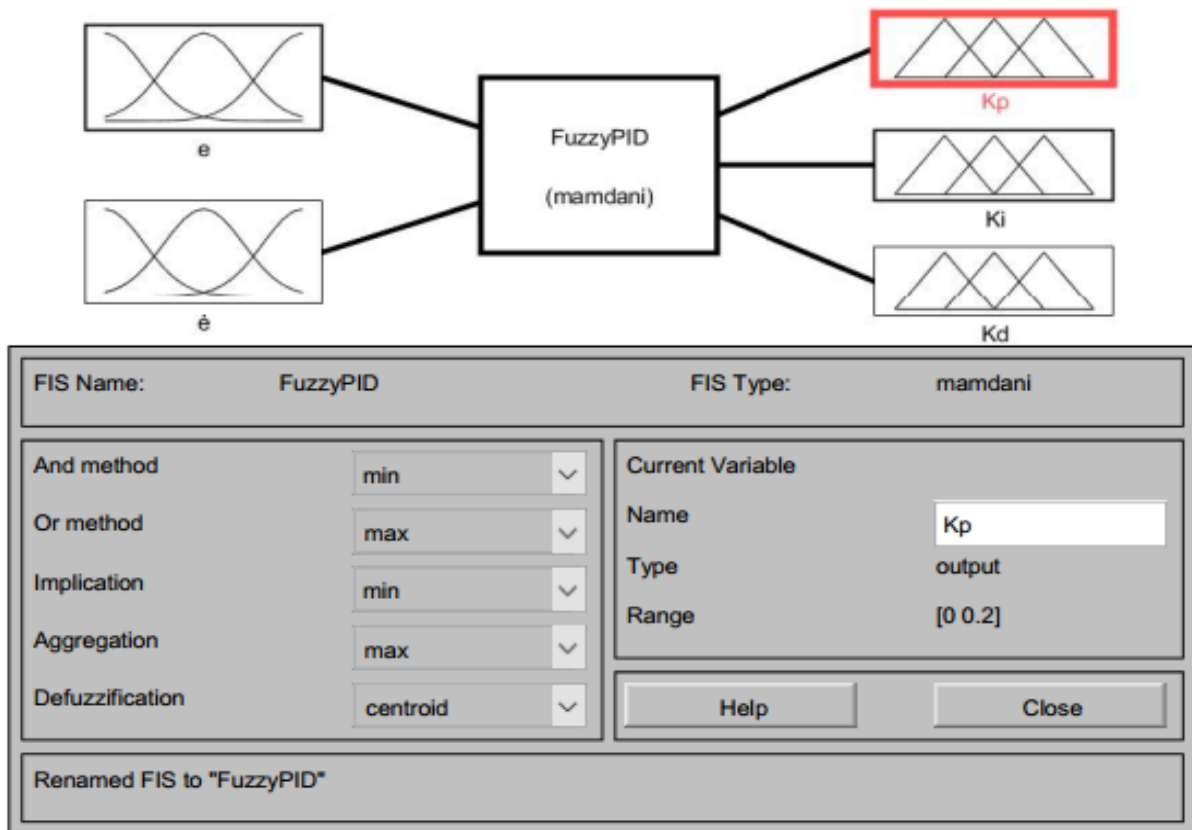
Fig. 4.6 Mamdani-based Fuzzy-PID Controller Input and Output Variables
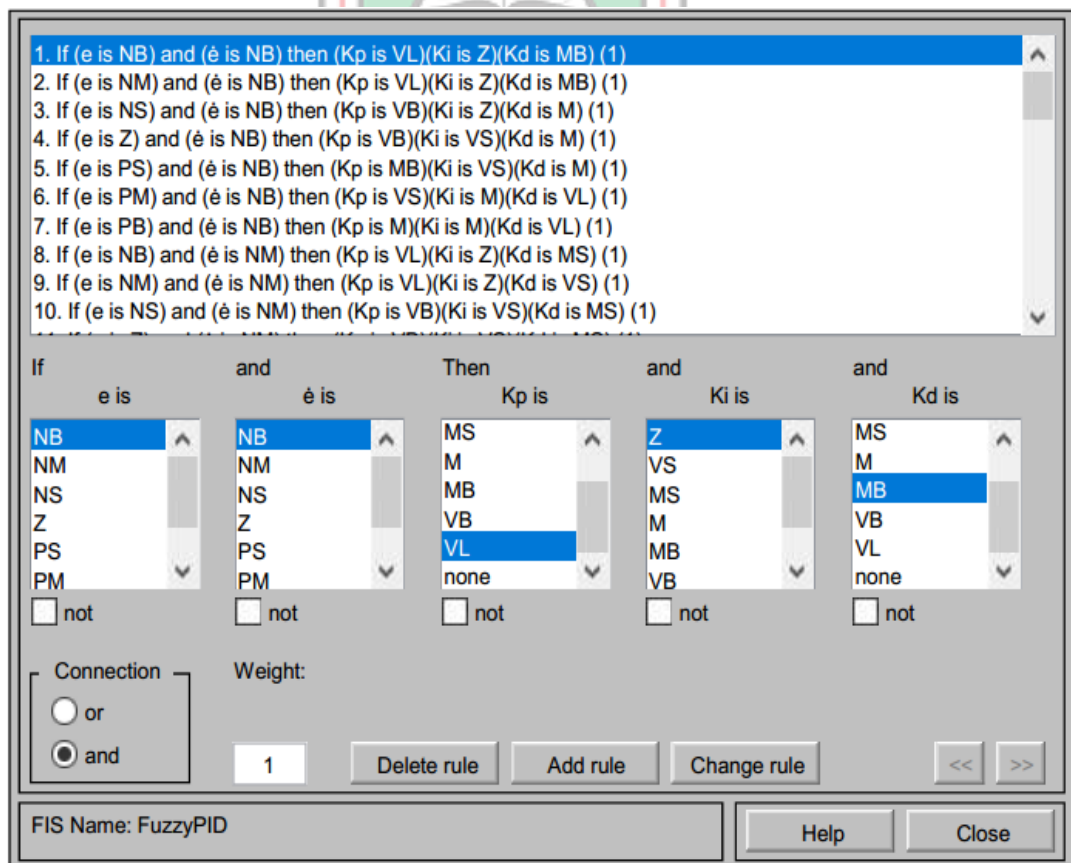
Fig. 4.7 Rule Viewer for Fuzzy-PID Controller
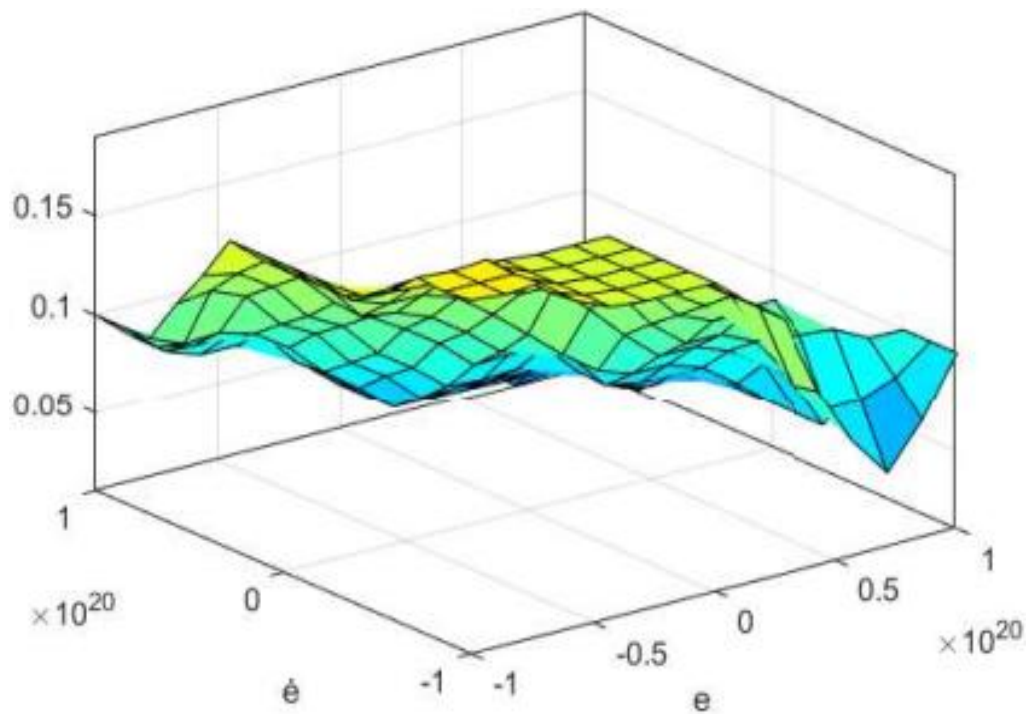
Fig. 4.8 Surface Viewer of Fuzzy-PID Controller

4.5.4 Fuzzy-PI Controller

The structure of the fuzzy-PI controller is shown in Fig. 4.9 where it differs from the fuzzy-PID controller by the absence of the D-controller. The rule base for the controller coefficients K_p and K_i are illustrated in Table 4.2 and Table 4.3, respectively. The membership function, input and output variables, rule viewer and surface viewer of the fuzzy-PI controller are shown in Fig. 10, Fig. 11, Fig. 12 and Fig. 13, respectively.
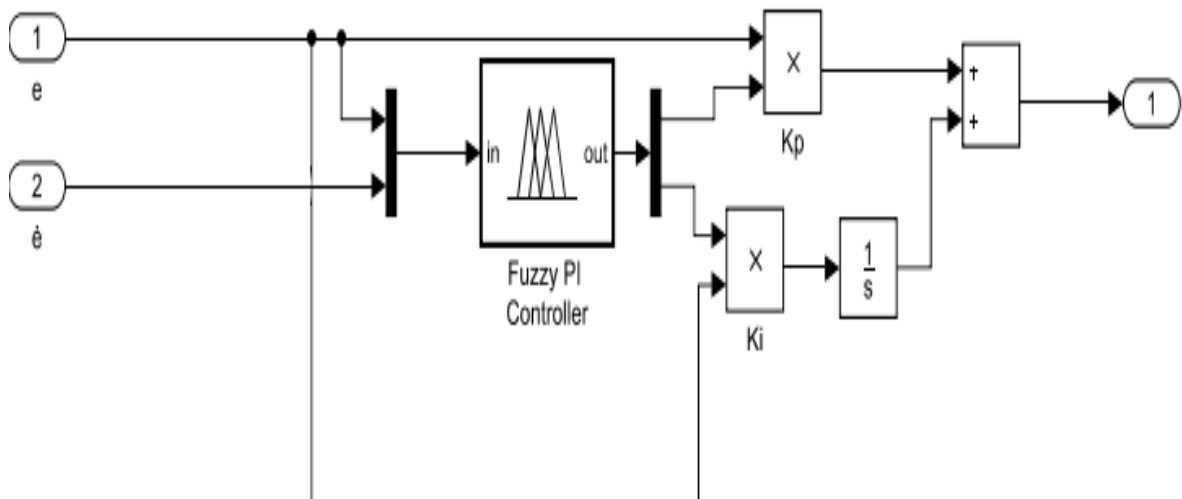
Fig. 4.9 Structure of the Fuzzy-PI Controller
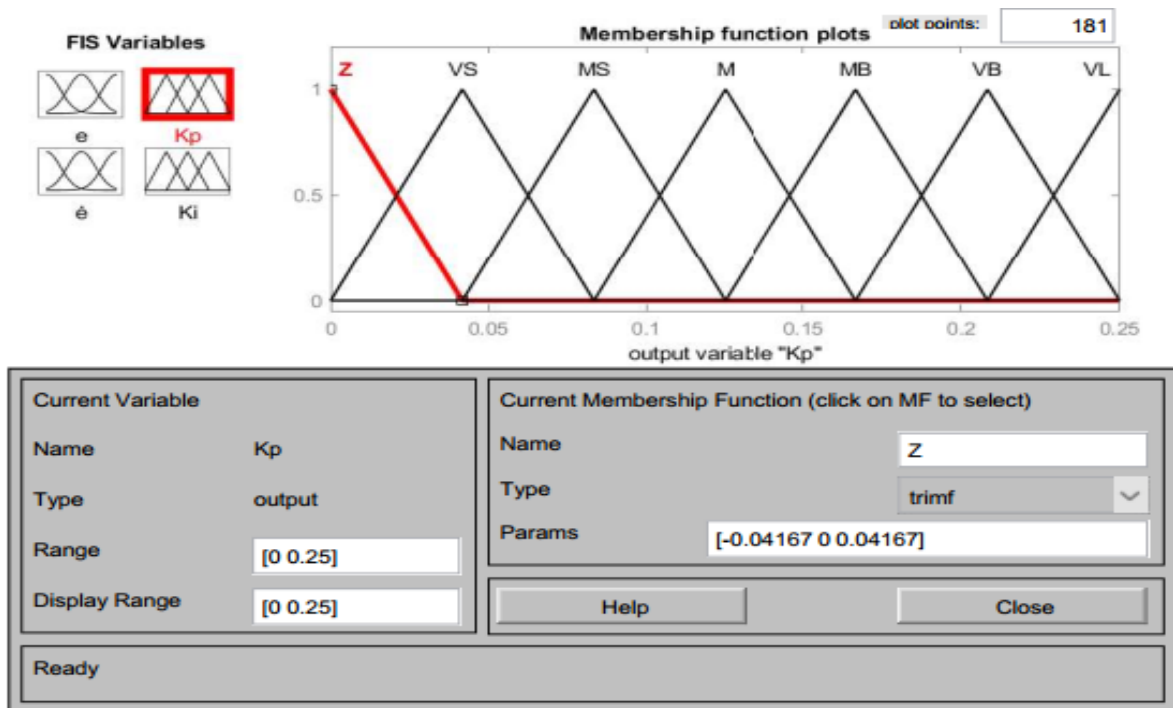
Fig. 4.10 Membership Function of Fuzzy-PI Controller
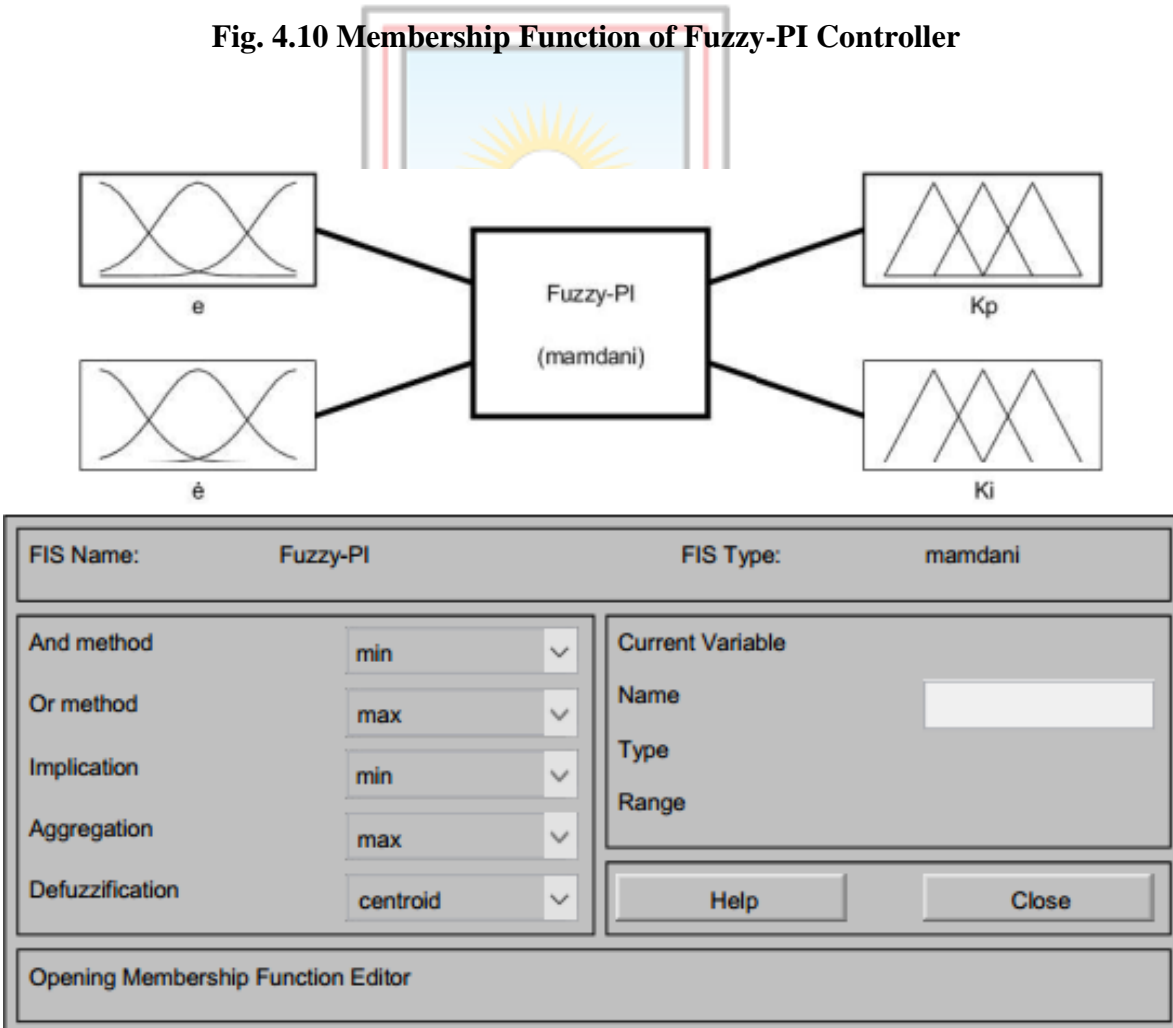
Fig. 4.11 Mamdani-based Fuzzy-PI Controller Input and Output Variables
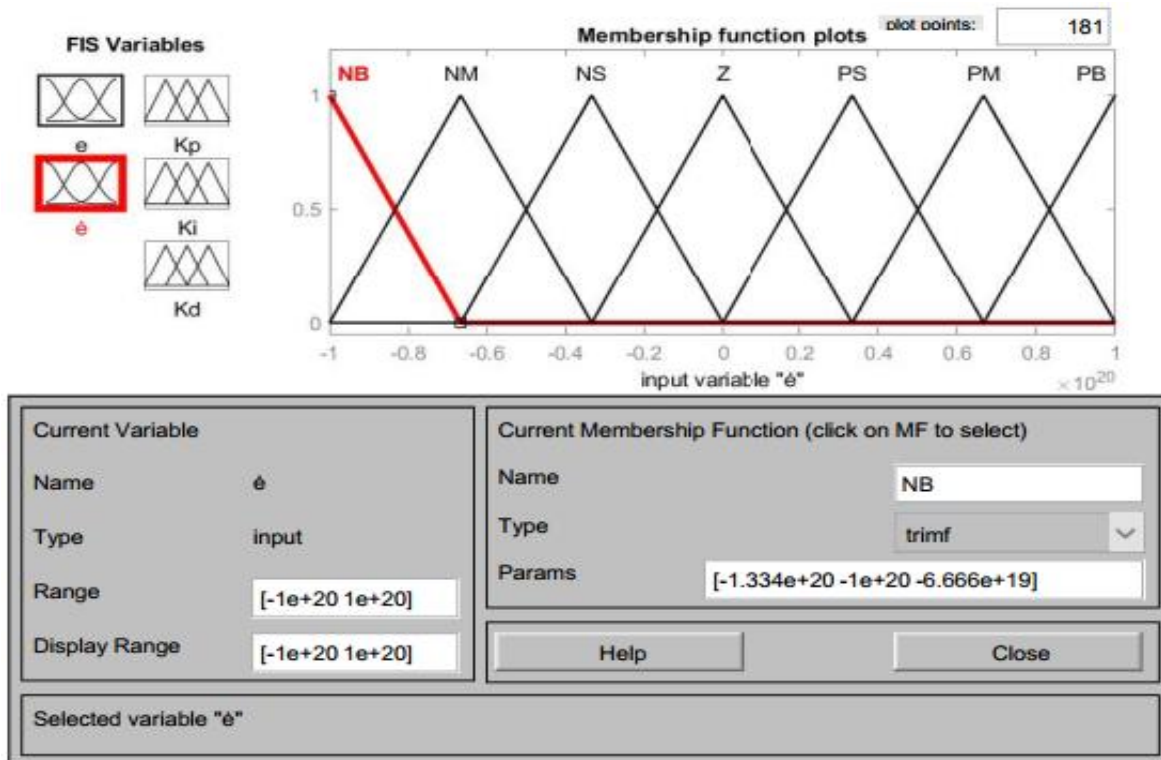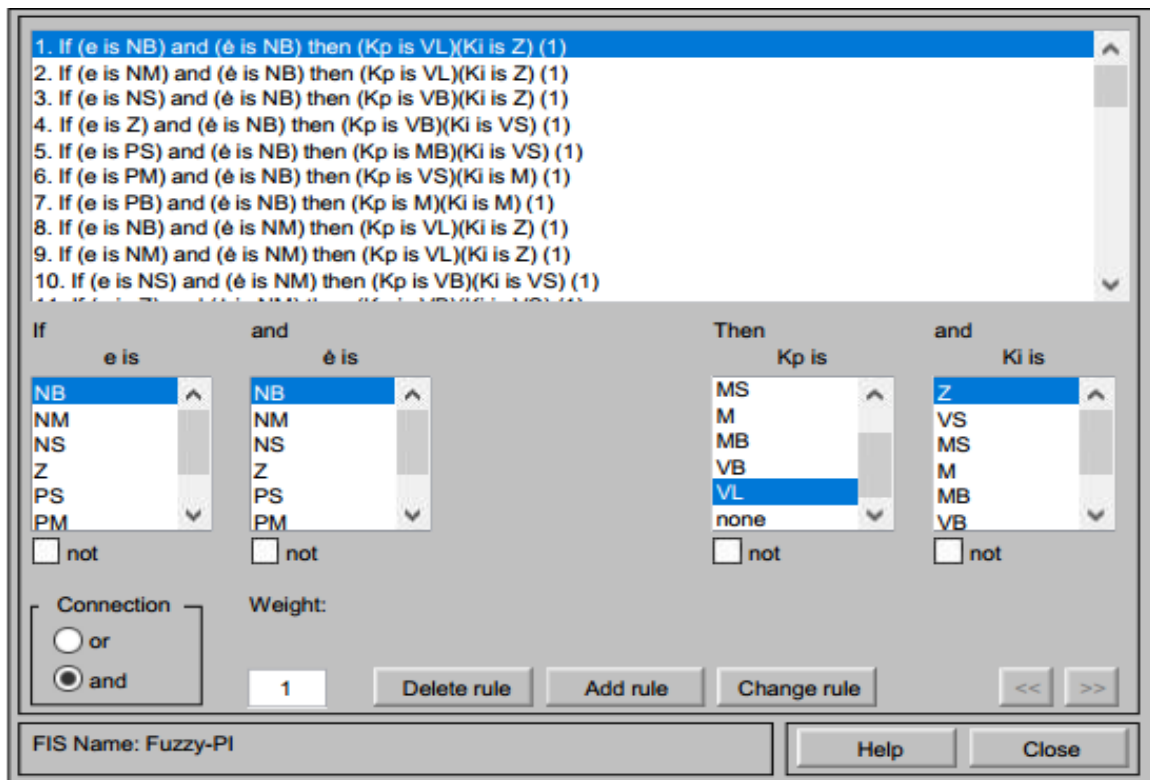
Fig. 4.12 Rule Viewer for Fuzzy-PI Controller
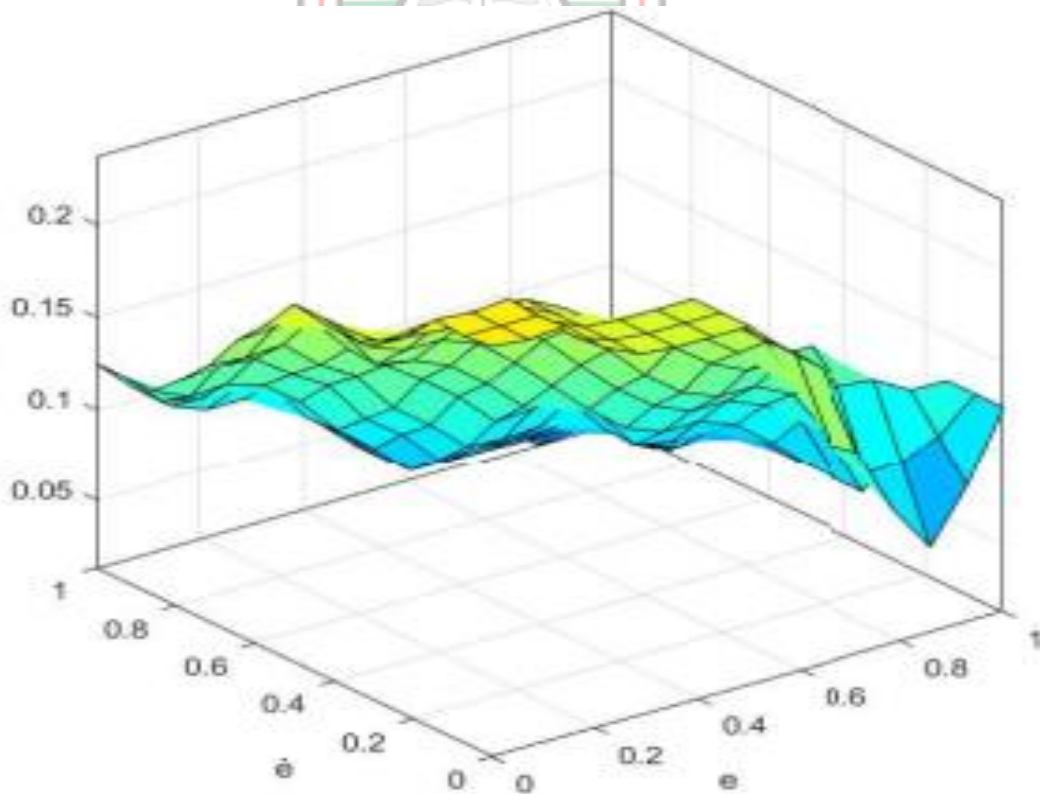
Fig. 4.13 Surface Viewer for Fuzzy-PI Controller

4.5.5   Adaptive Neuro-Fuzzy Inference System Controller

Adaptive Neuro-Fuzzy Inference System (ANFIS) is a hybrid structure consisting of neural system and fuzzy frameworks in such a manner that neural system is utilised to decide the parameters of fuzzy framework. ANFIS to a large extent expels the prerequisite for manual enhancement of the fuzzy framework parameters. A neural system is utilised to consequently tune the fuzzy parameters. ANFIS with learning ability of neural system and with benefits of the standard base fuzzy framework can considerably enhance controller performance. The structure of the ANFIS controller contains five layers, as shown in Fig. 4.14. In Layer 1, the node output is the membership function for the input variables x and y. The node output of Layer 2 is the product of membership functions for each variable which is called the firing strength. The node output in Layer 3 is a normalised firing strength. The adaptive node is represented by the fourth layer and finally, the summation of all the rules' output is done in Layer 5.
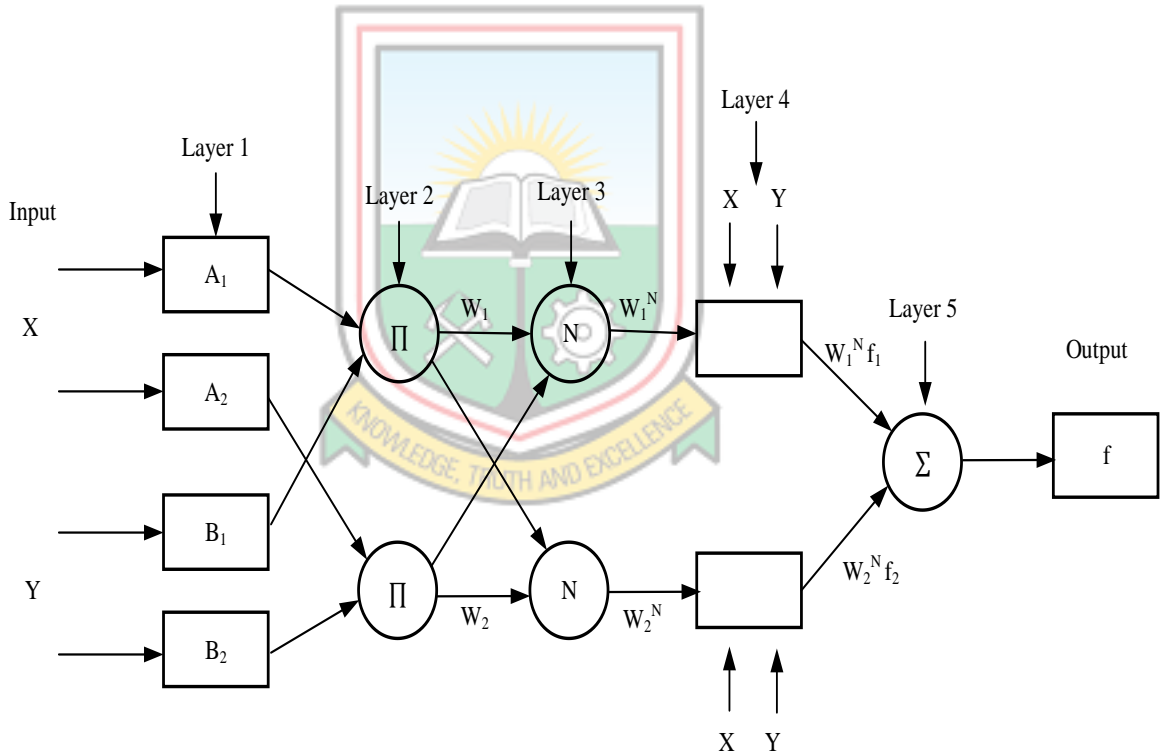
Fig. 4. 14 Layered Structure of the ANFIS Controller

The crisp inputs x and y to the node of the first layer and the output O_{1i} of this node are defined as in Equation (4.22) (Ewees and Elaziz, 2018; Ewees *et al.*, 2017).

$$O_{1i} = \mu A_i(x),\ i=1,2,\ O_{1i} = \mu B_{i-2}(y),\ i=3,4, \qquad (4.22)$$

where, A_i and B_i = the membership values of the generalised Gaussian membership function

The Gaussian membership function is expressed by Equation (4.23) (Handoyo and Efendi, 2019; Radhakrishna *et al*., 2017).

$$\mu(x) = e^{-}(x - \frac{p_i}{\sigma_i})^2 \tag{4.23}$$

where, p_i and σ_i = the premise parameters

In the second layer, the node's output is the firing strength of a rule given as in Equation (4.24) (Ewees *et al*., 2017; Khalil *et al*., 2018).

$$O_{2i} = \mu A_i(x) \times \mu B_{i-2}(y) \tag{4.24}$$

The node's output in the third layer is the normalised firing strength given by Equation (4.25) (Barman *et al*., 2016; Khalil *et al*., 2018).

$$O_{3i} = \bar{w}_i = \frac{\omega_i}{\sum_{(i-1)}^{2} \omega_i} \tag{4.25}$$

The node in Layer 4 is an adaptive node and its output is computed by equation (4.26).

$$O_{4,i} = \bar{w}_i f_i = \bar{w}_i (p_i x + q_i y + r_i) \tag{4.26}$$

where, p_i, q_i and r_i = the consequent parameters of the node i.

In the last layer, there exists only one node whose output is computed by using equation (4.27) (Barman *et al*., 2016; Khalil *et al*., 2018).

$$O_5 = \sum_i \bar{w}_i f_i \tag{4.27}$$

The data training interface, membership function, rule viewer, the surface viewer and the network structure of the ANFIS controller implementation are shown in Fig. 4.15, Fig. 4.16, Fig. 4.17, Fig. 4.18 and Fig. 4.19, respectively.
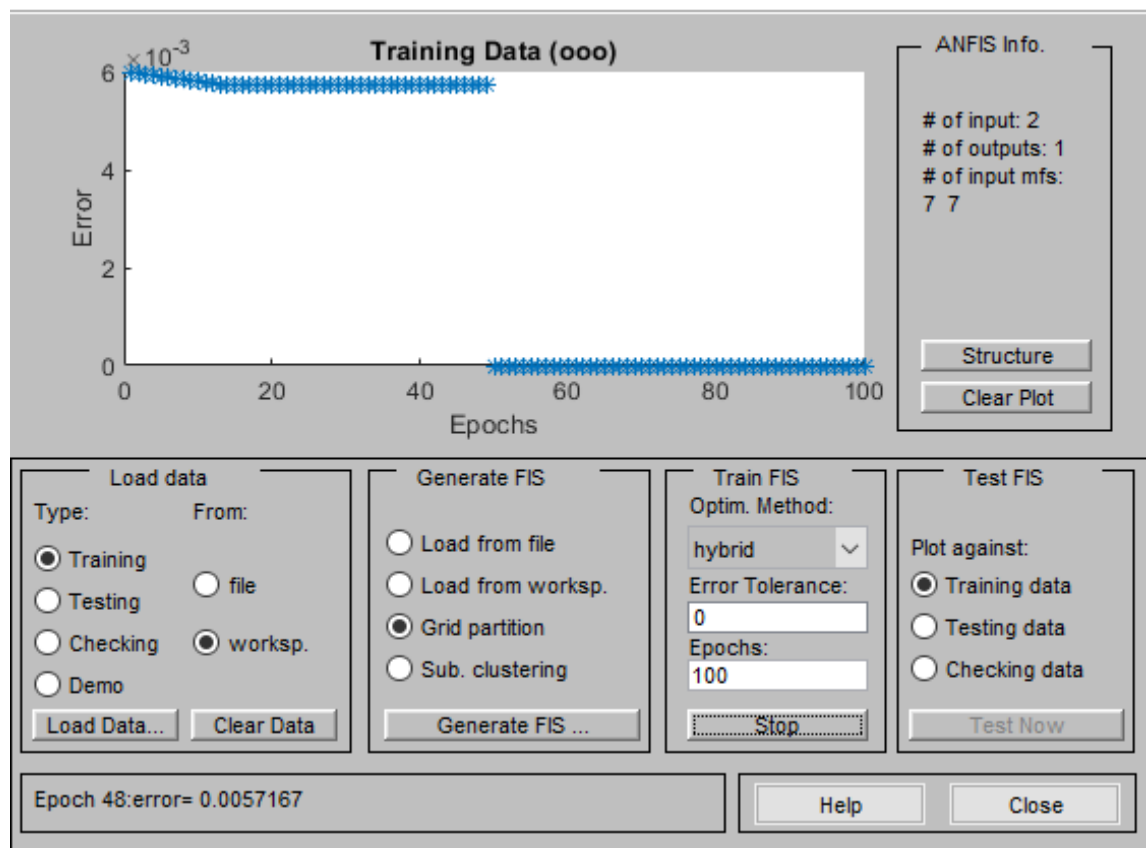
Fig. 4.15 Data Training Interface of ANFIS Controller
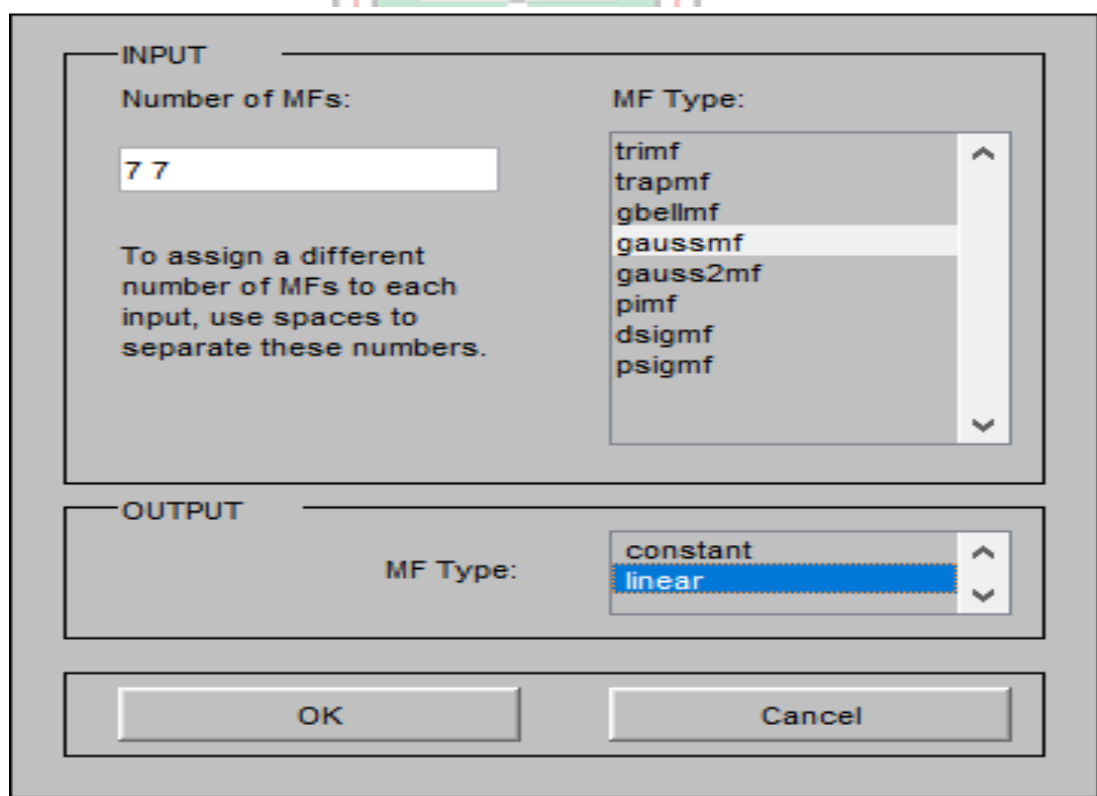
Fig. 4.16 Membership Function for ANFIS Controller
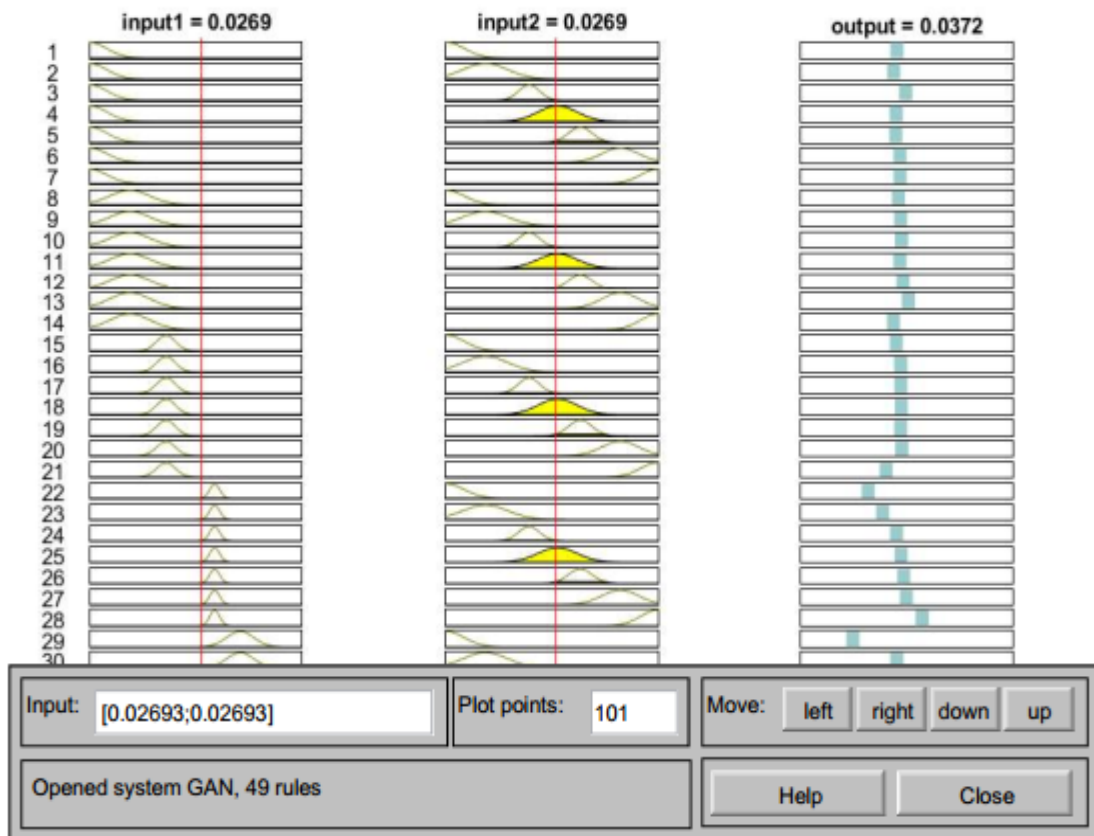
Fig. 4.17 Rule Viewer of ANFIS Controller
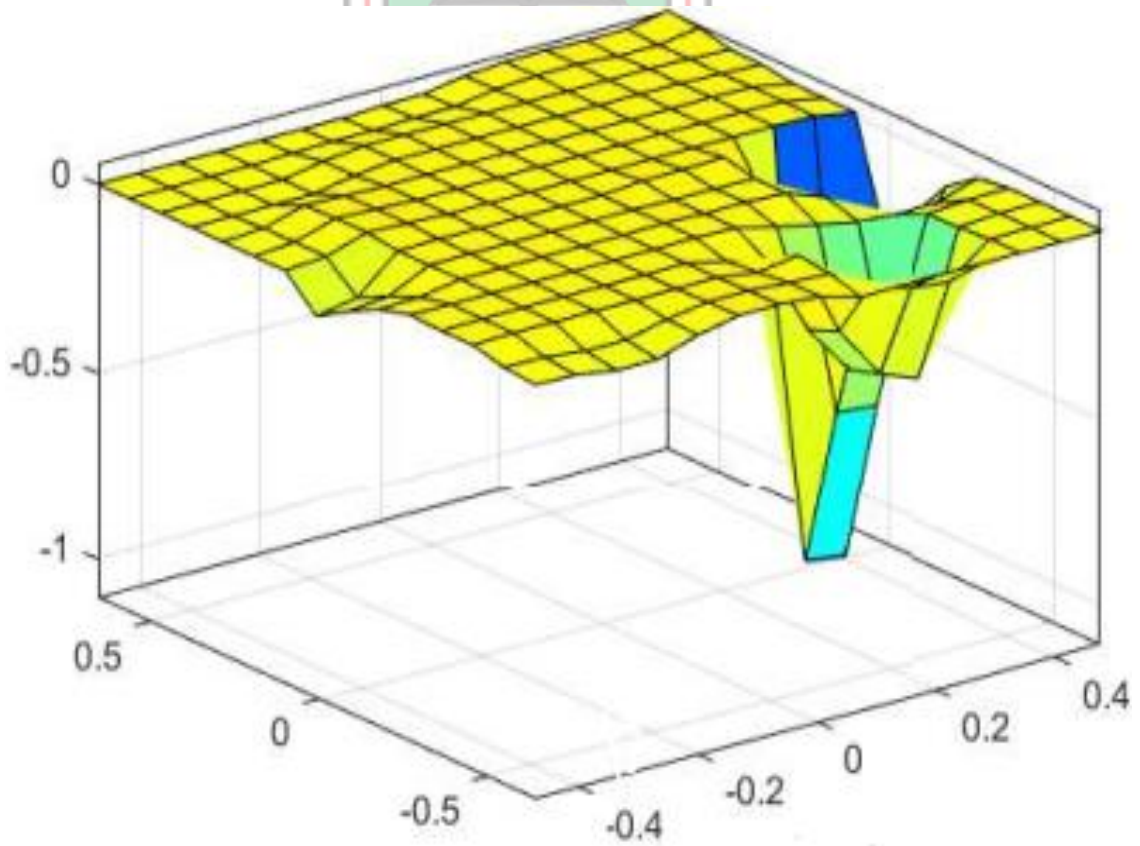
Fig. 4.18 Surface Viewer of ANFIS Controller
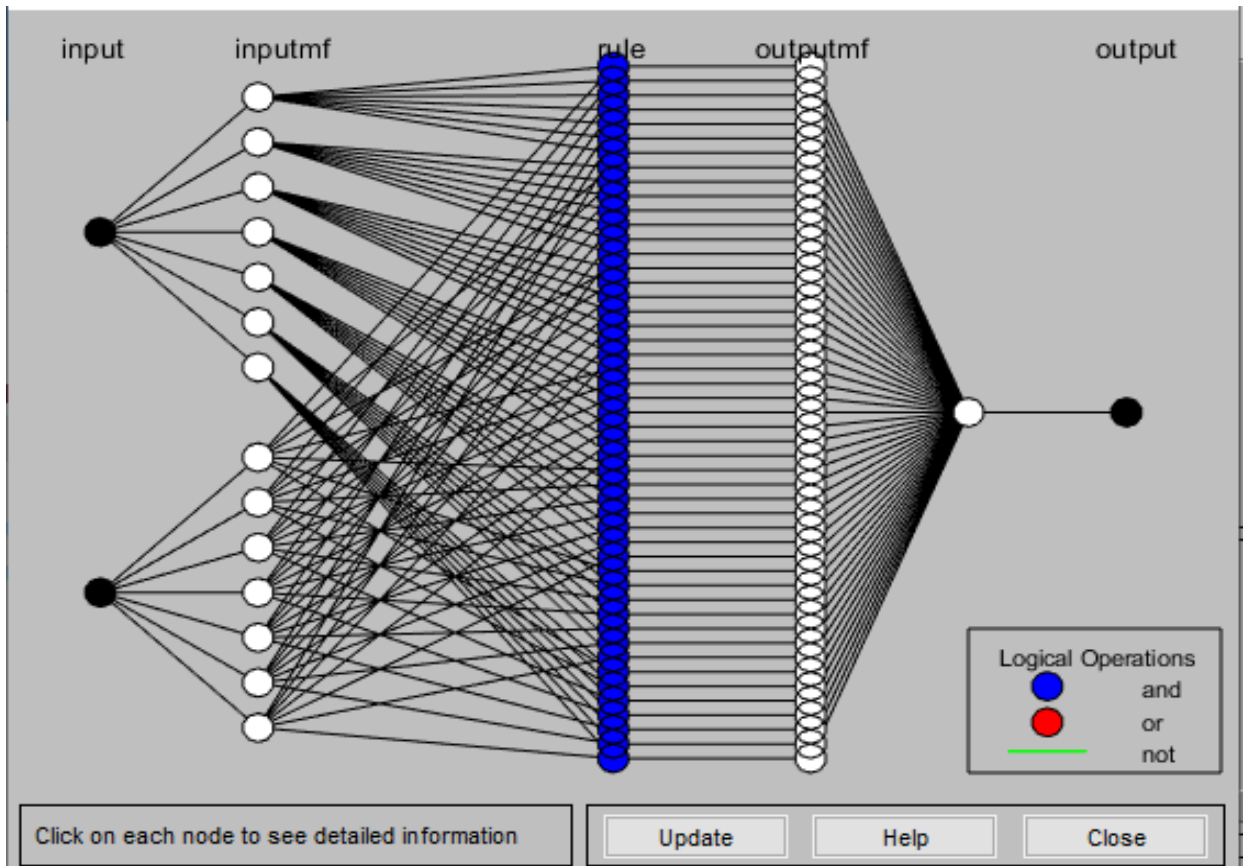
Fig. 4.19 The Network Structure of ANFIS Controller Model

4.6 Computer Simulations of the Pitch Control System

The computer simulations are conducted to find out the ability of each controller to suppress the influence of temperature and noise on the output response of the pitch control system. For the scenarios of the simulations, the pitch angle of 12.5 degrees and 33 degrees are considered for each of the controllers. Also, base case situation is run for 1 sec, then temperature is introduced at 2 secs and the remaining 2 secs is given to both temperature and noise effects. For the pitch control system of the AAS, the standard noise level is 65 dB (Dongwook *et al*., 2016) and the temperature of the aircraft should not exceed 15 ᵒC (O'Donnell and Bacon, 2015). The performance of the controllers are however evaluated against these standards of temperature and noise values. The modelled pitch control system of the AAS is implemented in MATLAB Simulink software as presented in Fig. 4.20.
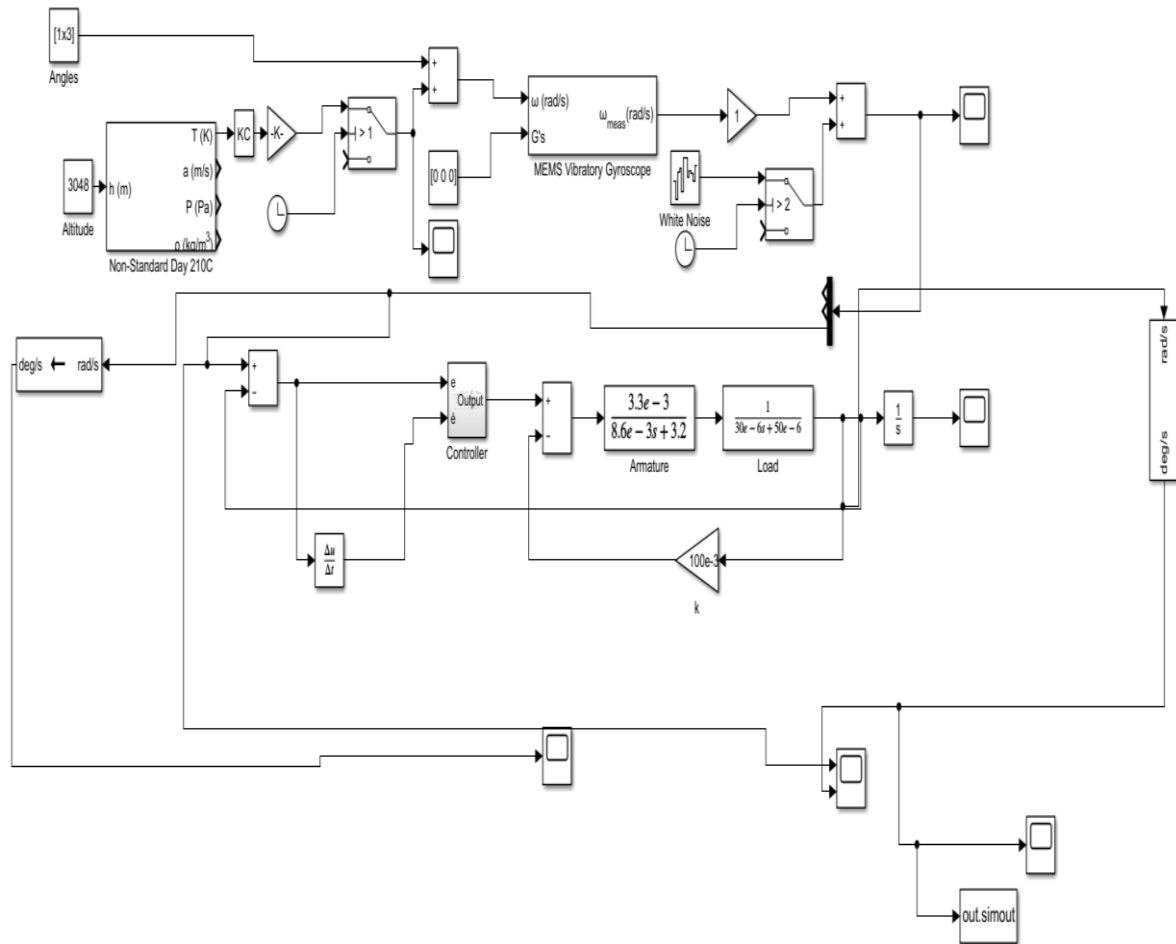
Fig. 4.20 MATLAB Simulink Software Representation of the Modelled Pitch Control System

4.7 Simulation Results and Discussion

4.7.1 Simulation Results

The performance of the controllers in suppressing the temperature and noise effects are evaluated by the response of the control system with regard to rise time (t_r), overshoot (OS%), settling time (t_s), slew rate (s_r) and Root Mean Square Error (RMSE). Fig. 4.21 and Fig. 4.22 show the simulation results of the entire pitch control system of the AAS at 12.5 degrees without any controller (Fig. 4.21) and with controllers (Fig. 4.22), respectively. Fig. 4.23 for no controller action case and Fig. 4.24 for controller action are effected for the angular orientation of 33 degrees. Performance of the various controllers are summarised in Table 4.5.
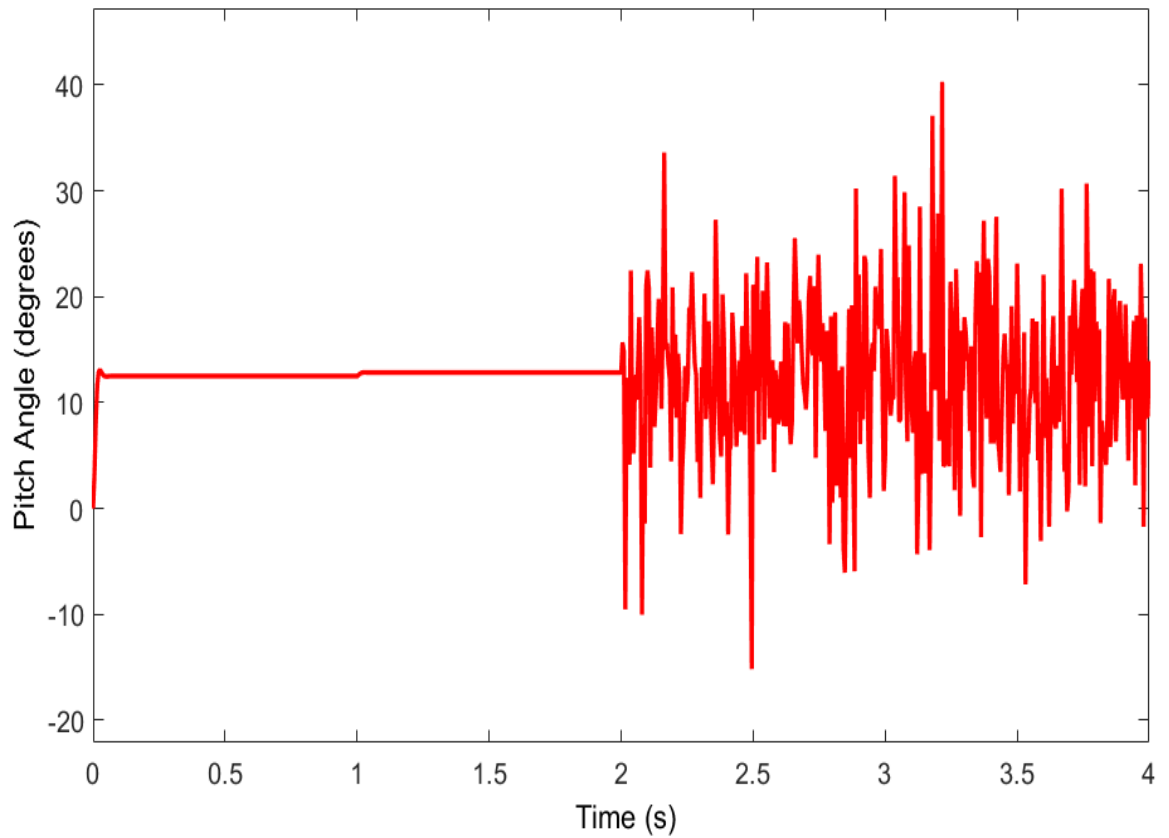
Fig. 4.21 Response of MEMS Vibratory Gyroscope to the Pitch Angle of 12.5 degrees with the Introduction of Temperature without Controller Action
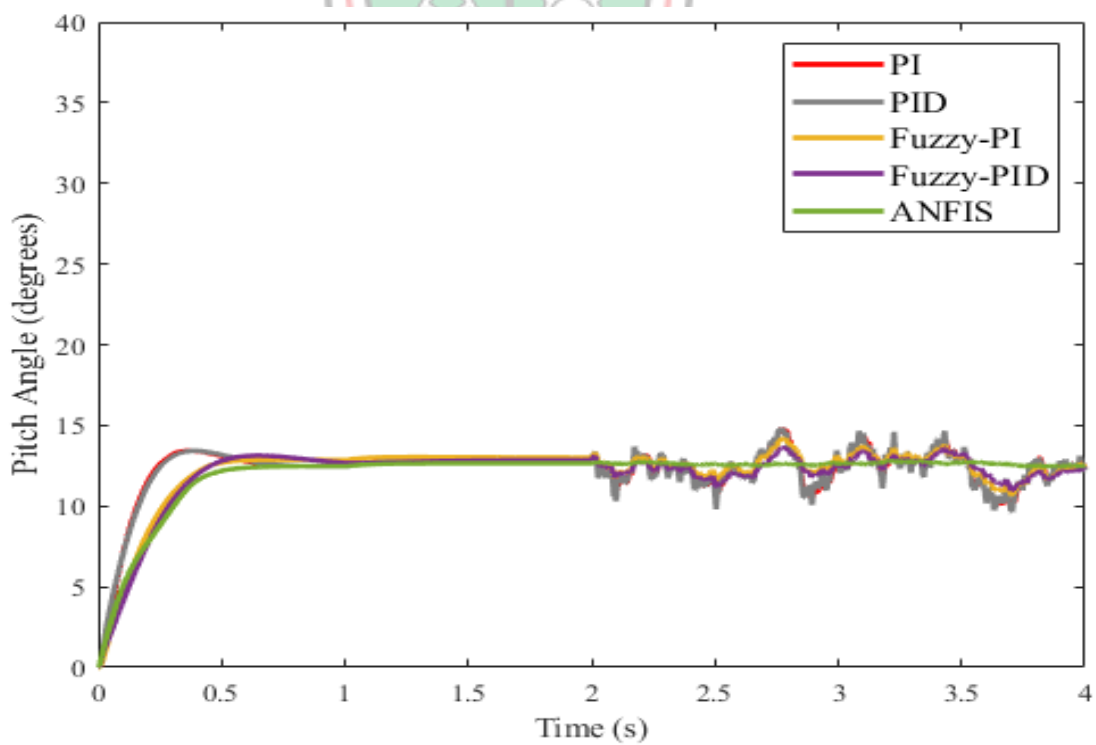
Fig. 4.22 Response of Pitch Control System to the Pitch Angle of 12.5 degrees with the Introduction of Controllers
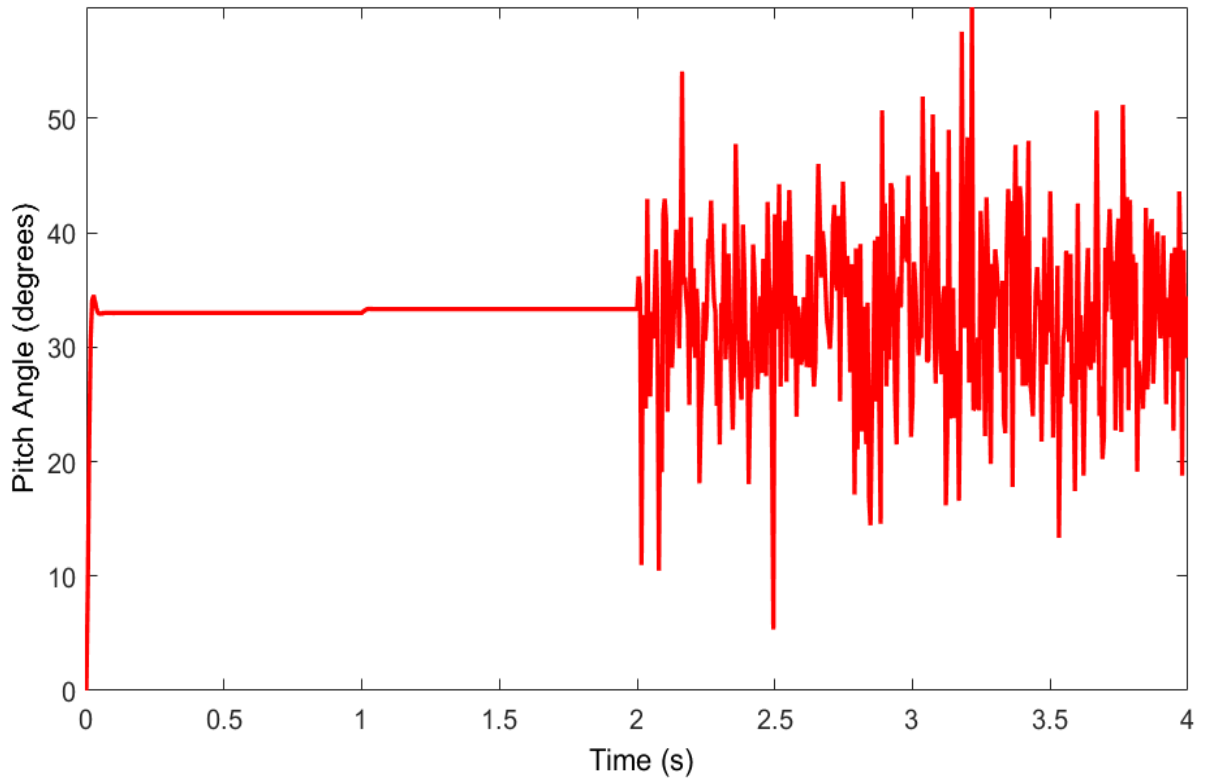
Fig. 4.23 Response of MEMS Vibratory Gyroscope to the Pitch Angle of 33 degrees with the Introduction of Temperature and Noise without Controller Action
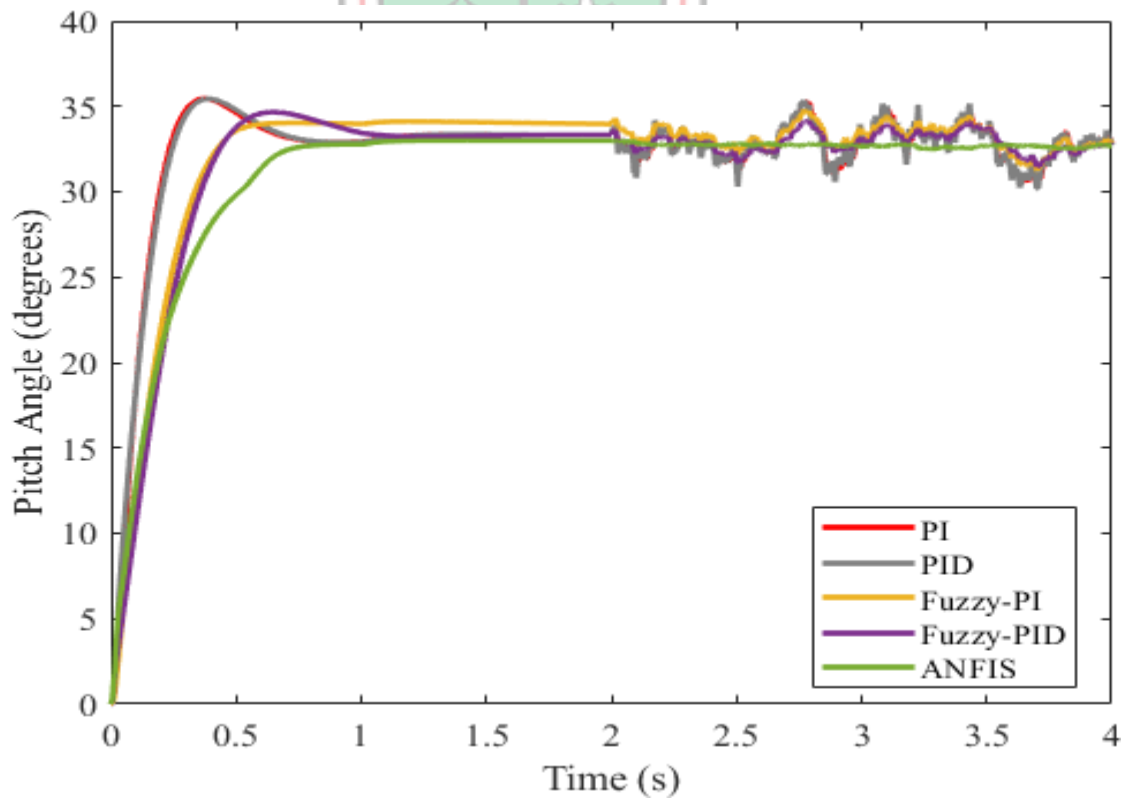
Fig. 4.24 Response of Pitch Control System to the Pitch Angle of 33 degrees with the Introduction of Controllers

Table 4.5 Performance of the Various Controllers

SN	Parameter	Controller					
		PI		PID		Fuzzy PI	
		12.5º	33º	12.5º	33º	12.5º	33º
1.	Rise Time (ms)	177.56	172.55	189.487	184.342	329.158	320.575
2.	Overshoot (%)	4.479	5.45	4.53	5.85	-0.177	-0.08
3.	Settling Time (s)	1.181	1.085	1.027	1	1.073	1.015
4.	Slew Rate (/s)	57.591	154.57	53.914	144.56	31.598	84.769
5.	RMSE	1.0459	1.0459	1.0598	1.0598	0.7271	0.7371

Table 4.5 Cont'd

SN	Parameter	Controller			
		Fuzzy PID		ANFIS	
		12.5º	33º	12.5º	33º
1.	Rise Time (ms)	349.264	352.452	399.123	468.145
2.	Overshoot (%)	2.759	4.737	0.404	0.505
3.	Settling Time (s)	1.073	1.293	0.719	0.796
4.	Slew Rate (/s)	29.1	74.773	25.076	55. 749
5.	RMSE	0.5637	0.5636	0.1447	0.2869

4.7.2   Discussion

From Table 4.5, the ANFIS controller gave better performance in terms of overshoot (0.404% at 12.5 degrees, 0.505% at 33 degrees), settling time (0.719 secs at 12.5 degrees and 0.796 secs at 33 degrees), slew rate (25.076 per sec at 12.5 degrees and 55.749 per sec at 33 degrees) and RMSE (0.1447 at 12.5 degrees and 0.2869 at 33 degrees). The ANFIS controller was followed by fuzzy-PID, fuzzy-PI, PI and PID controllers with respect to the overshoot and settling time. However, fuzzy-PID did better than fuzzy-PI in terms of slew rate. The PI and PID controllers were worst performers in exception of the rise time where they did far better especially the PI controller that gave 177.5 ms against 399.123 ms for ANFIS controller at 12.5 degrees and 172.5 ms against 468.145 ms at 33 degrees. This better performance of the PI controller is explained by the fact that its algorithm is far simpler compared to the ANFIS controller algorithm hence, requires less time of response to its

input signals. The highest poor rise time of 468.145 ms given by the ANFIS controller cannot be tolerated and should require further action.

Clearly, the ANFIS and the fuzzy controllers gave some oscillations after the introduction of noise in addition to the temperature. The way forward is to improve upon the transient and steady state performances of these three controllers and this could be done by deploying AI optimisers. Hopefully, this should improve some of the performance metrics, damp out the remnant oscillations and achieve steady state stability.

4.8   Summary

This chapter presented pitch control as executed by the AAS. Mathematical modelling of the individual subsystems of the proposed pitch control system of the AAS were done. Temperature and noise effects on the pitch control system were investigated by way of modelling and simulations. Simulations outcome proved the ANFIS controller as better than the PI, PID, fuzzy PI and fuzzy PID controllers. Notwithstanding, the ANFIS controller results stand to be improved upon due to the remnant oscillation in order to achieve an oscillation-free pitch angle control by the AAS. In other words, the simulations strongly suggest the need to further mitigate the faults effects of temperature and noise on the performance of the aircraft pitch control system. The further improvement needed is given focus in Chapter 5.
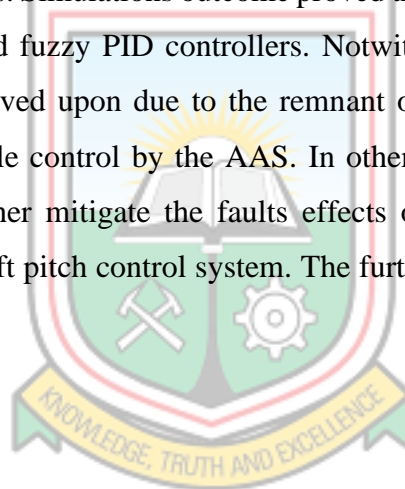
CHAPTER 5

OPTIMAL MITIGATION OF TEMPERATURE AND NOISE EFFECTS OF THE PITCH CONTROL SYSTEM

5.1   Introduction

Aircraft flight control systems are systems that are used to control the forces of flight, aircraft's direction and attitude. The aim of a flight control system of an aircraft is to maintain a safe operation of the aircraft in flight, so that the desired flight mission can be accomplished even under unexpected conditions. Safety is of serious concern in flight control systems. In this chapter, some Artificial Intelligence (AI) networks are employed in the further mitigation of effects of temperature and noise on the performance of the pitch control system of the AAS. These are Particle Swarm Optimisation (PSO) algorithm and Flower Pollination Algorithm (FPA).

5.2   Particle Swarm Optimisation Algorithm

PSO was initially developed as a tool by Kennedy and Ebenhart in the year 1995 for simulating the flight pattern of birds concerning collision avoidance, velocity matching and flock centring. The desirability of PSO lies in easy implementation, robustness to control parameters and conceptual simplicity. However, setbacks of PSO are the ease in falling into local optimum in high-dimensional space and a low convergence rate in the iterative process (Hemdan *et al*. 2017; Wen *et al*. 2018). In PSO, the particles are evaluated according to the fitness function of the problem to be solved. The particle best position and global best position of the particles are continually updated until the termination criterion loop is met. PSO algorithm uses only primitive mathematical operators which accounts for low computational requirements and the knowledge of good solutions is retained by all particles (Ahmad *et al.,* 2018). The previous best position of particle (P_{id}) and the global best position (P_{gd}) are needed in determining the current position. The best particle and global best positions are determined and updated using Equation (5.1) and Equation (5.2), respectively (Sen, 2017).

$$v_{id}^{n+1} = X(\omega v_{id}^n + c_1 r_1^n (p_{id}^n - x_{id}^n) + c_2 r_2^n (p_{gd}^n - x_{id}^n)) \qquad (5.1)$$

$$x_{id}^{n+1} = x_{id}^n + v_{id}^n \qquad (5.2)$$

where, X = constriction factor

ω = inertia weight

c_1 = cognitive acceleration parameter

c_2 = social acceleration parameter

r_1, r_2 = random number uniformly distributed in the range [0,1]

x_{id} = particle's position

v_{id} = particle's velocity

The flowchart of the PSO algorithm is illustrated in Fig. 5.1 (Bose, 2017) and Fig. 5.2 shows the pseudocode of PSO.
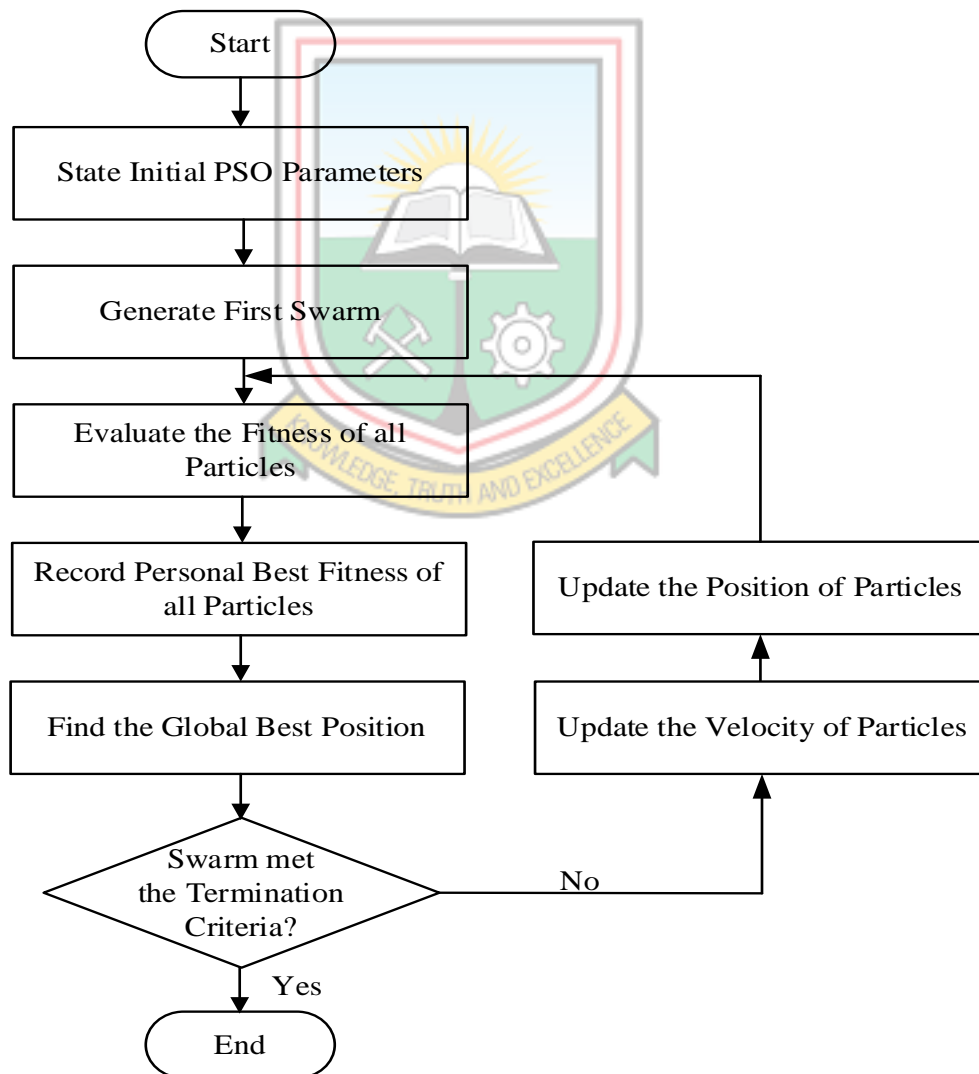
Fig. 5.1 Flowchart of PSO Algorithm

Steps of the flowchart

Step 1: Define the initial parameters for the PSO. For each particle in the swarm, initialise its position and velocity.

Step 2: Evaluate the objective function at each particle position and determine the best function value and the best position.

Step 3: Choose new velocities based on current velocity, individual best position and best position for their neighbours (global).

Step 4: Choose the particles with the best fitness values as the best values for their individual neighbours.

Step 5: If the termination criteria is satisfied, the optimal structure is achieved for further prediction, otherwise, go back to Step 2.

Begin
  for *each particle in the swarm*
   Initialise its position and velocity randomly
  end for
 do
  for *each particle in the swarm*
   Evaluate the fitness function
  if *the objective fitness value is better than the personal best objective fitness value*
   (P_{best}) in history, current fitness value is set as the new personal best (P_{best})
end if
end *for*
  From all the particles or neighbourhood, choose the particle with best fitness value
  as the G_{best}
 for *each particle in the swarm*
  Update the particle velocity
  Update the particle position
end for
until *stopping criteria is satisfied*
end

Fig. 5.2 Pseudocode of Particle Swarm Optimisation Algorithm

5.3 Flower Pollination Algorithm

FPA is a nature-inspired population based algorithm proposed by Xin-She Yang in 2012. The main objective of the FPA is to produce the optimal reproduction of plants by surviving the fittest flowers in the flowering plants. There are over a quarter of a million types of

flowering plants in nature, of which 80% of them are flowering species. The main purpose of a flower is ultimately reproduction via pollination (Yang, 2016). The flower pollination process is associated with the transfer of pollen by using pollinators such as insects, birds and bats. There are two major processes for transferring the pollen, namely, biotic or cross pollination process and abiotic or self pollination process.

Biotic pollination represents 90% of flowering plants, while 10% of pollination takes from abiotic process. In the biotic pollination, pollen is transferred from one flower to the other flower in different plants by a pollinator. Biotic cross-pollination may occur at long distances and they can be considered as a global pollination process with pollinators performing Le'vy flights. On the other hand, abiotic or self-pollination process is a fertilization of one flower from pollen of the same flower or different flower of the same plant. In this type of pollination, wind and diffusion in water help in the pollination of such flowering plants. Abiotic and self-pollination processes are considered as local pollination. Applications of FPA include engineering optimisation problems, Non-linear Programming (NP) hard combinatorial optimisation problem, training of neural networks, manufacturing scheduling and nurse scheduling problem (Abdel-Basset and Shawky, 2019). High quality and efficiency are considered as the merits of FPA whilst the disadvantages are inadequate optimisation precision and poor convergence (Abdel-Baset and Hezam, 2016; Chen and Pi, 2020).
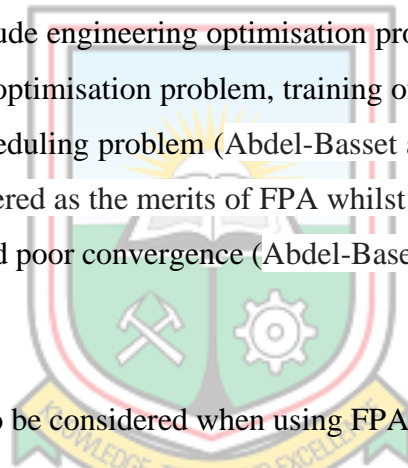
The following steps are to be considered when using FPA.

Step 1: The algorithm starts by setting the initial values of the most important parameters such as the population size, *n*, switch probability, *p* and the maximum number of generations, MGN.

Step 2: The initial population X_i, I = 1,…,n is generated randomly and the fitness function of each solution $f(X_i)$ in the population is evaluated by calculating its corresponding objective function.

Step 3: The following steps are repeated until the termination criterion is satisfied, which is to reach the desired number of generations.

Step 4: The global pollination process is started by generating a random number *r*, where *r* ϵ [0, 1], for each solution X_i.

    a. If *r* < *p*, where *p* is a switch probability, the new solution is generated by a Le'vy distribution as given by equation (5.11).

$$X_i^{t+1} = X_i^{t+1} + L(X_i^t - g*) \tag{5.11}$$

where, L = Le'vy flight, L > 0 and calculated as:

$$L \quad \frac{\lambda\Gamma(\lambda)\sin(\pi\lambda/2)}{\pi}\frac{1}{S^1 + \lambda} \qquad S \quad S_o > 0 \tag{5.12}$$

where, $\Gamma(\lambda)$ = standard gamma function and this distribution is valid for large steps s > 0.

b. Otherwise, the local pollination process is started by generating a random number ϵ, ϵ in [0, 1] as follows:

$$X_i^{t+1} = X_i^t + \epsilon(X_j^t - X_k^t) \tag{5.13}$$

where, X_i^t and X_j^t = pollens (solutions) from the different flowers of the same plant species.

X_i^t and X_j^t = pollens (solutions) from the same species or selected from the same population (local random walk)

c. Evaluate each solution X_i^{t+1} in the population and update the solutions in the population according to their objective values.

d. Rank the solutions and find the current best solution g*.

Step 5: Produce the best found solution so far.

Fig. 5.3 shows the flowchart of FPA and Fig. 5.4 presents the pseudocode of FPA.
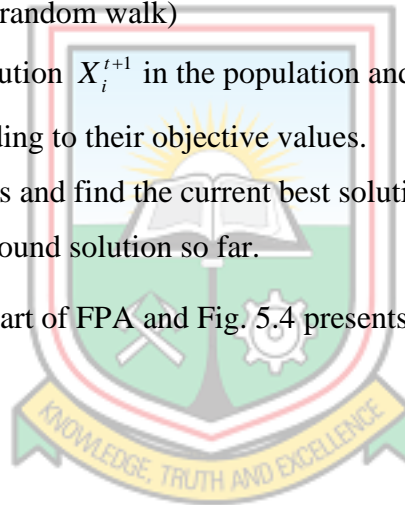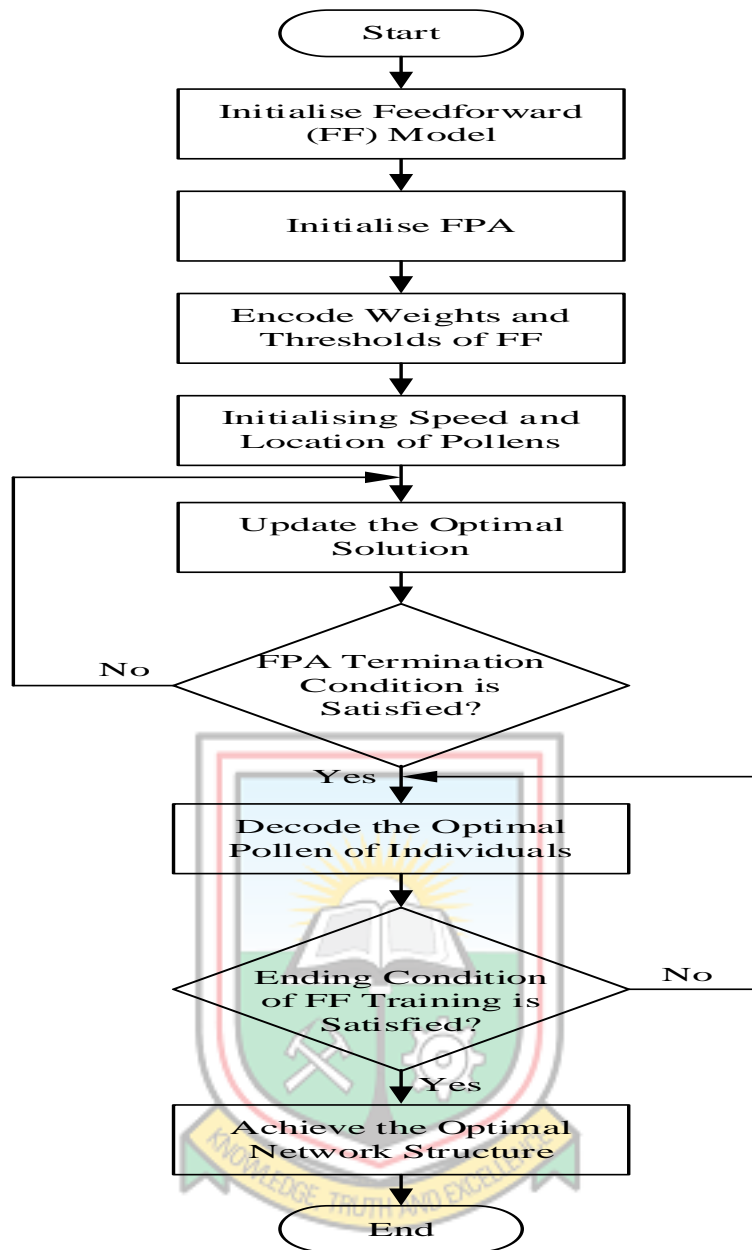
Fig. 5. 3 Flowchart of Flower Pollination Algorithm

Objective min *or* max $f(X), X = (x_1, x_2, ..., x_d)$

Initialise a population of n *flowers/pollen gametes with random solutions*

Find the best solution g∗ *in the initial population*

Define a switch probability p $\in [0,1]$

while $(t < MaxGeneration)$

   for $i = 1 : n$ *(all n flowers in the population)*

    if *rand* < p,

     Draw a (d-dimensional) step vector L which obeys a L´evy distribution

     Global pollination via $X_i^{t+1} = X_i^t + L(g_* - X_i^t)$

  else

Draw ϵ from a uniform distribution in [0,1]

    Randomly choose j and k among all the solutions

    Do local pollination via $X_i^{t+1} = X_i^t + \epsilon(X_j^t - X_k^t)$

end if

    Evaluate new solutions

    If new solutions are better, update them in the population

end for

 Find the current best solution g_*

end while

Fig. 5.4 Pseudocode of the Flower Pollination Algorithm

Steps of the flowchart

Step 1: Initialise feedforward (FF). Set input, hidden and output layers, initial network weight and thresholds.

Step 2: Set the population number, the initial value of variation factor and network learning parameters, the maximum number of iterations and training end condition in FPA.

Step 3: The speed and position of all pollens are initialised and the objective function of each pollen is kept computing until the minimum fitness value is reached.

Step 4: The initial weight and initial threshold in the FF are encoded into individual pollens where each pollen represents the FF structure.

Step 5: A random value *rand* is generated and compared with the conversion probability *p*.

Step 6: If the termination condition of FPA is met, proceed to the next step. Otherwise return to step 5.

Step 7: The optimal pollen individual is decoded and the decoded weights and thresholds are used as connection weight and threshold for FF.

Step 8: If the ending condition of FF training is satisfied, the optimal network structure is thus achieved for further prediction. Otherwise, go back to Step 7.

5.4 Optimal Pitch Control System

Optimality of the pitch control system with regards to the mitigation of temperature and noise effects, lies in use of the PSO and FPA optimisers to optimise the weights of the considered three controllers namely fuzzy-PI, fuzzy-PID and ANFIS. Fig. 5.5 and Fig. 5.6 show a block diagram and optimal representation, respectively, of the pitch control system. The symbols on Fig. 5.5 and Fig. 5.6 are explained as follows:

Ω_θ = angular rate at the input of the MEMS vibratory gyroscope in degrees

T = temperature applied onto the MEMS vibratory gyroscope in $^\circ$C

N_o = noise introduced to the MEMS vibratory gyroscope in dB

θ_{Ref} = reference pitch angle at the output of the MEMS vibratory gyroscope
equivalent in degrees

$V_{\theta_{Ref}}$ = reference voltage at the pitch transmitter output representing the reference
pitch angle of aircraft in volts

V_θ = feedback signal generated by the follow up transmitter representing the actual
pitch angle in volts

V_{e_θ} = error signal representing the difference between reference and actual pitch
angle in volts

U_{θ_c} = signal at the output of the pitch controller in volts

$\theta(s)$ = actual pitch angle in degrees
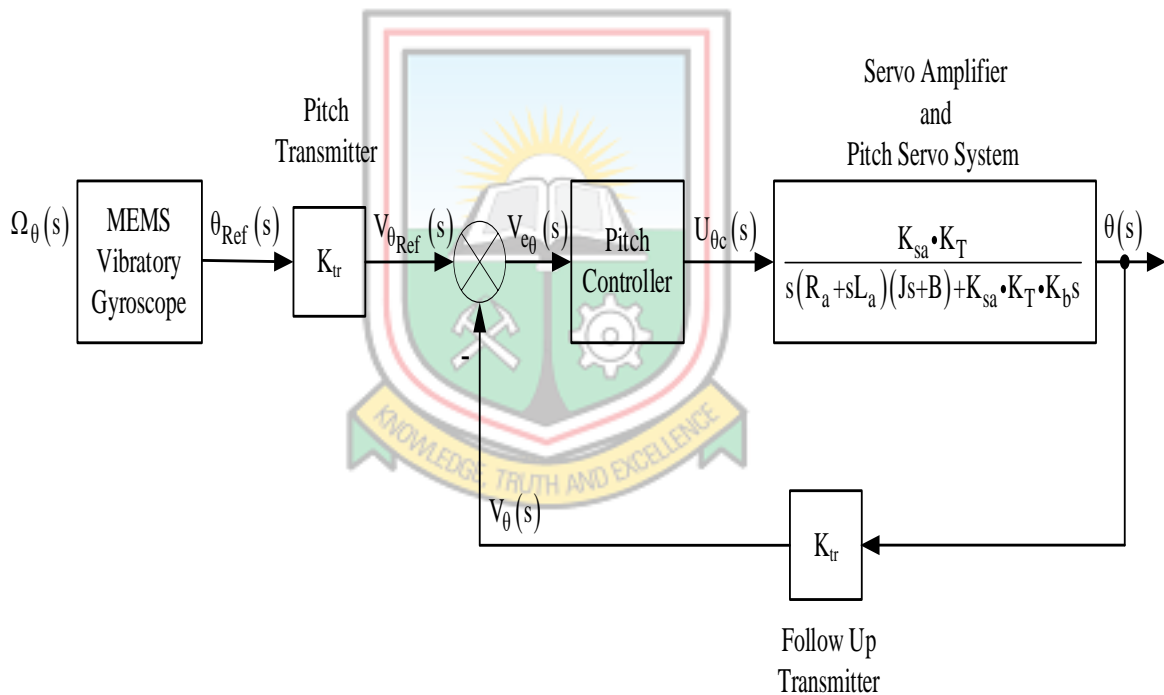
Fig. 5.5 A Block Diagram of the Pitch Control System
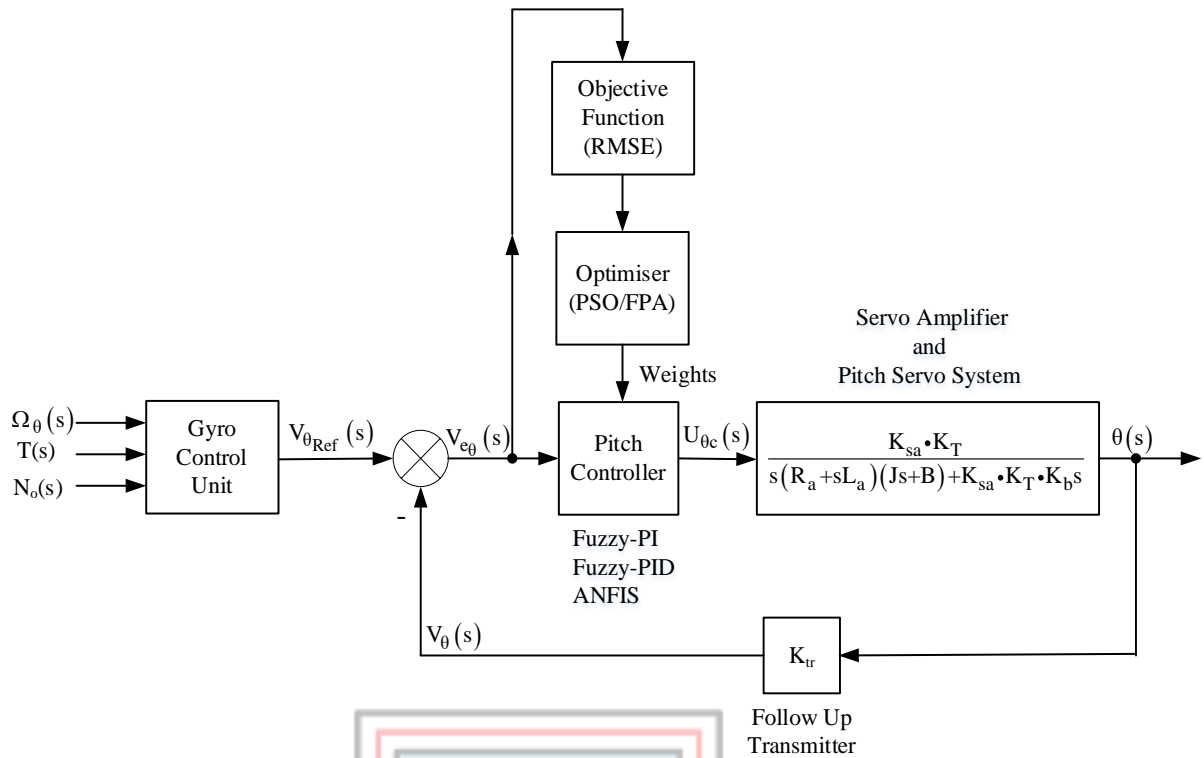
Fig. 5.6 A Representation of the Optimal Pitch Control System

5.5   Computer Simulations

The computer simulations are conducted to find out the ability of each optimiser to suppress the influence of temperature and noise on the output response of the pitch control system. For the scenarios of the simulations, the pitch angles of 12.5 degrees and 33 degrees are considered for each of the optimisers. For the pitch control system of the AAS, the standard noise level is 65 dB (Dongwook *et al*., 2016) and the temperature of the aircraft should not exceed 15 °C (O'Donnell and Bacon, 2015). The performance of the optimisers are however evaluated against these standards of temperature and noise values. The modelled pitch control system of the AAS is optimised in MATLAB Simulink software.

5.6   Results and Discussion

5.5.1   Simulation Results

The performance of the optimisers in suppressing the temperature and noise effects are evaluated by way of responses of the pitch control system with regards to rise time (t_r), overshoot (OS%), settling time (t_s) and slew rate (s_r). The simulation results of the pitch control system of the AAS for 12.5 degrees and 33 degrees are shown in Fig. 5.7 to Fig.

5.16. Also, performance of the pitch control system for 12.5 degrees and 33 degrees with regards to the optimisation algorithms are summarised into Table 5.1 and Table 5.2, respectively.
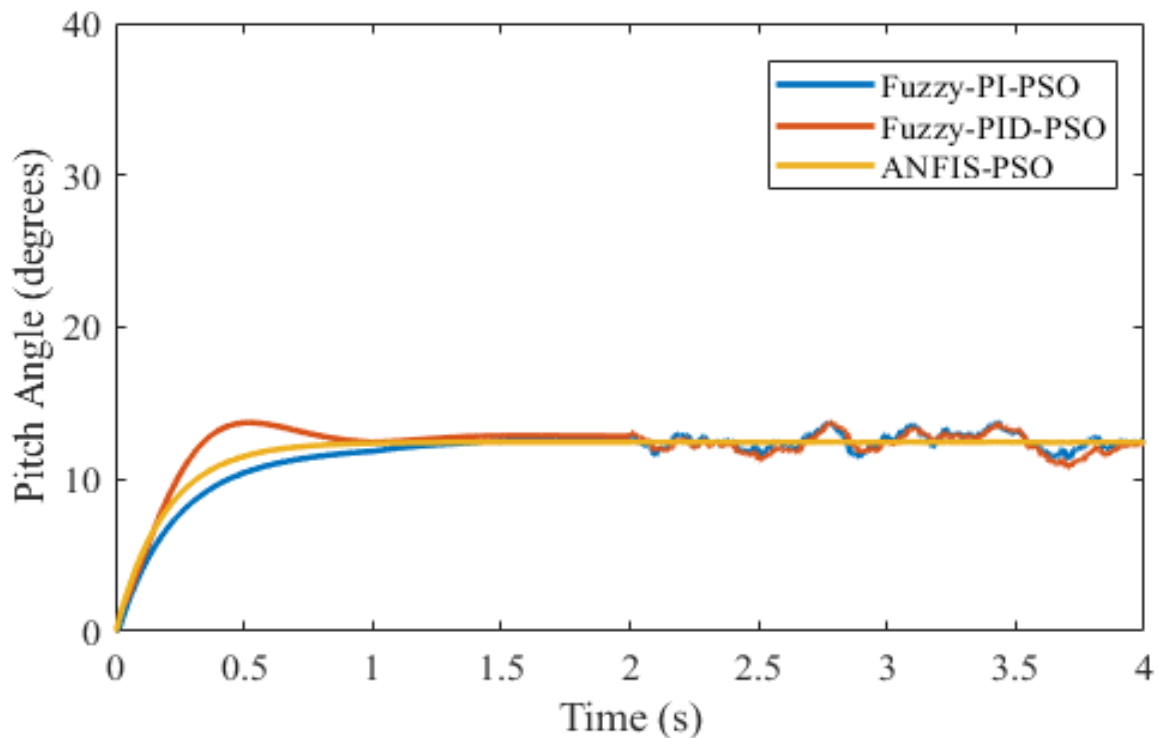
Fig. 5.7 Response of the Pitch Control System to the Pitch Angle of 12.5 degrees with the Introduction of Particle Swarm Optimisation Algorithm
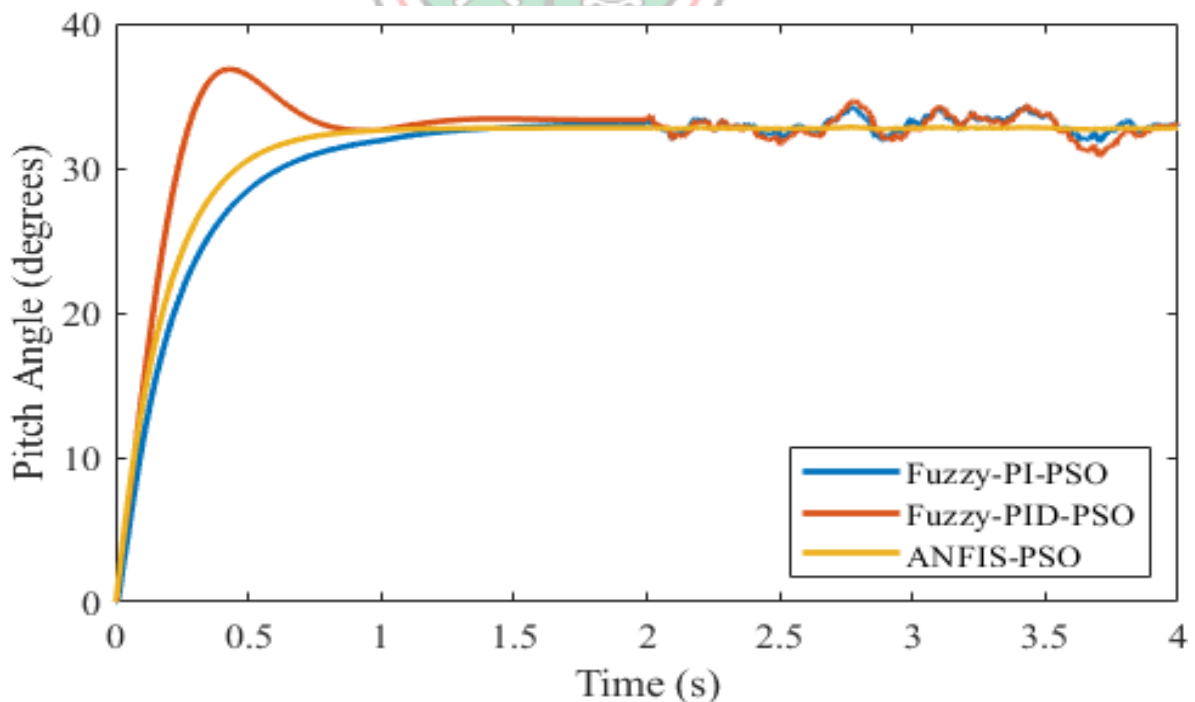
Fig. 5.8 Response of the Pitch Control System to the Pitch Angle of 33 degrees with the Introduction of Particle Swarm Optimisation Algorithm
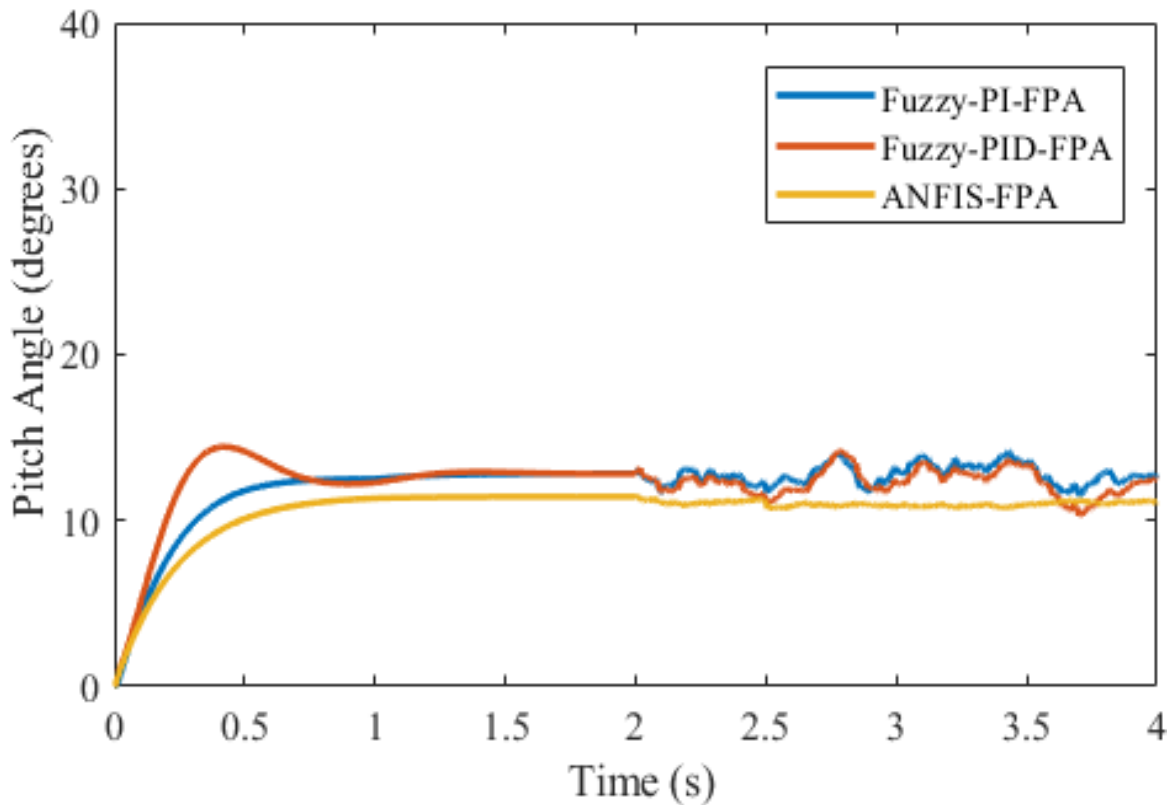
Fig. 5.9 Response of the Pitch Control System to the Pitch Angle of 12.5 degrees with the Introduction of Flower Pollination Algorithm
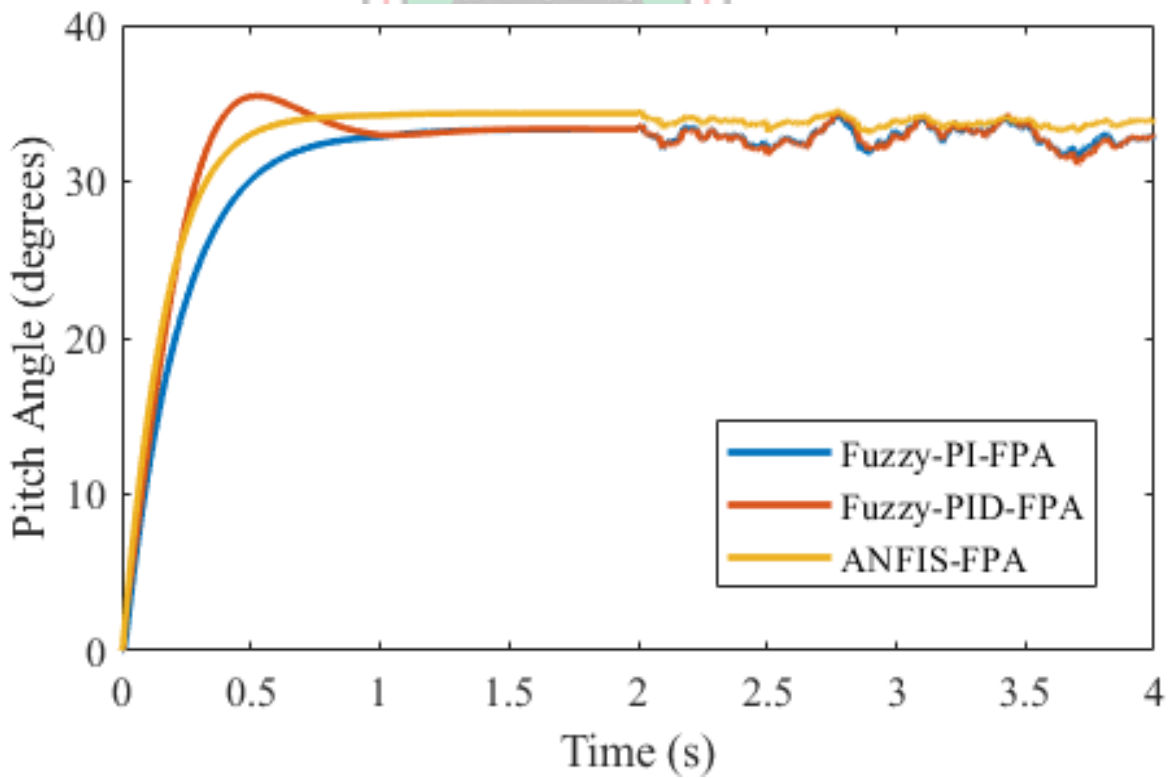
Fig. 5.10 Response of the Pitch Control System to the Pitch Angle of 33 degrees with the Introduction of Flower Pollination Algorithm
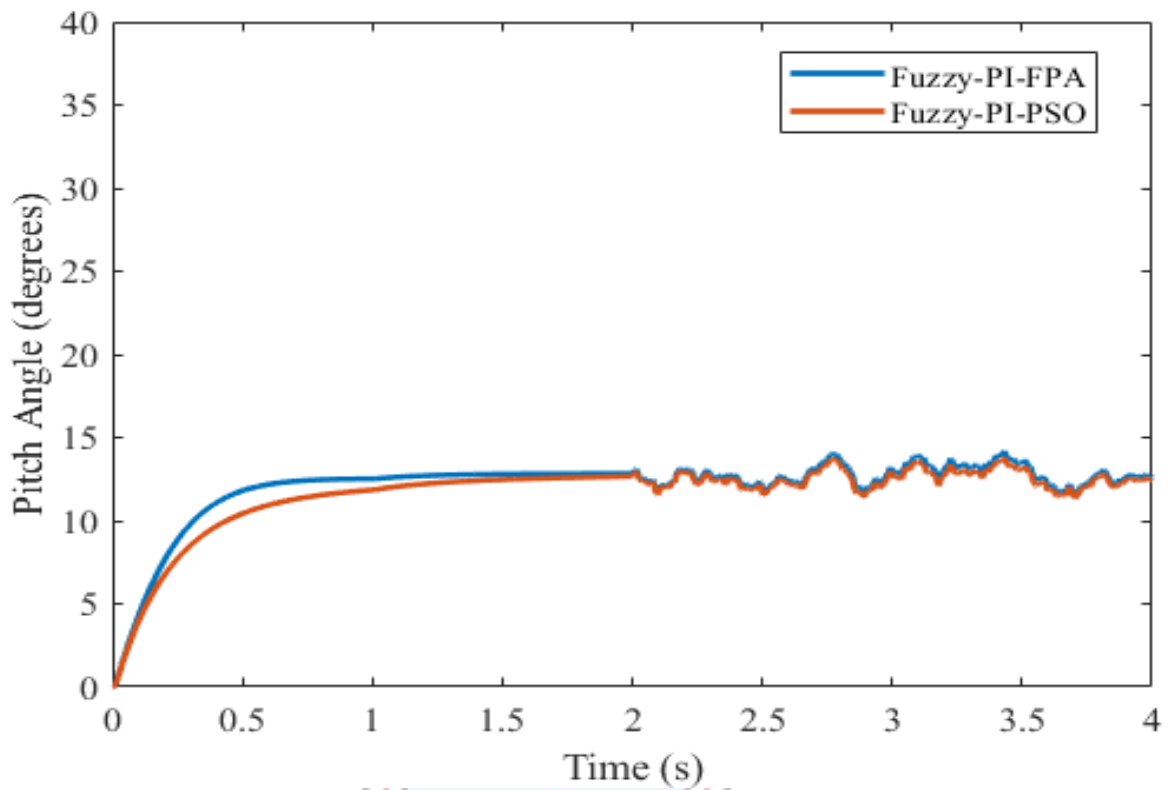
**Fig. 5.11 Response of the Fuzzy-PI Controller-based Pitch Control System to the
Pitch Angle of 12.5 degrees with FPA and PSO Algorithms**
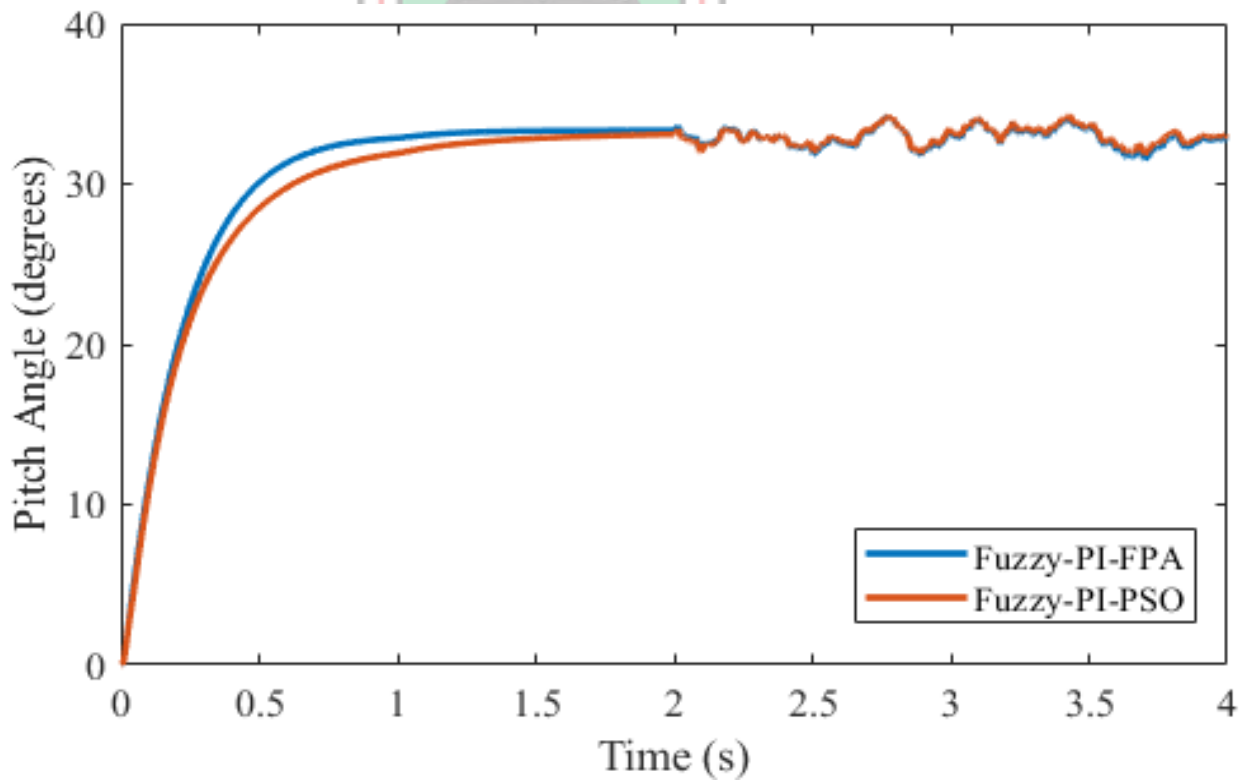
**Fig. 5.12 Response of the Fuzzy-PI Controller-based Pitch Control System to the
Pitch Angle of 33 degrees with FPA and PSO Algorithms**
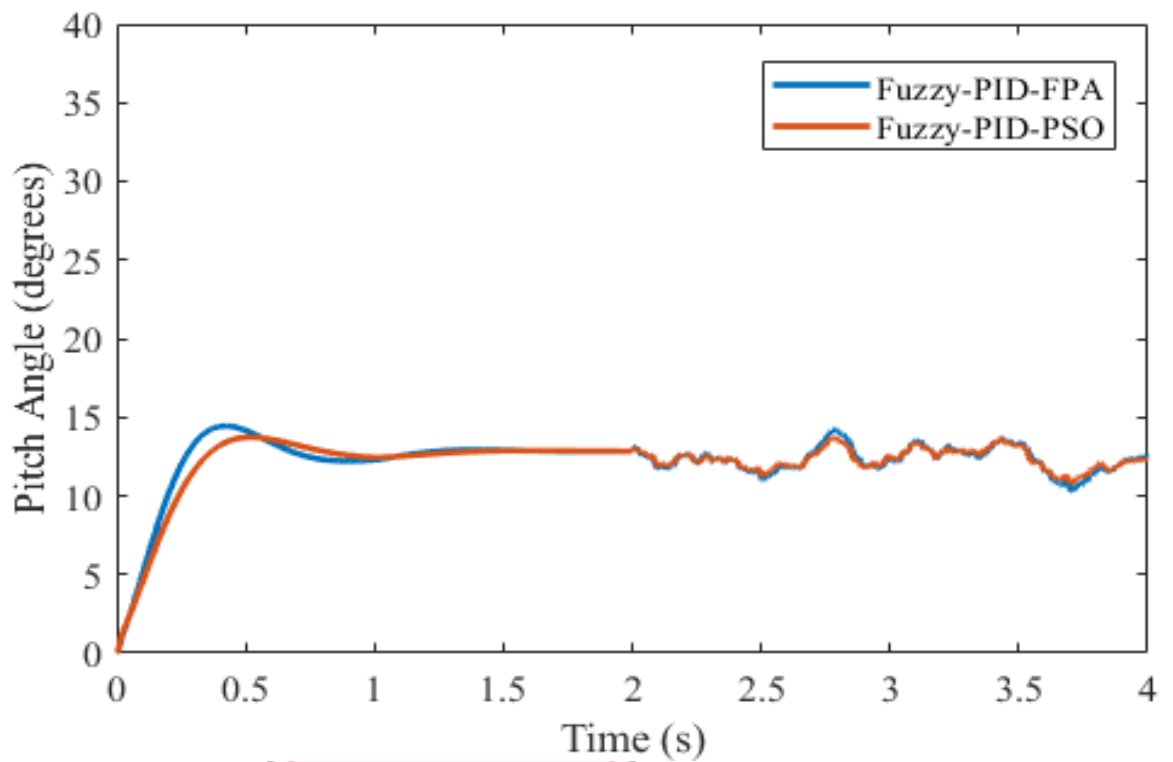
Fig. 5.13 Response of the Fuzzy-PID Controller-based Pitch Control System to the Pitch Angle of 12.5 degrees with FPA and PSO Algorithms
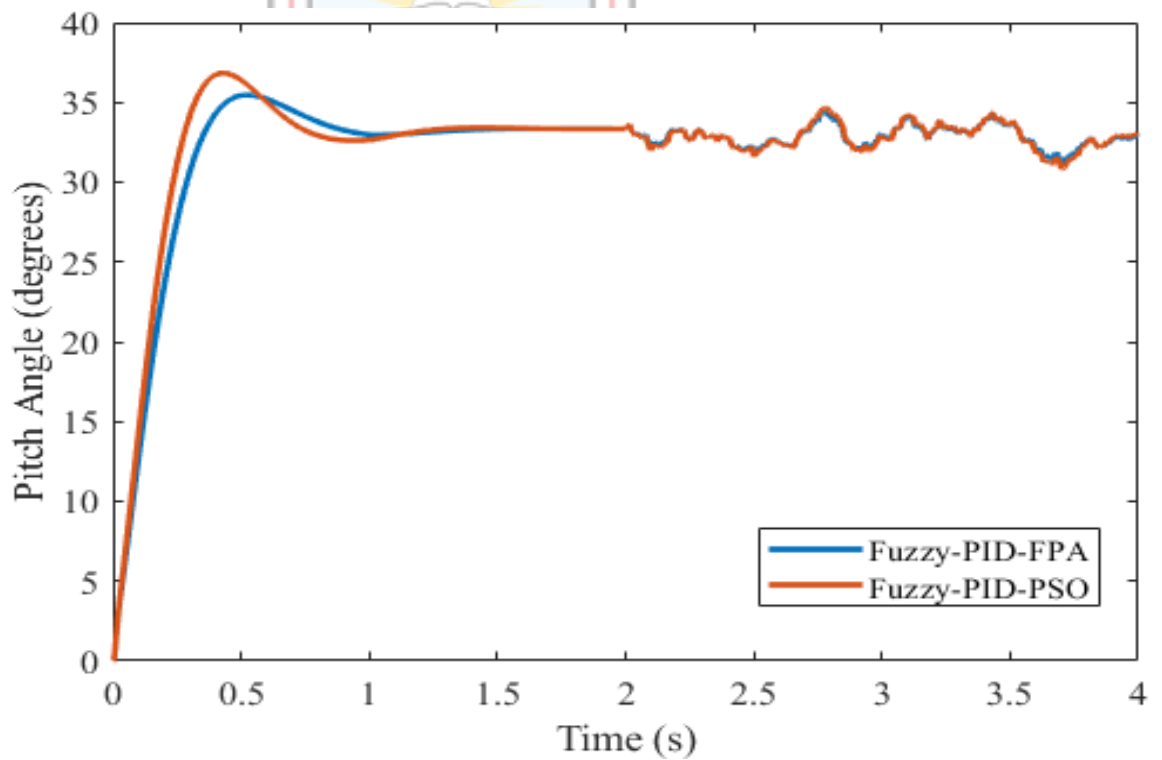
Fig. 5.14 Response of the Fuzzy-PID Controller-based Pitch Control System to the Pitch Angle of 33 degrees with FPA and PSO Algorithms
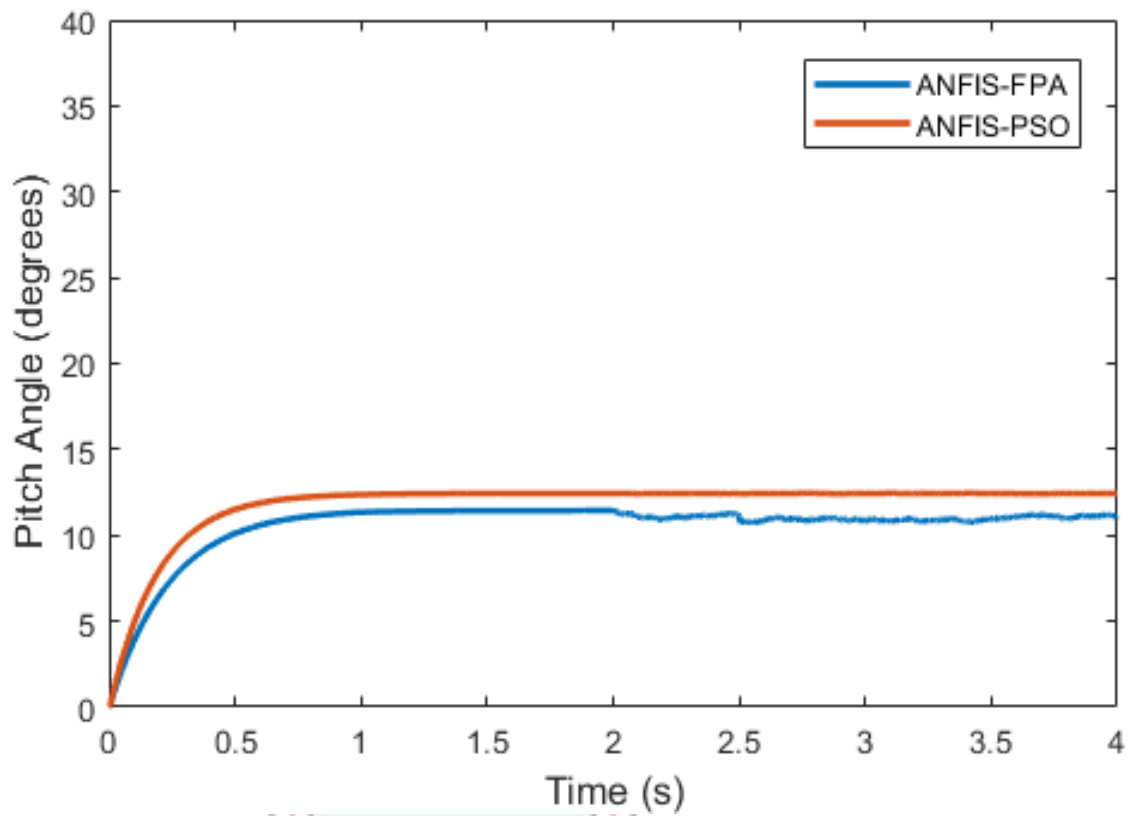
Fig. 5.15 Response of the ANFIS Controller-based Pitch Control System to the Pitch Angle of 12.5 degrees with FPA and PSO Algorithms
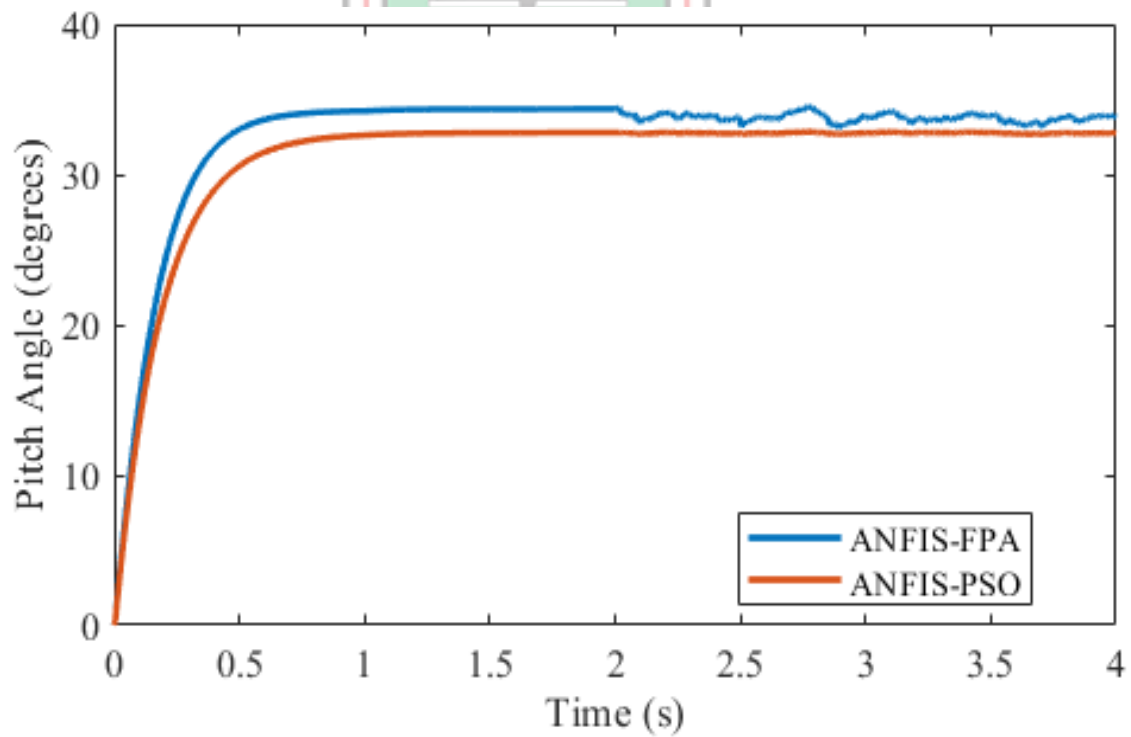
Fig. 5.16 Response of the ANFIS Controller-based Pitch Control System to the Pitch Angle of 33 degrees with FPA and PSO Algorithms

Table 5.1 Performance of the Optimisers at 12.5 dps

SN	Parameter	Optimisation Algorithm					
		Fuzzy-PI-PSO	Fuzzy-PID-PSO	Fuzzy-PI-FPA	Fuzzy-PID-FPA	ANFIS-PSO	ANFIS-FPA
1.	Rise Time (ms)	652.015	274.524	422.441	209.378	415.33	498.153
2.	Overshoot (%)	8.854	6.896	2.223	13.068	0.405	0.505
3.	Settling Time (s)	1.697	1.285	1.301	1.389	1.058	1.347
4.	Slew Rate (/s)	15.241	37.225	24.151	48.558	23.748	18.170
5.	RMSE	2.4218	0.6433	0.6275	0.7748	0.0633	1.4545

Table 5.2 Performance of the Optimisers at 33 dps

SN	Parameter	Optimisation Algorithm					
		Fuzzy-PI-PSO	Fuzzy-PID-PSO	Fuzzy-PI-FPA	Fuzzy-PID-FPA	ANFIS-PSO	ANFIS-FPA
1.	Rise Time (ms)	538.509	211.279	460.893	265.792	399.875	339.310
2.	Overshoot (%)	1.964	10.556	0.827	5.851	0.323	0.104
3.	Settling Time (s)	1.582	1.401	1.362	1.439	1.142	1.281
4.	Slew Rate (/s)	48.408	125.537	57.565	100.334	65.04	80.506
5.	RMSE	0.5262	2.9279	1.7340	2.9580	0.2426	0.9080

5.5.2   Discussion of Simulation Results

From Table 5.1 and Table 5.2, ANFIS-PSO gave better performance in terms of overshoot (0.405% at 12.5 degrees, 0.323% at 33 degrees) and settling time (1.058 sec at 12.5 degrees, 1.142 sec at 33 degrees) and RMSE (0.0633 at 12.5 degrees, 0.2426 at 33 degrees). ANFIS-PSO was followed by ANFIS-FPA, fuzzy-PI-FPA, fuzzy-PID-FPA, fuzzy-PID-PSO and fuzzy-PI-PSO with respect to the overshoot and settling time. However, fuzzy-PI-PSO did better in terms of slew rate (15.241 per sec at 12.5 degrees, 48.408 per sec at 33 degrees) but performed poorly in terms of rise time (652.015 ms at 12.5 degrees, 538.509 ms at 33 degrees). Again, fuzzy-PID-PSO did better in terms of rise time (274.524 ms at 12.5 degrees and 211.279 ms at 33 degrees) but fuzzy-PID- FPA performed better in respect of rise time at 12.5 degrees (209.378 ms). With regards to RMSE after the best performing ANFIS-PSO, the order at 12.5 degrees was fuzzy-PI-FPA, fuzzy-PI-PSO, fuzzy-PID-FPA, ANFIS-FPA and fuzzy-PI-PSO whilst at 33 degrees after the ANFIS-PSO, the order was fuzzy-PI-PSO, ANFIS-FPA, fuzzy-PI-FPA, fuzzy-PID-PSO and fuzzy-PID-FPA. The better performance of the optimised ANFIS controllers with regards to overshoot and settling time is attributable to the learning capability of ANFIS. The better performance of ANFIS-PSO compared to that of ANFIS-FPA could be due to the control parameter robustness ability of PSO. More importantly, ANFIS-PSO capably mitigated the oscillatory effects of

temperature and noise introduced to the pitch control system of the AAS (see Fig. 5.7, Fig. 5.8, Fig. 5.15 and Fig. 5.16). The inability of ANFIS-FPA to effectively reduce the effects as done by ANFIS-PSO could be due to the precision inadequacy of optimisation of FPA.

5.6   Summary

This chapter presented the optimal mitigation of temperature and noise effects of the pitch control system of an AAS. Flowcharts and pseudocodes of PSO and FPA were provided respectively. The results of the pitch control system with the optimised fuzzy-PI, fuzzy-PID and ANFIS controllers showed that ANFIS-PSO performed better in terms of mitigation of temperature and noise effects, overshoot, settling time and RMSE.

CHAPTER 6

CONCLUSIONS AND RECOMMENDATIONS

6.1   Conclusions

This research investigated enhancement of the aircraft pitch control system in an endeavour to mitigate "faults" of MEMS vibratory gyroscopes deployable in AAS. Specifically investigated were the effects of temperature and noise imbibed by the gyroscope as faults on the pitch control system. Oscillations as the resulting influence of temperature and noise were confirmed by the reference angular signal at the output of the MEMS vibratory gyroscope by way of computer simulations at specified pitch angles. Five controllers namely PI, PID, fuzzy-PI, fuzzy-PID and ANFIS were separately deployed to deal with the oscillations. Even though some successes were achieved by them especially the ANFIS, fuzzy-PID and fuzzy-PI controllers, they all left a trail of remnant oscillations that called for use of optimisers. PSO and FPA algorithms were deployed for the optimisation of the three controllers. ANFIS-PSO successfully dealt with the remnant oscillations and gave better performance metrics in terms of overshoot, settling time and RMSE but suffered on rise time at 33 degrees and slew rate at 12.5 degrees. It stands to reason that use of the MEMS vibratory gyroscope in AAS as a new development coupled with deployment of optimised ANFIS controller, enhances control of AAS in terms of gyroscope-related faults mitigation.

6.2   Recommendations

It is recommended that the newly developed, cheaper and small sized MEMS vibratory gyroscopes should be appropriately deployed in AAS for enhanced performance of attitude control of aircraft. Researchers and product developers are encouraged by this research to delve into possible deployment of the MEMS vibratory gyroscope in AAS.

6.3   Research Contributions

The contributions of this research are three fold: Firstly, a maiden investigation of the relatively new MEMS vibratory gyroscope in terms of faults effects of temperature and noise. Secondly, a proposal for use of the MEMS vibratory angular rate sensor-based pitch control system in enhancement of performance of AAS and thirdly, combining PSO with ANFIS for desirable mitigation of temperature and noise effects on the pitch control system of AAS.

6.4   Future Research Directions

Future research directions are as follows:

i.   Laboratory investigation and experimental field testing of MEMS vibratory gyroscope angular rate sensor-based pitch control system should be conducted as an extension of this research.

ii. Similar research should be conducted for a 2-DoF sense, 1-DoF drive MEMS vibratory gyroscope and the research outcome need be compared with the outcome of 1-DoF sense, 2-DoF drive case.

iii. Effects of other "faults" inducing factors such as humidity and random bias instability on the MEMS vibratory gyroscope-based AAS should be investigated.

iv. The roll and yaw control systems of the AAS should be investigated with focus on use of the MEMS vibratory gyroscope.

REFERENCES

Abdel-Baset, M. and Hezam, I. (2016), "A Hybrid Flower Pollination Algorithm for Engineering Optimization Problems", *International Journal of Computer Applications*, New York, USA, pp. 1 – 4.

Abdel-Basset, M. and Shawky, L. A. (2019), "Flower Pollination Algorithm: A Comprehensive Review", *Artificial Intelligence Review*, Vol. 52, No. 4, pp. 33 - 257.

Abdolvand, R., Bahreyni, B., Lee, J. E. Y. and Nabki, F. (2016), "Micromachined resonators", *A review. Micromachines*, Vol. 7, No. 9, pp. 160.

Abrate, S. (2016), "Soft Impacts on Aerospace Structures", *Progress in Aerospace Sciences*, Vol. 81, No. 3, pp. 1 – 17.

Acar, C. and Shkel, A. (2009), MEMS Vibratory Gyroscopes Structural Approaches to Improve Robustness, *Springer*, New York, USA, pp. 83 – 86.

Ahmad, M., Ali, W., Farooq, H., Jamil, M., Ali, M. and Rehman, A. U. (2018), "Solving the Problem of Economic Load Dispatch for a Small Scale Power System Using a Novel Hybrid PSO-GSA Algorithm", *International Symposium on Recent Advances in Electrical Engineering,* Islamabad, Pakistan, pp. 1 - 6.

Akyürek, Ş., Kürkçü, B., Kaynak, Ü. and Kasnakoğlu, C. (2016), "Control Loss Recovery Autopilot Design for Fixed-wing Aircraft" *Proceedings of 6th IFAC Symposium on System Structure and Control,* Istanbul, Turkey, pp. 117 – 123.

Anon. (2015), "Autopilot", *www.wikipedia.org/wiki/Autopilot*. Accessed: August 16, 2018.

Anon. (2016), "Airfoil", *www.wikipedia.org/wiki/Airfoil*. Accessed: August 13, 2018.

Anon. (2017a), "Aircraft", *www.wikipedia.org/wiki/Aircraft*. Accessed: August 6, 2018.

Anon. (2017b), "Aircraft", *www.wikipedia.org/wiki/Aircraft*. Accessed: August 8, 2018.

Anon. (2017c), "Types of Aircraft", *www.britannica.com/technology/airplane/Types-of-Aircraft*. Accessed: August 12, 2018.

Anon. (2017d), "Semiconductor Ring Laser Apparatus" *https://www.google.it/patents/US4405236.* Accessed: October 4, 2017.

Babinsky, H. (2015), "How do Wings Work", *Physics Education*, Vol. 38, No. 6, pp. 493 - 497.

Badick, J. R., Dole, C. E., Lewis, J. E. and Johnson, B. A. (2016), *Flight Theory and Aerodynamics*: *A Practical Guide for Operational Safety*, John Wiley and Sons, Chichester, UK, 3rd edition, 384 pp.

Barman, B., Kanjilal, R. and Mukhopadhyay, A. (2016), "Neuro-Fuzzy Controller Design to Navigate Unmanned Vehicle with Construction of Traffic Rules to avoid Obstacles", *International Journal of Uncertainty, Fuzziness and Knowledge-Based Systems*, Vol. 24, No.03, pp. 433 - 449.

Brandt, S. A. (2011), *Introduction to Aeronautics: A Design Perspective*, American Institute of Aeronautics and Astronautics, Virginia, USA, 3rd edition, 508 pp.

Bose, B. K. (2017), "Artificial Intelligence Techniques in Smart Grid and Renewable Energy Systems", *Proceedings of the IEEE*, Vol. 105, No.11, pp. 62 - 73.

Caliskan, F. and Hacizade, C. (2017), "Sensor and Actuator FDI Applied to an UAV Dynamic Model", *IFAC Proceedings,* Vol. 47, No. 3, pp. 12220 - 12225.

Chen, H. X., Shen, D. K. and Yang, X. (2016), "Effects of Mechanical Properties of Electric Loading System on Surplus Torque", *Chinese Guidance, Navigation and Control Conference*, Nanjing, China, pp. 913 - 917.

Chen, W., Qin, H., Zhang, Y. and Jin, T. (2012), "Accuracy Assessment of Single and Double Difference Models for the Single Epoch GPS Compass", *Advances in Space Research*, Vol. 49, Issue 4, pp. 725 - 738.

Chen, Y. and Pi, D. (2020), "An Innovative Flower Pollination Algorithm for Continuous Optimization Problem", *Applied Mathematical Modelling*, Vol. 83, pp. 237 – 265.

Coban, K., Colpan, C. O. and Karakoc, T. H. (2017), "Application of Thermodynamic Laws on a Military Helicopter Engine", *Advanced Energy Technologies in Aviation*, Vol. 140, No. 16, pp. 1427 – 1436.

Dalldorff, L., Luckner, R. and Reichel, R. (2013), "A Full-Authority Automatic Flight Control System for the Civil Airborne Utility Aircraft S15 – LAPAZ", *Proceedings of the EuroGNC, 2nd CEAS Specialist Conference on Guidance, Navigation and Control*, Delft, Netherlands, pp. 887 - 906.

Debiasi, M. T., Bouremel, Y., Lu, Z. and Ravichandran, V. (2016). "Deformation of the Upper and Lower Surfaces of an Airfoil by Macro Fiber Composite Actuators", *Proceedings of the Applied Aerodynamics Conference*, Jurong West, Singapore, pp. 1 – 9.

Dogruer, T. and Tan, N. (2018), "Design of PI Controller using Optimization Method in Fractional Order Control Systems", *International Federation of Accountants*, Vol. 51, Issue 4, pp. 841 - 846.

Dole, C. E., Lewis, J. E., Badick, J. R., and Johnson, B.A. (2016), *Flight Theory and Aerodynamics: A Practical Guide for Operational Safety*, Wiley-Interscience, New Jersey, USA, 3rd edition, 379 pp.

Dongwook, L., Sanggyu, M. and Dimitri, N. M. (2016), "Aircraft Noise Reduction Technology and Airport Noise Analysis for General Aviation Revitalization", 15th American Institute of Aeronautics and Astronautics Aviation Technology, Integration, and Operations Conference, Dallas, USA, pp. 1 – 17.

Elmajdub, F. A. B. N. and Manish, K. S. (2017), "Modified Six – Degree of Freedom Related to Takeoff and Landing Stages of Aircraft", *Journal of Electrical and Electronics Engineering*, Vol. 12, Issue 5, pp. 1 – 8.

Ewees, A. A. and Elaziz, M. A., (2018), "Improved Adaptive Neuro-Fuzzy Inference System using Gray Wolf Optimization", *Journal of Intelligent Systems*, Vol. 29, No. 1, pp. 924 - 940.

Ewees, A. A., El Aziz, M. A. and Elhoseny, M. (2017), "Social-Spider Optimization Algorithm for Improving ANFIS to Predict Biochar Yield", *8th International Conference on Computing, Communication and Networking Technologies*, Delhi, India, pp. 1 - 6.

Eykeren, L. V., Chu, Q. P. and Mulder, J. A. (2012), "Actuator Fault Detection by Aerodynamic Model Identification", *8th IFAC Symposium on Fault Detection, Supervision and Safety of Technical Processes*, Delft, Netherlands, Vol. 45, Issue 20, pp. 1353 – 1357.

Fallavollita, P., Wang, L., Zou, R., Chen, X., Weidert, S. and Navab, N. (2012), "Closed-form Inverse Kinematics for Interventional C-arm X-ray Imaging with Six Degrees of Freedom: Modelling and Application, *IEEE Transactions on Medical Imaging*, Vol. 31, No. 5, pp. 61 - 69.

Feng, H., Luo, M., Liu, H. and Wu, Z. (2011), "A Knowledge-based and Extensible Aircraft Conceptual Design Environment" *Chinese Journal of Aeronautics*, Vol. 24, Issue 3 pp. 709 – 719.

Feng, H., Lou, W., Wang, D., Zheng, F. and Liao, M. (2018), "System Reliability Analysis of MEMS Gyroscope with Multiple Failure Modes", 10th *International Conference on Modelling, Identification and Control*, Guiyang, China, pp. 1 - 6.

Ferreira, R. B., Baum, D. M., Neto, E. C. P., Martins, M. R., Almeida, J. R., Cugnasca, P. S. and Camargo, J. B. (2018), "A Risk Analysis of Unmanned Aircraft Systems Integration into Non-Segregate Airspace", *International Conference on Unmanned Aircraft System*, Braunschweig, Germany, pp. 42 – 51.

Fontanella, R., Accardo, D., Moriello, R. S. L., Angrisani, L. and De Simone, D. (2018), "MEMS Gyros Temperature Calibration through Artificial Neural Networks", *Sensors and Actuators*, Vol. 279, pp. 553 - 565.

Geliev, A.V., Varyukhin, A. N., Zakharchenko, V. S., Kiselev, I. O. and Zhuravlev, D. I. (2019), "Conceptual Design of an Electric Propulsion System Based on Fuel Cells for an Ultralight Manned Aircraft", *International Conference on Electrotechnical Complexes and Systems,* Ufa, Russia, pp. 1 - 17.

Goupil, P. (2011), "AIRBUS State of the Art and Practices on FDI and FTC in Flight Control System", *Control Engineering Practice*, Vol. 19, No. 6, pp. 524 - 539.

Gu, H., Zhao, B., Zhou, H., Liu, X. and Su, W. (2019), "MEMS Gyroscope Bias Drift Self-Calibration Based on Noise-Suppressed Mode Reversal", *Micromachines*, Vol. 10, No. 12, pp. 1 – 17.

Hakan, C. and Yaralioglu, G. G. (2017). "Analysis of Vibratory Gyroscopes: Drive and Sense Mode Resonance Shift by Coriolis Force", *IEEE Sensors Journal*, Vol. 17, No. 2, pp. 347 – 358.

Hao, S., Zhu, Y., Zhang, C., Feng, J., Chen, W. and Zhang, K. (2019), "A Novel Optimisation Design Method for Multi-degree of Freedom Vibratory Gyroscope", *International Conference of Mechatronics and Automation*, Tianjin, China, pp. 276 – 281.

Hamel, P. G. (2017), "Variable Stability Aircraft and In-Flight Simulators", *In-Flight Simulators and Fly-by-Wire/Light Demonstrators*, Springer, pp. 33 - 71.

Handoyo, S. and Efendi, A. (2019), "Generating of Fuzzy Rule Bases with Gaussian Parameters Optimized via Fuzzy C-Mean and Ordinary Least Square", *International Journal of Recent Technology and Engineering*, Vol. 8, No. 4, pp. 5787 - 5794.

Hemalatha, B. and Kumar, S. (2013), "Design and Simulation of MEMS based Gyroscope", *International Journal of Electrical and Electronics Engineering,* Vol. 5, Issue 6, pp. 23 – 30.

Hess, R. A. (2016) "Fast Simulation in Evaluating Pilot/Aircraft Performance and Handling Qualities", *IFAC Proceedings*, California, USA, Vol. 49, No. 14, pp. 153 – 158.

Hu, Y., Zeng, K., Wang, H., Liang, C., Zhou, Y. and Sun, X. (2018), "A Temperature Compensation Method of Measuring Frequency for Cylindrical Vibratory Gyroscope in Frequency Split Trimming", *Maricopa Advanced Technology Education Center Web of Conferences*, Changsha, China, pp. 1 – 5.

Hu, Z. and Gallacher, B. (2018), "A Mode-Matched Force-Rebalance Control for a MEMS Vibratory Gyroscope", *Sensors and Actuators*, Vol. 273, pp. 1 - 11.

Huajun, G., Ziyang, Z., Xin, L., Ju, J. and Wang, X. (2012), "Automatic Flight Control System Design of Level Change Mode for a Large Aircraft", *International Journal of Advanced Robotic System*, Vol. 10, Issue 96, pp. 1 – 8.

Ivanova, M. S., Nakova, M. M., Ivanov, I. N. and Denishev, K. H. (2013), "Investigation and Analysis of Gyroscope MEMS Design Solutions for Automotive Applications", *Annual Journal of Electronics*, Sozopol, Bulgaria, Vol. 3, No.1, pp. 223 – 225.

Jaiswal, R., Nair, R. C., Yarlagadda, N. K., Senapati, A. A. K. and Mulage, P. (2016), "Adaptive Gyroscope Drift Compensation based on Temporal Noise Modelling", *International Conference on Microelectronics, Computing and Communications,* Bangalore, India, pp. 1 - 5.

Jakab, P. L. (2014), "Vision of a Flying Machine", The Wright Brothers and the Process of Invention, *American Journal of Aeronautics*, Vol. 41, No. 4, pp. 756 -781.

Jiang, F., Zhang, M. and Shao, T. (2018), "Temperature Compensating Model of MEMS Gyro based on Back Propagation Neural Network". *Conference Series: Materials Science and Engineering*, Vol. 382, No. 5, pp. 1 – 7.

Jimoh, O. P., Thando, B. and Tshabalala. (2017), "PI - Based Fault Tolerant Control for Fixed - Wing UAVs Using Control Allocation", *IFAC-Papers Online*, Vol. 50, Issue 2, pp. 181 – 186.

Jinhui, Z. and Jin, J. (2011), "Modelling of Rate Gyroscopes with Consideration of Faults", *6th IFAC Proceedings*, Beijing, China, Vol. 39, Issue 13, pp. 168 – 173.

Karlgaard C. D., Prasad K. and Schoenenberger, M. (2017), "Coupled Inertial Navigation and Flush Air Data Sensing Algorithm for Atmosphere Estimation", *Journal of Spacecraft and Rockets,* Vol. 54, Issue 1, pp. 128 – 140.

Kavitha, S., Daniel, R. J. and Sumangala, K. (2016), "High Performance MEMS Accelerometers for Concrete Structural Health Monitoring Applications and Comparison with Commercial Off-the-shelf Accelerometers", *Mechanical Systems and Signal Processing*, Vol. 66, No. 10, pp. 410 - 424.

Keane, A. J., Sóbester, A. and Scanlan, J. P. (2017), *Small Unmanned Fixed-wing Aircraft Design: A Practical Approach*, Wiley-Interscience, UK, 2nd edition, 496 pp.

Khalil, A. S., Starovoytov, S. V. and Serpokrylov, N.S. (2018), "The Adaptive Neuro-Fuzzy Inference System Application for the Ammonium Removal from Aqueous Solution Predicting by Biochar", *Materials Science Forum*, Vol. 931, pp. 985 - 990.

Krug, B. G. (2016), "Sensing Gyroscopic Properties of Rotating Magnetic Nanoparticles in Solution", *Unpublished PhD Thesis Report*, Western Michigan University, Kalamazoo, USA, 94 pp.

Kumar, A. S. and Dahiya, R. (2016), "Design and Modelling of Controllers for Aircraft Pitch Control Movement", *International Journal of Engineering and Computer Science*, Vol. 5, Issue 11, pp. 198 – 211.

Kumar, S. and Padture, N. P. (2018), "Materials in the Aircraft Industry", In *Metallurgical Design and Industry,* Springer, Rhode Island, USA, 1st edition, 383 pp.

Kwon, H., Seok, S. and Lim, G. (2017), "System Modeling of a MEMS Vibratory Gyroscope and Integration to Circuit Simulation, *Sensors*, Vol. 17, No. 11, pp. 1 - 13.

Laith, M. J. (2018), "Elevator Servo Control System Design of Fighter Aircraft", *MSc Thesis,* University of Mosul, Mosul, Iraq, pp. 25 – 37.

Liang, J., Qiu, A., Zhao, Y., Xia, G. and Shi, Q. (2019), "A Method for Real-Time Suppression of In-Phase Error of Silicon Micro Gyroscopes", *Intraocular Pressure Conference Series: Materials Science and Engineering*, Vol. 677, No. 2, pp. 1 – 8.

Liliang, L., Zhenhua, W. and Shen, Y. (2016), "Fault Diagnosis for Attitude Sensors via a Bank of Extended Kalman Filters", *Proceedings of the 35th Chinese Control Conference*, Chengdu, China, pp. 34 – 38.

Liu, P. and Yan, P. (2017), "A Modified Pseudo Rigid Body Modelling Approach for Compliant Mechanisms with Fixed-guided Beam Flexures", *Mechanical Sciences*, Vol. 8, No. 2, pp. 359 - 368.

Ma, T., Cao, H. and Shen, C. (2020), "A Temperature Error Parallel Processing Model for MEMS Gyroscope based on a Novel Fusion Algorithm", *Electronic*, Vol. 9, No. 3, pp. 1 – 21.

Mcruer, D. T., Graham, D. and Ashkenas, I. (2014), *Aircraft Dynamics and Control,* Princeton University Press, New Jersey, 3rd edition, 740 pp.

Minoura, K., Fukamizu, T. and Kanko, Y. (2009), "High Response Control System and Diagnosis System for Servo Valve", *IHI Engineering Review*, Vol. 42, No. 1, pp. 42 – 49.

Minotti, P., Dellea, S., Mussi, G., Bonfanti, A., Facchinetti, S., Tocchio, A., Zega, V., Comi, C., Lacaita, A. L. and Langfelder, G. (2017), "High Scale-Factor Stability Frequency-Modulated MEMS Gyroscope: 3-Axis Sensor and Integrated Electronics Design", *Transactions on Industrial Electronics*, Vol. 65, No. 6, pp. 40 - 50.

Narasimhulu, N., Pedamuthevi, V. and Krishna, S. J. (2018), "Natural Frequency Analysis of Helicopter Rotor Blades", *International Journal of Intellectual Advancements and Research in Engineering Computations*, Vol. 6, Issue 4, pp. 2599 – 2605.

Nashat, S. E. D., AbdelRassoul, R. and El Bary, A. E. M. A. (2018), "Design and Simulation of Radio Frequency MEMS Comb Drive with Ultra-low Pull-in Voltage and Maximum Displacement", *Microsystem Technologies*, Vol. 24, No. 8, pp. 43 - 53.

Navidi, N., Landry Jr, R., Cheng, J. and Gingras, D. (2016), "A New Technique for Integrating MEMS-based Low-cost IMU and GPS in Vehicular Navigation", *Journal of Sensors*, Vol. 1, No. 1, pp. 1 – 17.

O'Donnell, K. and Bacon, J. (2015), "Temperature-Controlled Transport Operations by Road and by Air", *World Health Organisation*, Geneva, Switzerland, 34 pp.

Palaniyappan, T. K., Yadav, V., Tayal, V. K. and Choudekar, P., (2018), "PID Control Design for a Temperature Control System", *International Conference on Power Energy, Environment and Intelligent Control*, Greater Noida, India, pp. 632 - 637.

Passaro, M. N. V., Cuccovillo, A., Vaiani, L., Carlo, M. and Campanella, C. E. (2017), "Gyroscope Technology and Applications", *A Review in the Industrial Perspective*, Vol. 17, No. 10, pp. 5 – 22.

Patel, C. and McCluskey, P., (2016), "Performance of MEMS Vibratory Gyroscopes in Harsh Environments", *8th International Conference and Exhibition on Device Packaging*, Maryland, USA, pp. 1 – 10.

Peck, B. C., Allen, G. and Grassey, T. B. (2015), "Air and Space Power", *Journal of Air and Space Power.* Vol. 29, No. 5, pp. 10 - 12.

Peixoto, T. F., Daniel, G. B. and Cavalca, K. L. (2017), "Experimental Estimation of Equivalent Damping Coefficient of Thrust Bearings", *Proceedings of the International Symposium on Dynamic Problems of Mechanics*, Campinas, Brazil, pp. 17 - 29.

Perelmuter, V. M. (2015), "Electrotechnical Systems", *Simulation with Simulink and SimPowerSystem*, CRC Press, Florida, USA, 1st edition, 441 pp.

Petrescu, R. V., Aversa, R., Akash, B., Corchado, J., Berto, F., Apicella, A. and Petrescu, F. I. (2017), "Some Special Aircraft", *Journal of Aircraft and Spacecraft Technology*, Vol. 1, No. 3, pp. 89 – 102.

Poulad, M. E., Naylor, D. and Oosthiuzen, P. H. (2011), "Measurement of Time Average Turbulent Free Convection in a Tall Enclosure Using Interferometry", *Journal of Heat*, Vol. 133, No. 4, pp. 1 - 8.

Prentice, B. E., Beilock, R. E., Phillips, A. J. and Thomson, J. (2010), "The Rebirth of Airships", *Journal of the Transportation Research Forum*, Vol. 44, No. 1, pp. 1- 5.

Powell, J. (2017), "Hardware Design for an Electro-mechanical Bicycle Simulator in an Immersive Virtual Reality Environment", *Unpublished MSc Thesis Report*, University of Iowa, Iowa City, USA, 55 pp.

Pyrhonen, J., Hrabovcova, V. and Semken, R. S. (2016), *Electrical Machine Drives Control*, *An introduction*, 1st edition, John Wiley and Sons, West Sussex, United Kingdom, 527 pp.

Qu, Q., Wang, W., Liu, P. and Agarwal, R. K. (2015), "Airfoil Aerodynamics in Ground Effect for Wide Range of Angles of Attack", *Journal of Aviation*, Vol. 53, No. 4, pp. 1048 – 1061.

Radhakrishna, V., Kumar, P. V., Aljawarneh, S. A. and Janaki, V. (2017), "Design and Analysis of a Novel Temporal Dissimilarity Measure using Gaussian Membership Function", *International Conference on E*ngineering, Monastir, Tunisia, pp. 1 - 5.

Rafiee, P., Khatibi, G. and Zehetbauer, M. (2017), "A Review of the Most Important Failure, Reliability and Nonlinearity Aspects in the Development of Microelectromechanical Systems (MEMS)", *Microelectronics International*, Vol. 34, No. 1, pp. 9 – 21.

Ramesh, P., Jahnavi, W. V. and Kumaraswamy, I. (2012), "Stability Analysis and Root Locus for Three Axis Autopilot Controlled Airplane Using Time and Frequency Domain Responses", *International Journal of Engineering Research and Applications,* Vol. 2, Issue 2, pp. 356 – 360.

Ribeiro, L. R. and Oliveira, N. M. F. (2010), "UAV Autopilot Controllers Test Platform Using Matlab/Simulink and X-Plane", *In Frontiers in Education Conference,* IEEE, pp. S2H - 1.

Rout, M. K., Sain, D., Swain, S. K. and Mishra, S. K. (2016), "PID Controller Design for Cruise Control System using Genetic Algorithm", International Conference on

Electrical, Electronics, and Optimization Techniques, Chennai, India, pp. 4170 – 4173.

Saeed, A. S., Younes, A. B., Islam, S., Dias, J., Seneviratne, L. and Cai, G. (2015), "A Review on the Platform Design, Dynamic Modelling and Control of Hybrid Unmanned Aerial Vehicles", *Proceedings of Unmanned Aircraft Systems International Conference,* Denver, USA, pp. 806 - 815.

Sarruda, A. J. (2011), "Determination of the Shelf Life of MEMS Navigation-grade Sensors through Use of Accelerated Aging Principles", *USA Research, Development and Engineering Command*, pp. 1 – 20.

Sarter, N. B., Mumaw, R. J. and Wickens, C. D. (2015), "Pilots' Monitoring Strategies and Performance on Automated Flight Decks: An Empirical Study Combining Behavioral and Eye-Tracking Data", Vol. 49, Issue 3, pp. 347 - 357.

Schade, N., Eliasson, P., Burg, W. J. and von Geyr, H. F. (2016), "CFD Prediction of Maximum Lift Effects on Realistic High-Lift-Commercial-Aircraft-Configurations", *Proceedings of the 25th Conference of Applied Aerodynamics*, Braunschweig, Germany, pp. 1 – 16.

Shen, C., Li, J., Zhang, X., Shi, Y., Tang, J., Cao, H. and Liu, J. (2016), "A Noise Reduction Method for Dual-Mass Micro-Electromechanical Gyroscopes Based on Sample Entropy Empirical Mode Decomposition and Time-Frequency Peak Filtering", *Sensors*, Vol. 16, No. 6, pp. 1 - 14.

Singh, S. and Murthy, T. R. (2015), "Simulation of Sensor Failure Accommodation in Flight Control System of Transport Aircraft: A Modular Approach", *World Journal of Modelling and Simulation*, Vol. 11, No.1, pp. 55 - 68.

Stroe, G., Andrei, I. C. and Salaoru, T. A. (2017), "Design of Air Traffic Control Operation System", *Proceedings of the 5th International Workshop on Numerical Modelling in Aerospace Sciences*, Bucharest, Romania, No.3, pp. 1 - 15.

Sun, H. and Xie, H. (2017), "Interface Circuits for Capacitive MEMS Gyroscopes", *Fundamental Technology and Applications*, 161 pp.

Takala, J., Kirkko-Jaakkola, M. and Collin, J. (2012), "Bias Prediction for MEMS Gyroscopes", *Proceeding of IEEE*, Vol. 12, No. 6, pp. 2157 – 2163.

Tang, Q. J., Wang, X. J., Yang, Q. P. and Liu, C. Z. (2013), "Static Temperature Analysis and Compensation of MEMS Gyroscopes", *International Journal of Metrology and Quality Engineering*, Vol. 4, No. 3, pp. 209 - 214.

Ting, D. K. and Jalal Ahamed, M. (2018), "Modeling of Structural and Environmental Effects on Microelectromechanical Vibratory Gyroscopes", *Proceedings of Mechanical Engineering International Congress*, Toronto, Canada, pp. 1 – 5.

Tkalich, V. L., Labkovskaia, R. I., Pirozhnikova, O. I., Kalinkina, M. E. and Kozlov, A. S. (2018), "Analysis of Errors in Micromechanical Devices", *International Scientific-Technical Conference on Actual Problems of Electronics Instrument Engineering*, St. Petersburg, Russia, pp. 272 - 276.

Tomayko, J. E. (2017), Computer Take Flight: A History of NASA's Pioneering Digital Fly-by-Wire Project, *NASA History Series*, Vol. 6, No. 2, pp. 57 – 69.

Tonti, J. (2014), "Development of a Flight Dynamics Model of a Flying Wing Configuration", *MSc Thesis*, Sapienza University di Roma, Rome, Italy, pp. 28 – 35.

Torabi, A., Ahari, A. A., Karsaz, A and Kazemi, S. H., (2018), "Intelligent Pitch Controller Identificacion and Design", *Journal of Mathematics and Computer science*, Vol. 2, No. 3, pp. 113 - 127.

Toyoda, K., Kwak, D., Noguchi, M. and Rinoie, K. (2015), "Aerodynamic Interference caused by the Inboard Leading-edge Flap on the Outboard Area of the Cranked Arrow Wing", *Procedia Engineering*, Vol. 99, pp. 42 - 46.

Uhlig, D., Bhamidipti, K. and Neogi, N. (2006), "Safety and Reliability within Unmanned Area Vehicle Construction", *Proceedings of the 25th Digital Avionics Systems Conference*, Hamburg, Germany, pp. 1 – 9.

Valadeiro, J., Cardoso, S., Macedo, R., Guedes, A., Gaspar, J. and Freitas, P. (2016), "Hybrid Integration of Magnetoresistive Sensors with MEMS as a Strategy to Detect Ultra-Low Magnetic Fields", *Micromachines*, Vol. 7, No. 5, pp. 1 - 20.

Verma, P., Shekhar, C., Arya, S. K. and Gopal, R. (2015), "New Design Architecture of a 3-DoF Vibratory Gyroscope with Robust Drive Operation Mode and Implementation", *Microsystem Technologies*, Vol. 21, No. 10, pp. 175 - 185.

Villani, E. and Miyagi, P. E. (2006), "A Hybrid Approach for Safety Analysis of Aircraft Systems" *Proceedings of 2nd Conference on Analysis and Design of Hybrid Systems*, São Paulo, Brazil, pp. 389 – 394.

Von Braitn, W. (2014), "Putting it all Together: Conceptual Aircraft Design", In *Introduction to Aeronautics*, John Wiley and Sons, Chichester, UK, 1st edition, pp. 379 - 386.

Wang, Y., Palacios, R. and Wynn, A. (2015), "A Method for Normal-Mode-based Model Reduction in Nonlinear Dynamics of Slender Structures", *Computers and Structures*, Vol. 159, No. 3, pp. 26 - 40.

Wang, W., Lv, X. and Xu, D. (2014), "Design of Multi-degree-of-freedom Micromachined Vibratory Gyroscope with Double Sense-Modes", *Measurement*, Vol. 58, pp. 6 - 11.

Wargo, C. A., Church, G. C., Glaneueski, J. and Strout, M. (2014), "Unmanned Aircraft Systems Research and Future Analysis", *Proceedings of* the *IEEE Aerospace Conference*, Virginia, USA, pp. 1 - 16.

Wen, C., Liu, C., Zhang, H. and Wang, H. (2018), "An Improved Particle Swarm Optimization with Gaussian Disturbance", *Proceedings of the 2ⁿᵈ International Conference on Electronic Information Technology and Computer Engineering*, Hubei, China, pp. 1 – 4.

Wen, Z., Zhi, Z., Qidan, Z. and Shiyue, X. (2009), "Dynamic Model of Carrier-based Aircraft Landing Gears Landed on Dynamic Deck", *Chinese Journal of Aeronautics*, Vol. 22, No. 12, pp. 371 – 379.

Xie, H. and Fedder, K. G. (2016), "Integrated Microelectromechanical Gyroscope", *Journal of Aerospace Engineering*, Vol. 16, No. 2, pp. 68 – 74.

Xing, H., Hou, B., Lin, Z. and Guo, M. (2017), "Modeling and Compensation of Random Drift of MEMS Gyroscopes Based on Least Squares Support Vector Machine Optimized by Chaotic Particle Swarm Optimization", *Sensors*, Vol. 17, No. 10, pp. 1 – 15.

Yan, Q., Zhang, F. and Zhang, W. (2012), "A Micro-Machined Gyroscope for Rotating Aircraft", *Sensors*, Vol. 12, No. 7, pp. 24 – 28.

Yang, X. S. (2016), "Flower Pollination Algorithm for Global Optimisation", *International Conference on Unconventional Computing and Natural Computation*", Heidelberg, Berlin, pp. 240 - 249.

Younes, A. B., Saeed, A. S., Islam, S., Dias, J., Seneviratne, L. and Cai, G. (2015), "A Review on the Platform Design, Dynamic Modelling and Control of Hybrid UAVs", *Proceedings of the International Conference on Unmanned Aircraft Systems,* Denver, USA, pp. 806 - 815.

Young, I. I. and Aaron, M. (2015), "Saturable Reactor for Power Flow Control in Electric Transmission Systems: Modelling and System Impact Study, *Unpublished PhD Thesis Report,* University of Tennessee, Knoxville, USA, 183 pp.

Zeitlin, V. (2016), "Understanding Inertial Instability on the F-Plane with Complete Coriolis Force", *Proceedings of the International Symposium on Stratified Flows,* Vol. 1, No. 1, pp. 1 – 8.

Zhanshe, G. Fucheng, C. Boyu, L. Le, C. Chao, L. and Ke, S. (2015), "Research Development of Silicon MEMS Gyroscopes" *Micro Systems Technology*, Vol. 21, Issue 10, pp. 2053 – 2066.

Zhiqiang, G. and Zheng, Q. (2011), "Disturbance Rejection in MEMS Gyroscope: Problems and Solutions", *Proceedings of the 30th Chinese Control Conference*, Yantai, China, pp. 6334 – 6339.

Zhou, J., Xiao, Q., Xu, D., Ouyang, H. and Li, Y. (2017), "A Novel Quasi-zero-stiffness Strut and its Applications in Six-degree-of-freedom Vibration Isolation Platform", *Sound and Vibration*, Vol. 394, pp. 59 - 74.

Zhou, W., Chen, L., Yu, H., Peng, B. and Chen, Y. (2016), "Sensitivity Jump of Micro Accelerometer Induced by Micro-fabrication Defects of Micro Folded Beams", *Measurement Science Review*, Vol. 16, No. 4, pp. 228 - 234.

APPENDIX

M-FILE CODES IN MATLAB/SIMULINK SOFTWARE

Create Initial FIS
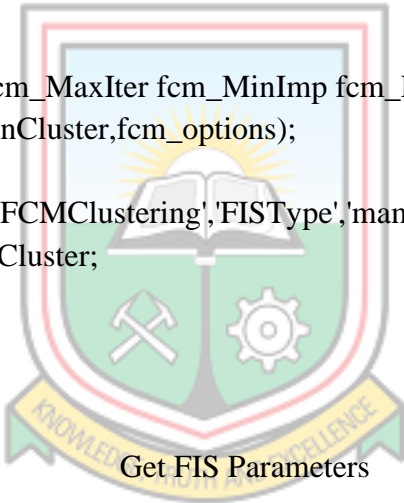
```
function fis=CreateInitialFIS(data,nCluster)

    if ~exist('nCluster','var')
        nCluster='auto';
    end

    x=data.TrainInputs;
    t=data.TrainTargets;

    fcm_U=2;
    fcm_MaxIter=100;
    fcm_MinImp=1e-5;
    fcm_Display=false;
    fcm_options=[fcm_U fcm_MaxIter fcm_MinImp fcm_Display];
    fis=genfis3(x,t,'sugeno',nCluster,fcm_options);

%     opt = genfisOptions('FCMClustering','FISType','mamdani');
%     opt.NumClusters = nCluster;
%     opt.Verbose = 0;
%     fis=genfis(x,t,opt);
end
```

Get FIS Parameters

```
function p=GetFISParams(fis)

    p=[];

    nInput=numel(fis.input);
    for i=1:nInput
        nMF=numel(fis.input(i).mf);
        for j=1:nMF
            p=[p fis.input(i).mf(j).params];
        end
    end

    nOutput=numel(fis.output);
    for i=1:nOutput
        nMF=numel(fis.output(i).mf);
        for j=1:nMF
```

```
      p=[p fis.output(i).mf(j).params];
    end
  end

end
```

Set FIS Parameters

```
function fis=SetFISParams(fis,p)

  nInput=numel(fis.input);
  for i=1:nInput
    nMF=numel(fis.input(i).mf);
    for j=1:nMF
      k=numel(fis.input(i).mf(j).params);
      fis.input(i).mf(j).params=p(1:k);
      p(1:k)=[];
    end
  end

  nOutput=numel(fis.output);
  for i=1:nOutput
    nMF=numel(fis.output(i).mf);
    for j=1:nMF
      k=numel(fis.output(i).mf(j).params);
      fis.output(i).mf(j).params=p(1:k);
      p(1:k)=[];
    end
  end

end
```
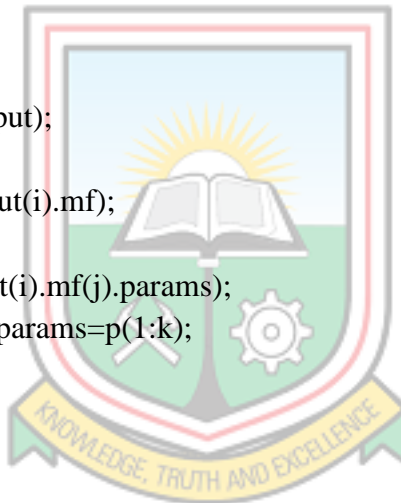
Train FIS Cost

```
function [z, out]=TrainFISCost(x,fis,data)

  MinAbs=1e-5;
  if any(abs(x)<MinAbs)
    S=(abs(x)<MinAbs);
    x(S)=MinAbs.*sign(x(S));
  end

  p0=GetFISParams(fis);

  p=x.*p0;

  fis=SetFISParams(fis,p);
```

```matlab
    x=data.TrainInputs;
    t=data.TrainTargets;
    y=evalfis(x,fis);

    e=t-y;

    MSE=mean(e(:).^2);
    RMSE=sqrt(MSE);

    z=RMSE;

    out.fis=fis;
    %out.y=y;
    %out.e=e;
    out.MSE=MSE;
    out.RMSE=RMSE;

end


function data=LoadData()

    data=load('anfis12_5');
    Input=data.input;
    Target=data.target;
    Target=Target(:,1);

    nSample=size(Input,1);

    % Shuffle Data
    S=randperm(nSample);
    Input=Input(S,:);
    Target=Target(S,:);

    % Train Data
    pTrain=0.9;
    nTrain=round(pTrain*nSample);
    TrainInputs=Input(1:nTrain,:);
    TrainTargets=Target(1:nTrain,:);

    % Test Data
    TestInputs=Input(nTrain+1:end,:);
    TestTargets=Target(nTrain+1:end,:);
```

```matlab
    % Export
    data.TrainInputs=TrainInputs;
    data.TrainTargets=TrainTargets;
    data.TestInputs=TestInputs;
    data.TestTargets=TestTargets;

end
```

Main

```matlab
clc;
clear;
close all;

%% Load Data

data=LoadData();

%% Generate Basic FIS

fis=CreateInitialFIS(data,5); %changed to use original fis
%fisdata=load('fpifis');
%fis=fisdata.FuzzyPI;
%% Train Using PSO

Options = {'Genetic Algorithm', 'Particle Swarm Optimization', 'Flower Pollination'};

[Selection, Ok] = listdlg('PromptString', 'Select training method for ANFIS:', ...
                'SelectionMode', 'single', ...
                'ListString', Options);

pause(0.01);

if Ok==0
    return;
end

switch Selection
    case 1, fis=TrainAnfisUsingGA(fis,data);
    case 2, fis=TrainAnfisUsingPSO(fis,data);
    case 3, fis=TrainAnfisUsingFPA(fis,data);
end

%% Results
```

```matlab
% Train Data
TrainOutputs=evalfis(data.TrainInputs,fis);
PlotResults(data.TrainTargets,TrainOutputs,'Train Data');

% Test Data
TestOutputs=evalfis(data.TestInputs,fis);
PlotResults(data.TestTargets,TestOutputs,'Test Data');
```

Results

```matlab
function PlotResults(Target, Outputs, Name)

    figure;

    Errors=Target-Outputs;

    MSE=mean(Errors.^2);
    RMSE=sqrt(MSE);

    error_mean=mean(Errors);
    error_std=std(Errors);

    subplot(2,2,[1 2]);
    plot(Target,'k');
    hold on;
    plot(Outputs,'r');
    legend('Target','Output');
    title(Name);
    xlabel('Sample Index');
    grid on;

    subplot(2,2,3);
    plot(Errors);
    legend('Error');
    title(['MSE = ' num2str(MSE) ', RMSE = ' num2str(RMSE)]);
    grid on;

    subplot(2,2,4);
    histfit(Errors, 50);
    title(['Error Mean = ' num2str(error_mean) ', Error St.D. = ' num2str(error_std)]);

end
```

Roulette Wheel Selection

```matlab
function i=RouletteWheelSelection(P)

    r=rand;

    c=cumsum(P);

    i=find(r<=c,1,'first');

end
```

Train ANFIS using PSO

```matlab
function bestfis=TrainAnfisUsingPSO(fis,data)

    %% Problem Definition

    p0=GetFISParams(fis);

    Problem.CostFunction=@(x) TrainFISCost(x,fis,data);

    Problem.nVar=numel(p0);

    Problem.VarMin=-40;
    Problem.VarMax=40;

    %% PSO Params
    Params.MaxIt=50;
    Params.nPop=30;

    %% Run PSO
    results=RunPSO(Problem,Params);

    %% Get Results

    p=results.BestSol.Position.*p0;
    bestfis=SetFISParams(fis,p);

end

function results=RunPSO(Problem,Params)

    disp('Starting PSO ...');
```

```matlab
%% Problem Definition

CostFunction=Problem.CostFunction;        % Cost Function

nVar=Problem.nVar;          % Number of Decision Variables

VarSize=[1 nVar];           % Size of Decision Variables Matrix

VarMin=Problem.VarMin;      % Lower Bound of Variables
VarMax=Problem.VarMax;       % Upper Bound of Variables

%% PSO Parameters

MaxIt=Params.MaxIt;      % Maximum Number of Iterations

nPop=Params.nPop;         % Population Size (Swarm Size)

w=1;            % Inertia Weight
wdamp=0.99;     % Inertia Weight Damping Ratio
c1=1;           % Personal Learning Coefficient
c2=2;           % Global Learning Coefficient

% Constriction Coefficients
% phi1=2.05;
% phi2=2.05;
% phi=phi1+phi2;
% chi=2/(phi-2+sqrt(phi^2-4*phi));
% w=chi;          % Inertia Weight
% wdamp=1;        % Inertia Weight Damping Ratio
% c1=chi*phi1;    % Personal Learning Coefficient
% c2=chi*phi2;    % Global Learning Coefficient

% Velocity Limits
VelMax=0.1*(VarMax-VarMin);
VelMin=-VelMax;

%% Initialization

empty_particle.Position=[];
empty_particle.Cost=[];
empty_particle.Velocity=[];
empty_particle.Best.Position=[];
empty_particle.Best.Cost=[];

particle=repmat(empty_particle,nPop,1);
```

```
BestSol.Cost=inf;

for i=1:nPop

    % Initialize Position
    if i>1
        particle(i).Position=unifrnd(VarMin,VarMax,VarSize);
    else
        particle(i).Position=ones(VarSize);
    end

    % Initialize Velocity
    particle(i).Velocity=zeros(VarSize);

    % Evaluation
    particle(i).Cost=CostFunction(particle(i).Position);

    % Update Personal Best
    particle(i).Best.Position=particle(i).Position;
    particle(i).Best.Cost=particle(i).Cost;

    % Update Global Best
    if particle(i).Best.Cost<BestSol.Cost

        BestSol=particle(i).Best;

    end

end

BestCost=zeros(MaxIt,1);

%% PSO Main Loop

for it=1:MaxIt

    for i=1:nPop

        % Update Velocity
        particle(i).Velocity = w*particle(i).Velocity ...
            +c1*rand(VarSize).*(particle(i).Best.Position-particle(i).Position) ...
            +c2*rand(VarSize).*(BestSol.Position-particle(i).Position);

        % Apply Velocity Limits
```

```matlab
        particle(i).Velocity = max(particle(i).Velocity,VelMin);
        particle(i).Velocity = min(particle(i).Velocity,VelMax);

        % Update Position
        particle(i).Position = particle(i).Position + particle(i).Velocity;

        % Velocity Mirror Effect
        IsOutside=(particle(i).Position<VarMin | particle(i).Position>VarMax);
        particle(i).Velocity(IsOutside)=-particle(i).Velocity(IsOutside);

        % Apply Position Limits
        particle(i).Position = max(particle(i).Position,VarMin);
        particle(i).Position = min(particle(i).Position,VarMax);

        % Evaluation
        particle(i).Cost = CostFunction(particle(i).Position);

        % Update Personal Best
        if particle(i).Cost<particle(i).Best.Cost

            particle(i).Best.Position=particle(i).Position;
            particle(i).Best.Cost=particle(i).Cost;

            % Update Global Best
            if particle(i).Best.Cost<BestSol.Cost

                BestSol=particle(i).Best;

            end

        end

    end

    BestCost(it)=BestSol.Cost;

    disp(['Iteration ' num2str(it) ': Best Cost = ' num2str(BestCost(it))]);

    w=w*wdamp;

end

disp('End of PSO.');
disp(' ');
```

%% Results

    results.BestSol=BestSol;
    results.BestCost=BestCost;

end

Train ANFIS using GA

function bestfis=TrainAnfisUsingGA(fis,data)

    %% Problem Definition

    p0=GetFISParams(fis);

    Problem.CostFunction=@(x) TrainFISCost(x,fis,data);

    Problem.nVar=numel(p0);

    Problem.VarMin=-20;
    Problem.VarMax=20;

    %% GA Params
    Params.MaxIt=50;
    Params.nPop=30;

    %% Run GA
    results=RunGA(Problem,Params);

    %% Get Results

    p=results.BestSol.Position.*p0;
    bestfis=SetFISParams(fis,p);

end

function results=RunGA(Problem,Params)

    disp('Starting GA ...');

    %% Problem Definition

    CostFunction=Problem.CostFunction;   % Cost Function

    nVar=Problem.nVar;   % Number of Decision Variables

```matlab
VarSize=[1 nVar];        % Size of Decision Variables Matrix

VarMin=Problem.VarMin;     % Lower Bound of Variables
VarMax=Problem.VarMax;     % Upper Bound of Variables

%% GA Parameters

MaxIt=Params.MaxIt;     % Maximum Number of Iterations

nPop=Params.nPop;       % Population Size

pc=0.4;               % Crossover Percentage
nc=2*round(pc*nPop/2);  % Number of Offsprings (Parnets)

pm=0.7;               % Mutation Percentage
nm=round(pm*nPop);      % Number of Mutants

gamma=0.7;

mu=0.15;       % Mutation Rate

beta=8;         % Selection Pressure

%% Initialization

empty_individual.Position=[];
empty_individual.Cost=[];

pop=repmat(empty_individual,nPop,1);

for i=1:nPop

    % Initialize Position
    if i>1
        pop(i).Position=unifrnd(VarMin,VarMax,VarSize);
    else
        pop(i).Position=ones(VarSize);
    end

    % Evaluation
    pop(i).Cost=CostFunction(pop(i).Position);

end

% Sort Population
```

```matlab
Costs=[pop.Cost];
[Costs, SortOrder]=sort(Costs);
pop=pop(SortOrder);

% Store Best Solution
BestSol=pop(1);

% Array to Hold Best Cost Values
BestCost=zeros(MaxIt,1);

% Store Cost
WorstCost=pop(end).Cost;


%% Main Loop

for it=1:MaxIt

    P=exp(-beta*Costs/WorstCost);
    P=P/sum(P);

    % Crossover
    popc=repmat(empty_individual,nc/2,2);
    for k=1:nc/2

        % Select Parents Indices
        i1=RouletteWheelSelection(P);
        i2=RouletteWheelSelection(P);

        % Select Parents
        p1=pop(i1);
        p2=pop(i2);

        % Apply Crossover
        [popc(k,1).Position, popc(k,2).Position]=...
            Crossover(p1.Position,p2.Position,gamma,VarMin,VarMax);

        % Evaluate Offsprings
        popc(k,1).Cost=CostFunction(popc(k,1).Position);
        popc(k,2).Cost=CostFunction(popc(k,2).Position);

    end
    popc=popc(:);
```
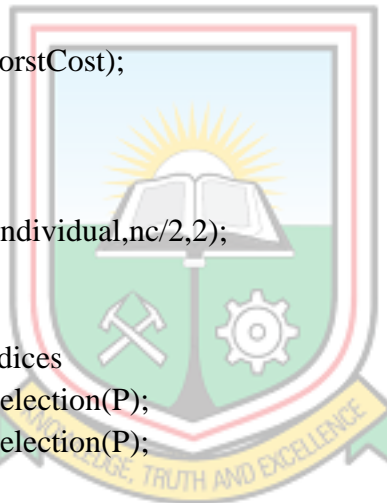
```matlab
    % Mutation
    popm=repmat(empty_individual,nm,1);
    for k=1:nm

        % Select Parent
        i=randi([1 nPop]);
        p=pop(i);

        % Apply Mutation
        popm(k).Position=Mutate(p.Position,mu,VarMin,VarMax);

        % Evaluate Mutant
        popm(k).Cost=CostFunction(popm(k).Position);

    end

    % Create Merged Population
    pop=[pop
        popc
        popm]; %#ok

    % Sort Population
    Costs=[pop.Cost];
    [Costs, SortOrder]=sort(Costs);
    pop=pop(SortOrder);

    % Update Worst Cost
    WorstCost=max(WorstCost,pop(end).Cost);

    % Truncation
    pop=pop(1:nPop);
    Costs=Costs(1:nPop);

    % Store Best Solution Ever Found
    BestSol=pop(1);

    % Store Best Cost Ever Found
    BestCost(it)=BestSol.Cost;

    % Show Iteration Information
    disp(['Iteration ' num2str(it) ': Best Cost = ' num2str(BestCost(it))]);

end

disp('End of GA.');
```

```matlab
    disp(' ');

    %% Results

    results.BestSol=BestSol;
    results.BestCost=BestCost;

end

function [y1, y2]=Crossover(x1,x2,gamma,VarMin,VarMax)

    alpha=unifrnd(-gamma,1+gamma,size(x1));

    y1=alpha.*x1+(1-alpha).*x2;
    y2=alpha.*x2+(1-alpha).*x1;

    y1=max(y1,VarMin);
    y1=min(y1,VarMax);

    y2=max(y2,VarMin);
    y2=min(y2,VarMax);

end

function y=Mutate(x,mu,VarMin,VarMax)

    nVar=numel(x);

    nmu=ceil(mu*nVar);

    j=randsample(nVar,nmu)';

    sigma=0.1*(VarMax-VarMin);

    y=x;
    y(j)=x(j)+sigma*randn(size(j));

    y=max(y,VarMin);
    y=min(y,VarMax);

end
```

Train ANFIS using FPA

```matlab
function bestfis=TrainAnfisUsingFPA(fis,data)
```

```matlab
%% Problem Definition

p0=GetFISParams(fis);

Problem.CostFunction=@(x) TrainFISCost(x,fis,data);

Problem.nVar=numel(p0);

Problem.VarMin=-40;
Problem.VarMax=40;

%% FPA Params
Params.MaxIt=100;
Params.nPop=20;

%% Run FPA
results=RunFPA(Problem,Params);

%% Get Results

p=results.BestSol.*p0;
bestfis=SetFISParams(fis,p);

end

function results=RunFPA(Problem,Params)

    disp('Starting FPA ...');
    %% Problem Definition

    Fun=Problem.CostFunction;

    nVar=Problem.nVar;          % Number of Decision Variables

    %VarSize=[1 nVar];          % Size of Decision Variables Matrix

    VarMin=Problem.VarMin;      % Lower Bound of Variables
    VarMax=Problem.VarMax;      % Upper Bound of Variables

    %% FPA Parameters
    N_iter=Params.MaxIt;        % Maximum Number of Iterations
    n=Params.nPop;              % Population Size (Swarm Size)
    q=0.8;                      % probability switch

    % Dimension of the search variables
```
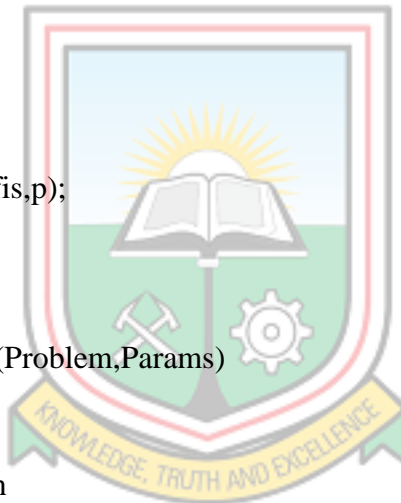
```
d=nVar;    %3;
Lb= VarMin*ones(1,d);       %-50*ones(1,d);
Ub= VarMax*ones(1,d);     %50*ones(1,d);


% % Initialize the population/solutions
% for i=1:n
%    Sol(i,:)=Lb+(Ub-Lb).*rand(1,d);
%    Fitness(i)=Fun(Sol(i,:));
% end


% Initialize the population/solutions
for i=1:n
   Sol(i,:)=Lb+(Ub-Lb).*rand(1,d);
   Fitness(i)=Fun(Sol(i,:));
end


% Find the current best
[fmin,I]=min(Fitness);
best=Sol(I,:);
S=Sol;


% Start the iterations -- Flower Algorithm
for t=1:N_iter
   % Loop over all bats/solutions
   for i=1:n
   % Pollens are carried by insects and thus can move in
   % large scale, large distance.
   % This L should replace by Levy flights
   % Formula: x_i^{t+1}=x_i^t+ L (x_i^t-gbest)
   if rand>q
   %% L=rand;
   L=Levy(d);
   dS=L.*(Sol(i,:)-best);
   S(i,:)=Sol(i,:)+dS;


   % Check if the simple limits/bounds are OK
   S(i,:)=simplebounds(S(i,:),Lb,Ub);


   % If not, then local pollenation of neighbor flowers
   else
      epsilon=rand;
      % Find random flowers in the neighbourhood
      JK=randperm(n);
      % As they are random, the first two entries also random
      % If the flower are the same or similar species, then
```
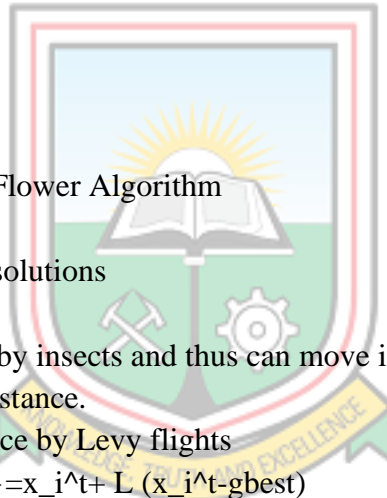
```matlab
        % they can be pollenated, otherwise, no action.
        % Formula: x_i^{t+1}+epsilon*(x_j^t-x_k^t)
        S(i,:)=S(i,:)+epsilon*(Sol(JK(1),:)-Sol(JK(2),:));
        % Check if the simple limits/bounds are OK
        S(i,:)=simplebounds(S(i,:),Lb,Ub);
    end

    % Evaluate new solutions
    Fnew=Fun(S(i,:));
    % If fitness improves (better solutions found), update then
    if (Fnew<=Fitness(i))
        Sol(i,:)=S(i,:);
        Fitness(i)=Fnew;
    end

    % Update the current global best
    if Fnew<=fmin
        best=S(i,:)   ;
        fmin=Fnew   ;
    end
    end
    % Display results every 100 iterations
    if round(t/100)==t/5
       best
       fmin
    end

end

% Output/display
disp(['Total number of evaluations: ',num2str(N_iter*n)]);
disp(['Best solution=',num2str(best),'   fmin=',num2str(fmin)]);

disp('End of FPA.');
disp(' ');

% Application of simple constraints
function s=simplebounds(s,Lb,Ub)
  % Apply the lower bound
  ns_tmp=s;
  I=ns_tmp<Lb;
  ns_tmp(I)=Lb(I);

  % Apply the upper bounds
  J=ns_tmp>Ub;
```

```matlab
    ns_tmp(J)=Ub(J);
    % Update this new move
    s=ns_tmp;
  end


% Draw n Levy flight sample
function L=Levy(d)
  % Levy exponent and coefficient
  % For details, see Chapter 11 of the following book:
  % Xin-She Yang, Nature-Inspired Optimization Algorithms, Elsevier, (2014).
  beta=3/2;
  sigma=(gamma(1+beta)*sin(pi*beta/2)/(gamma((1+beta)/2)*beta*2^((beta-
    1)/2)))^(1/beta);
  u=randn(1,d)*sigma;
  v=randn(1,d);
  step=u./abs(v).^(1/beta);
  L=0.01*step;
end

%% Results

results.BestSol=best;
results.BestCost=fmin;

end
```